

Cover Page



Universiteit Leiden



The handle <http://hdl.handle.net/1887/85674> holds various files of this Leiden University dissertation.

Author: Jiang, L.

Title: Chemical functionalization of the graphene surface for electrical and electrochemical sensing applications

Issue Date: 2020-02-27

Chemical functionalization of the graphene surface for electrical and electrochemical sensing applications

Proefschrift

ter verkrijging van
de graad van Doctor aan de Universiteit Leiden,
op gezag van Rector Magnificus prof.mr. C.J.J.M. Stolker,
volgens besluit van het College voor Promoties
te verdedigen op Donderdag 27 Februari 2020
klokke 13.45 uur

door

Lin Jiang

geboren op 16 September 1988 te Shandong, P.R.China

Promotiecommissie

Promotors: Dr. G. F. Schneider

Prof. Dr. A. Kros

Overige Leden:

Prof. dr. H. S. Overkleeft, LIC (voorzitter)

Prof. dr. J. Brouwer, LIC (secretaris)

Dr. E. M. Blokhuis, LIC

Prof. dr. B. Holst, University of Bergen, Norway

Prof. dr. R. Dryfe, The University of Manchester, UK

Prof. dr. M. Strano, Massachusetts Institute of Technology, USA

For my parents

For Feng Jiang

Table of Contents

Chapter 1	1
Introduction	
Chapter 2	33
Quantum and electrochemical interplay in hydrogenated graphene	
Chapter 3	51
Oxygen reduction reaction on nitrogen-doped graphene activated by co-doped oxygen functional groups	
Chapter 4	67
Hydrogenation cleans up airborne contamination from graphene	
Chapter 5	79
Graphene mechanics studied by biaxial compression: The effect of sp^3 and vacancy defects	
Chapter 6	91
Hydrogenated and nitrogenated graphene for field effect gas sensing	
Chapter 7	103
Summary, Conclusions and Outlook	
Appendix I	109
Supporting Information for Chapter 2	
Appendix II	123
Supporting Information for Chapter 3	
Appendix III	135
Supporting Information for Chapter 4	
Appendix IV	143
Supporting Information for Chapter 5	
Appendix V	155
Supporting Information for Chapter 6	
Samenvatting	159
Curriculum Vitae	163
List of Publications	165
Acknowledgements	167

Chapter 1

Introduction

Part of this chapter was published as a review article: Wangyang Fu, Lin Jiang, Erik P. van Geest, Lia M. C. Lima, and Grégory F. Schneider, *Adv. Mater.* **2017**, 29, 1603610.

Graphene is a two-dimensional (2D) carbon allotrope composed of a single layer of sp^2 hybridized atoms arranged in a hexagonal lattice. Figure 1.1a shows the honeycomb lattice of graphene containing atom A and atom B in each unit cell. As the sp^2 orbitals contribute to form the plane, the unsaturated perpendicular p_z orbitals form an extended π -band with delocalized electrons. The conduction π^* band and valence π band meet each other at the so-called Dirac point (K and K') or charge neutrality point, forming a zero bandgap semiconductor (Figure 1.1b). At the low energies that are most relevant in electron transport, the electrons behave in a linear dispersion with the band structure viewed as two conical cones (Dirac cones, Figure 1.1c). As illustrated in Figure 1d, the density of states (DOS) varies linearly with the energy in each Dirac cone. More importantly, such a unique band structure contributes to the intrinsic charge carrier mobility of graphene at room temperature, which can be as high as $15000 \text{ cm}^2 \text{ V}^{-1} \text{ s}^{-1}$.^[1]

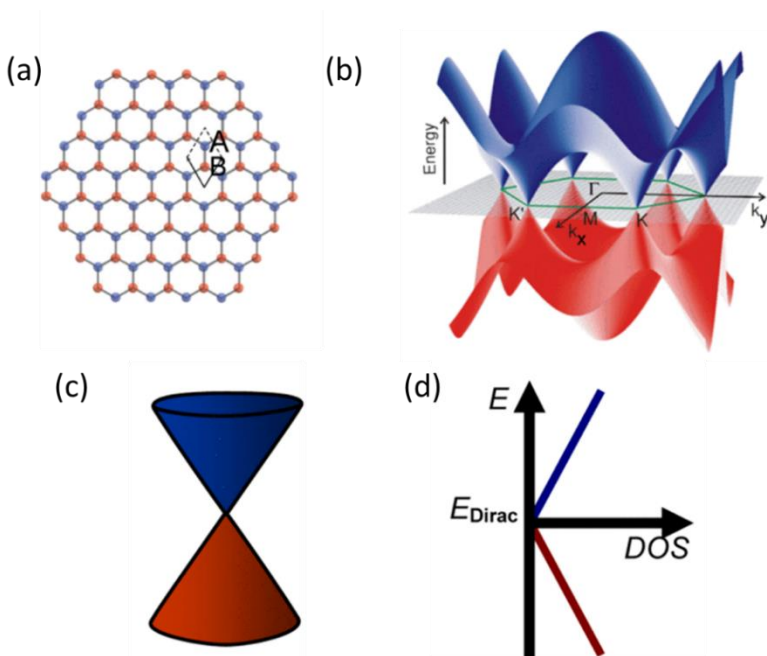


Figure 1.1 Graphene lattice and band structure. a) The honeycomb lattice. b) The electronic band structure. b) Linear dispersion at low energies. c) Density of states (DOS) dependence on energy.^[2]

In addition to the extraordinarily high mobility, graphene is also characterized with a low intrinsic electrical noise^[3] and inert chemical properties. All these properties render the graphene basal plane an ideal candidate for electrical and electrochemical studies. In particular, nanoelectronics based on the surface of graphene provide a

versatile platform for a wide spectrum of (bio)chemical sensing applications.^[4] Detection can be realized through various mechanisms, including charge transfer,^[5] charge scattering,^[6] capacitive effect,^[7] and field effect^[8]. In particular, the electrical field effect has been widely regarded as one of the most reliable sensing mechanisms.

1.1 Graphene field-effect transistors (GFETs)

Since the experimental preparation and observation of the electric field effect in graphene by the Manchester group in 2004,^[9] biochemical sensing using graphene electronic devices has been actively pursued.^[10] The sensing principle rests on a change of the electrical conductance of the graphene channel upon adsorption of a molecule on the sensor surface.^[10a] The uniqueness of graphene among other solid-state materials is that all carbon atoms are located on the surface, making the graphene surface potentially highly sensitive to any changes of its surrounding environment. For instance, the chemisorption of gas molecules on the graphene surface has been reported with the sensitivity down to a single molecule detection,^[10a] which is mainly ascribed to the surface contaminations by polymer residues during device fabrication.^[11]

1.1.1 Back-gated GFETs

The word transistor is a combination of two words: transfer and resistor. Usually a transistor is used to switch or amplify an electronic signal, comparable to a tap-valve that controls the supply and flow of water. Figure 1.2a depicts a back-gated GFET composed of a source/drain metallic electrode bridged together with a graphene channel. The carrier density, and thus the conductivity of the channel is typically modulated by the electric field via gating a highly conductive silicon substrate located underneath an insulating SiO₂ dielectric layer to a range of voltages. As shown in Figure 1.2b, a typical measurement consists in applying a constant bias voltage, V_{sd} , between the source and the drain of the graphene channel, and monitoring the resulting source-drain current I_{sd} . By changing the back gate voltage V_g , the electrochemical potential of the charge carriers (i.e., the Fermi energy) can be modulated. As a consequence, the type of charge carriers (which flow in the graphene channel and give the current I_{sd}) can continuously be tuned from holes (red curve in the left of Figure 1.2b) to electrons (grey curve in the right of Figure 1.2b), yielding a so-called 'ambipolar behavior'. At the transition between the electron and hole regime, the current (conductivity) is minimized and this point is also known as the charge neutrality point (CNP).

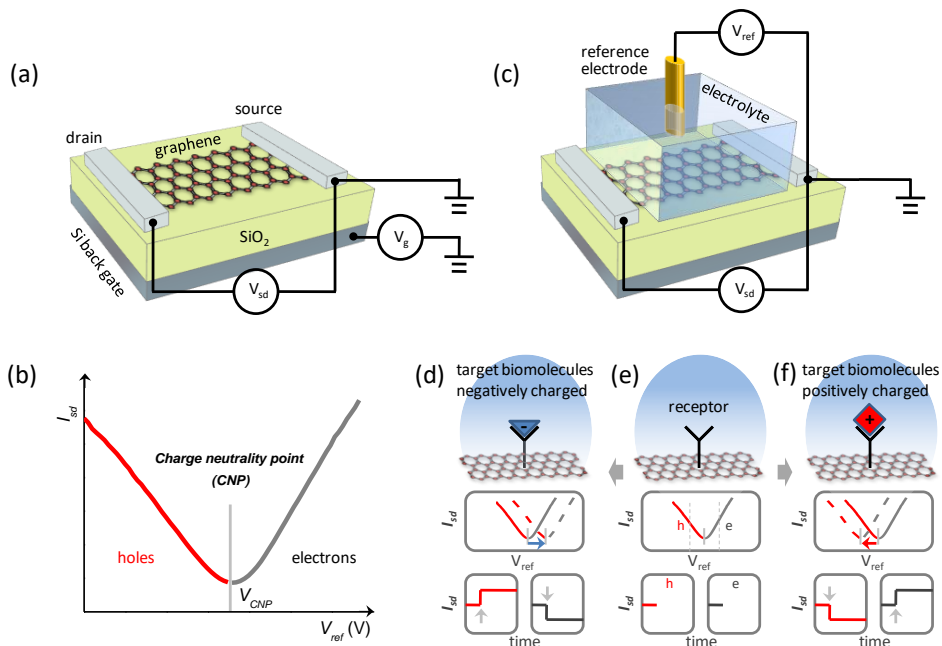


Figure 1.2 Working principle of a graphene field-effect transistor (GFET). a) Schematic of a back-gated GFET. b) Typical ambipolar transfer characteristics showing that the type of carriers in graphene can continuously be modulated from holes (on the left, in red) to electrons (on the right, in grey) using the field effect. The charge-neutrality point (CNP) is located at the transition between the electron and hole regime, where the current is minimized. c) Schematic of an electrochemically-gated GFET device and its sensing principle (d-f). In the upper panel of e), a receptor molecule is immobilized on the graphene surface. The plots of I_{sd} versus V_{ref} and I_{sd} versus the time t are shown in the middle and lower panels, respectively. The abbreviation 'h' in red refers a measurement carried in the hole regime (and 'e' for the electron regime in grey). f) (respectively d) depicts the field effect resulting from the binding of a positively (respectively negatively) charged target on the receptor (as indicated by the grey arrows in the $I_{sd}(t)$ curves). The binding of a charged target as indicated by the blue arrows yields a shift in the curves of I_{sd} versus V_{ref} .

1.1.2 Electrochemically-gated GFETs

A change in the electric field can either be achieved using the above discussed back-gate voltage or be induced by physisorption or chemisorption of the target molecules. When the back-gate is held at a fixed voltage the change in current between the drain and source must thus be due to molecules adsorbed on the graphene surface, as demonstrated in a pioneering study by the Manchester group in 2007 with single molecule detection capability upon NO_2 chemisorption.^[10a]

In contrast to the back-gate geometry, in an electrochemically-gated configuration the

gate voltage is applied to the electrolyte via a reference electrode (Figure 1.2c). The reference electrode is coupled to the graphene channel through an interfacial capacitance C , consisting of a series of two capacitances,^[12] namely the quantum capacitance of graphene (C_Q),^[13] and the double layer capacitance of the electrolyte (C_{DL}).^[14] The double layer capacitor is a virtual capacitor formed by the separated charges located at the solid side and the solution side of the interface as described by the Poisson-Boltzmann equation.^[15] Electrochemically-gated GFETs belong to the large family of ion-sensitive FETs, the first new concept of which was investigated by Bergveld with Si devices.^[16] Although the choice of the channel materials, the reference electrode, the operational mode, and the final encapsulation for liquid handling, vary from case to case, the heart of any ion-sensitive FETs lies on the interface between electrolyte and the solid FET materials. In general, GFETs are operated at low electrolyte gate voltage such that any electrochemical processes and exchange ionic currents are negligible, i.e., the interface is considered to be inert and purely capacitive, although this assumption is not always explicitly stated in most of the literature. Experimental artifacts at moderate or relatively high electrolyte gate voltages resulting from such simple assumption are considered mainly of electrochemical nature.

The working principle of an electrochemically-gated GFET sensor is illustrated in Figure 1.2d-f. In practice, electrochemically-gated GFETs can be integrated into microfluidic systems:^[17] the confinement into the fluidic channel helps in bringing the analyte to the sensor surface.^[18] In a typical measurement, receptor molecules are immobilized on the surface for selective recognition of target molecules (Figure 1.2e, upper panel). The corresponding I_{sd} versus V_{ref} curve of such an electrochemically-gated GFET is shown in the middle panel (Figure 1.2e) with similar characteristics as the one observed for a back-gated GFET (Figure 1.2b). The lower panel of Figure 1.2e depicts the time dependent current I_{sd} at a fixed reference potential V_{ref} (as indicated by the dashed grey lines). In either the hole regime (as indicated by 'h') or in the electron regime ('e'), when a positively charged target binds (Figure 1.2f, upper panel), a depletion of hole carriers (respectively an accumulation of electron carriers) in the graphene occurs due to the field effect. Such doping effect causes a negative shift of the $I_{sd}(V_{ref})$ curve as indicated by the blue arrow in Figure 1.2f (middle panel). In the time-dependent measurement (i.e., the lower panel of Figure 1.2f), the binding of a positively charged target causes a decrease of the current I_{sd} in the hole regime, and an increase of the current in the electron regime. Conversely, the binding of a negatively charged target (Figure 1.2e) induces a positive shift of the $I_{sd}(V_{ref})$ curve and an increase in the I_{sd} in the hole regime. In the electron regime – instead – the same event induces a negative shift of the $I_{sd}(V_{ref})$ curve and a decrease of the current

I_{sd} . This current modulation in the graphene channel can be expressed as a function of the change in the carrier density Δn , which is induced by and is proportional to the total number N of charged molecules adsorbing on the graphene surface:^[19]

$$\Delta I_{sd} = \frac{w}{l} V_{sd} e \mu \Delta n \propto N \quad (1)$$

where w and l are the width and length of the graphene channel, e is the electron charge, and μ is the charge carrier mobility. In Equation (1), it is clear that the sensing response of a transistor sensor should be proportional to the total number of adsorbed molecules N . The quantitative monitoring of molecules, however, is non-trivial. Challenges lie in characterizing the number of charges each molecule carry, in controlling the chemical functionalization, and in identifying the exact sensing reactions at the graphene surface in each different regime. It is of note here that, in principle, non-charged molecules should have no influences on the field-effect sensing response of GFET sensors, unless they can induce a charge variation (for example, through subtle dipole fluctuation^[20] or molecular engineering^[21]). To deduce Equation (1), it is assumed that graphene has a constant carrier mobility μ upon the adsorption of charged molecules. This assumption is correct in most cases where the adsorbed molecules bind to the receptors and interact weakly with the graphene lattice. However, molecules that directly bind on a graphene surface form additional scattering centers, resulting in a change of the mobility of charge carriers.^[22] Additionally, practical sensor designs also take into account the changes in interfacial capacitance upon molecules adsorption.^[23]

1.1.3 Sensing with GFETs of high carrier mobility

The change of the electrical current ΔI_{sd} resulting from the minute field-effect induced – for example – by the interaction of a biochemical molecule carrying an electron charge, defines the sensing response $S = \Delta I_{sd}/N$. According to Equation (1), S is therefore proportional to the mobility μ of graphene. With other parameters equal (especially the electrical noise performance), a higher sensing response S implies a better sensor performance.

Because the performance of GFET sensors depends on the mobility μ , the use and integration of high quality graphene into devices is fundamental. To achieve high-quality pristine monolayer or few layer graphene sheets, the most commonly used method is the micromechanical cleavage of graphite with adhesive tape.^[9] This so-called ‘scotch tape’ technique involves splitting few layers of graphene from multi-layered graphite, after which the flakes are pressed and ‘dry-deposited’ onto a silicon wafer. Compared to graphene synthesized using other methods, micromechanical

cleavage yields graphene with higher mobility and lower intrinsic electrical noise, primarily because fewer structural defects are introduced upon preparation.^[24] Generally, for exfoliated graphene on SiO₂/Si wafers, mobilities on the order of $\sim 3,000\text{-}15,000\text{ cm}^2\text{ V}^{-1}\text{ s}^{-1}$ are reported,^[25] which is more than one order of magnitude higher than those of silicon materials ($\sim 100\text{-}1,500\text{ cm}^2\text{ V}^{-1}\text{ s}^{-1}$).^[26] The mobilities of the first graphene-based gas sensor devices were $\sim 5,000\text{ cm}^2\text{ V}^{-1}\text{ s}^{-1}$.^[27] Nowadays, at room temperature, carrier mobility up to $100,000\text{-}197,600\text{ cm}^2\text{ V}^{-1}\text{ s}^{-1}$, can be achieved by encapsulating graphene in boron nitride (BN),^[28] providing unprecedented possibilities for sensing applications. The fact that this idea has only been realized very recently (with h-BN capped MoS₂^[29]) is not a surprise: groups that work on high quality BN coated graphene samples, very often focus on cryogenic measurements of the physics of the 2D electron gases in graphene rather than its biological sensing applications; moreover, the fabrication methods are very delicate (it is not yet trivial to achieve an ideal interface) and the lack of scalability is still an important drawback.^[28a]

Despite all the impressive achievements in the electrical performances of graphene devices, the reproducibility and homogeneity of sample preparation and the relatively small size (on micrometer scale) represent the bottleneck for using exfoliated graphene for practical applications. Larger sheets of few-layer or monolayer graphene can now be directly synthesized via chemical vapor deposition (CVD) on nickel or copper substrates^[30] with mobilities rivalling the ones of exfoliated samples.^[31] For samples placed on SiO₂/Si wafers, mobilities on the order of $\sim 1,000\text{-}10,000\text{ cm}^2\text{ V}^{-1}\text{ s}^{-1}$ are now routinely observed and regarded as the standard for graphene transistor products for sensing applications.^[32] The electronic performances of CVD graphene^[33] can be significantly enhanced by growing single-crystal graphene free of grain boundaries^[34] and by using a BN substrate similarly to exfoliated graphene, with which mobility up to $\sim 50,000\text{-}350,000\text{ cm}^2\text{ V}^{-1}\text{ s}^{-1}$ can be achieved.^[35] These mobility numbers are rivaling those of exfoliated samples, making the CVD process ideal for large-area synthesis of high-quality and uniform graphene for sensing applications.

1.1.4 Electrical noise performances of GFETs

At low frequencies (100 Hz), the ubiquitous $1/f$ noise, whose power spectral density (PSD) spectrum inversely depends on the frequency f ,^[36] seriously impedes the sensing performances of GFETs.^[3a] This low-frequency $1/f$ noise is even more pronounced for devices that are scaled down to nanometer dimensions, where the channel current becomes more prone to fluctuations due to, particularly, interface and surface trap states.^[37] It is the level of these unwanted fluctuations (along with

the sensing response S) that determines the ultimate detection limit of GFET sensors. The $1/f$ noise of graphene mono-layers supported on a substrate is comparable to that of bulk semiconductors (including Si).^[38] For freestanding or bilayer graphene, however, the $1/f$ noise was found to be one order of magnitude lower through the effective screening of potential fluctuations from external charged impurities (for example, oxide traps or interface states).^[3b, 38] The fact that graphene

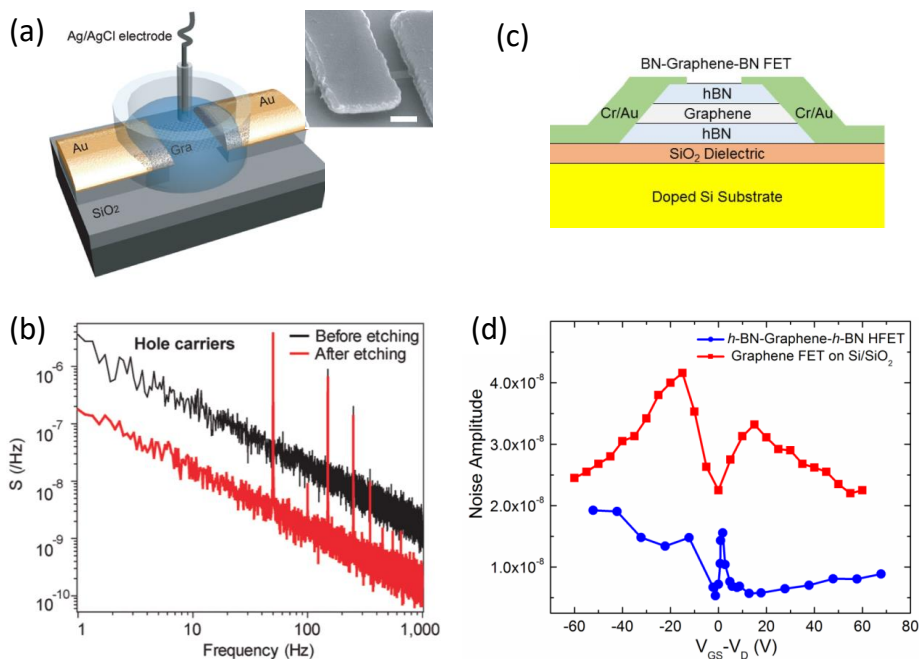


Figure 1.3 Noise performance of graphene. a) Schematic representation of the experimental setup where a single-layer graphene is supported in solution by Cr/Au contacts to bridge a trench in the oxide. The inset shows an SEM image of a suspended graphene device. Scale bar is 0.5 μm . b) Comparison of graphene's noise power spectra in the linear operating modes with holes as carriers before (black) and after suspension of the graphene layer (red). The red/black spikes are due to 50 Hz noise coupled from the power lines.^[3b] c) Schematics of BN-graphene-BN FET. d) Noise amplitude as a function of the gate voltage for both BN-graphene-BN FET (in blue) and conventional non-encapsulated GFET on Si/SiO₂ wafer (in red).^[39]

possesses both superior mobility and noise performances, gives it a better signal-to-noise ratio (SNR) as advocated from time to time by literature, reporting graphene based sensors with superior performances compared to their Si based counterpart devices.^[40] Figure 1.3b compares the noise performances of a GFET device supported by a SiO₂/Si substrate and its counterpart after suspending the graphene monolayer by etching the underlying SiO₂ substrate (Figure 1.3a).^[3b] The large noise suppression

was mainly attributed to the removal of any external trap states in the supported SiO₂ substrate since the $1/f$ noise in graphene devices is a surface phenomenon.^[41]

Similarly, defects in the graphene are another source of noise. For example, the permanent oxygen-based defects contained in graphene oxide (GO) or reduced graphene oxide (rGO) – introduced by over-oxidation (for GO) or incomplete removal of oxygen groups (for rGO) – lead to inferior electrical quality (i.e., degradation in the mobility and noise performance) compared to scotch-tape or CVD graphene.^[42] Interestingly, environmental exposure and ageing of graphene devices also increase the level of noise, suggesting that a proper capping layer or surface functionalization may circumvent an increase of noise.^[43] Indeed, by encapsulating a single layer graphene between two layers of hexagonal boron nitride (h-BN, as shown in Figure 1.3c), the noise spectral density normalized to the channel area (blue dots, Figure 1.3d) can be suppressed up to one order of magnitude lower compared to non-encapsulated devices on Si/SiO₂ (red dots, Figure 1.3d).^[39] In the case of silicon FET, the functionalization of the sensor channel (in this case a silicon nanowire buried in a SiO₂ dielectric) with 3-aminopropyl-triethoxysilane (APTES) yields better noise performances (up to 60 times), presumably due to the passivation of the oxide traps and interface states at the sensor surface.^[44] On the contrary, for carbon nanotubes, a two-level random telegraphic noise (RTN) was reported and ascribed to a single probe molecule (more precisely, the binding and unbinding of charged target molecules at its active sites), which was covalently bound to a defect in the carbon nanotube sidewall.^[45] A suppression of the RTN was observed in high ionic strength buffer solutions (ionic screening) and for high gate potentials (when the target molecules are repelled from the nanotube). The influence of surface functionalization on the noise performances of liquid-gated GFETs has not yet been systematically studied. As previously discussed, with other parameters equal (especially the electrical noise performance), a higher mobility implies a better sensor performance when considering the adsorption of charged molecules. It is of note here that a higher mobility also complies with graphene bearing less defects and impurities, which is in favor of an improved noise performance (although there is still not enough experimental evidences or theories that could directly and unambiguously link the high mobility of GFETs to their noise performances).

1.2 Graphene for electrochemical sensing

In electrochemically-gated GFETs, the electrical current is confined transversely in the graphene conductive channel. Any electrochemical current vertically flowing between the graphene channel and the liquid gate (through the electrolyte solution), is regarded as a spurious signal and limits the performances of gate controlled GFET

devices.^[46] This electrochemical current is – however – at the basis of graphene electrochemical (GEC) sensing, which are complementary to FETs.^[47] In this regard, it is necessary to understand the construction as well as the working principle of a GEC sensor, in order to fully appreciate the operation of a GFET. Specifically, the sensing principle of a GEC sensor rests on the electrochemical transfer current between the redox active molecules in the solution-phase and graphene surface.

As a single-layered sp^2 -hybridized carbon material, graphene has the similar atomic surface structure with highly ordered pyrolytic graphite (HOPG), a classical electrode material for electrochemistry related fundamental studies and applications. However, one of the disadvantages for HOPG is its low reproducibility of the electrode surface due to the abundant edge planes. In contrast, high-quality and homogenous graphene presents a more reproducible surface morphology and chemistry. Moreover, the extraordinarily high mobility and other assets like large specific surface area ($2630 \text{ m}^2 \text{ g}^{-1}$)^[48] and large potential window in aqueous media concordantly prepare graphene for electroanalytical and electrocatalytic applications with high sensitivity and stability.

1.2.1 The electrochemical activity of graphene

In electrochemistry, the electron is transferred between the redox molecules and the electrode, whose Fermi level can be tuned through the applied potential. The electron transfer process occurs when the electrochemical potential of the electrode (the Fermi level) is properly aligned with the HOMO/LUMO level of the redox molecules. For instance, the reduction reaction occurs when the electrons flow from the graphene surface to the LUMO orbital of the oxidative molecules. Given a specific redox system, the kinetics of electron transfer (reflected by the heterogeneous electron transfer rate k^0) is expected to be closely related to the DOS of graphene. As an important electrode parameter, the DOS at certain energy level defines how many states are available to be occupied by the electrons. Normally a higher DOS, which is determined by the electronic structure of an electrode, improves the possibility of electron transfer between the electrode and the redox systems near its surface.^[49] A low DOS at the Fermi level (also illustrated in Figure 1.1c) is general for an infinite pristine graphene sheet.^[50]

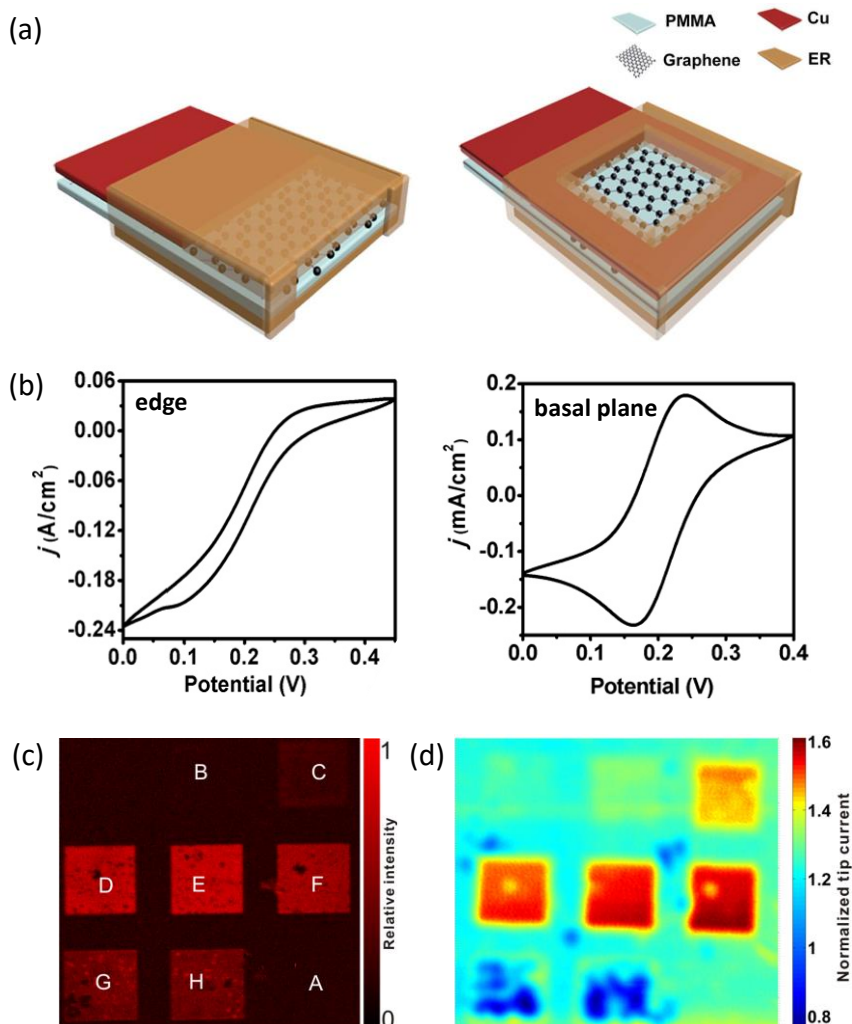


Figure 1.4 The electrochemical activity of graphene. **a)** An illustration of edge-based (left) and basal plane-based (right) CVD graphene. Epoxy resin (ER), a non-conducting pinhole-free polymer, is employed here to coat graphene and only expose the surface of interest. **b)** Cyclic voltammetry studies demonstrated that the current density on edge electrode (0.11 A cm^{-2}) is 500 times higher than that on the basal plane one ($2.2 \times 10^{-4} \text{ A cm}^{-2}$).^[51] **c)** Raman mapping of the D band of the defective graphene patterns (light squares) induced by Ar^+ irradiation. Window size: $500 \mu\text{m}$ by $500 \mu\text{m}$. **d)** Scanning electrochemical microscopy (SECM) of the same defective graphene patterns with a tip potential of 0.4 V and a substrate potential of 0.11 V . Window size: $500 \mu\text{m}$ by $500 \mu\text{m}$. Square F with medium defect density as tested by Raman spectroscopy exhibits the highest electrochemical activity.^[52]

Similarly to GFETs, the GEC uses the surface of graphene as the major sensing element. Until now, the majority of GECs uses graphene dispersions (usually nanosheets of chemically functionalized graphene) deposited on conductive

electrodes.^[53] These graphene dispersions with large surface to volume ratio – in contrast with mono- or bilayer graphene sheets employed in GFETs – contain more defective areas. These defects enhance the density of electronic states (DOS) of graphene dispersions, which favors the electron transfer between the graphene materials and the redox molecules, and thus yielding a higher sensitivity.^[50] For example, reduced graphene nanowalls (rGNW) with large amount of sharp edges have been deposited vertically via electrophoresis on a graphite electrode to detect double-stranded DNA (dsDNA) with an impressively wide detection concentration range of 0.1 fM – 10 mM.^[53b]

The sensitivity of the abovementioned GEC sensors resides in the defects of graphene. Functionalization of these defects with electrochemical catalysts lead to further improved sensitivity and selectivity for the detection of a wide range of molecules, namely glucose,^[54] cholesterol,^[55] DNA,^[56] proteins,^[57] and even living cells.^[58] To functionalize graphene, most typical catalysts are composed of enzymes,^[59] metal nanoparticles,^[60] and polymers,^[61] to name a few. Advantageously, covalent functionalization often results in dramatically enhanced DOS in graphene facilitating higher electron transfer rate.^[50] Non-covalent functionalization, however, has the advantage to retain the excellent electrical properties of graphene, and, to a certain extent, limit the possible charge transfer across the interface, and thus favoring the GFET sensors. Drop-casting deposition^[56d] is one of the most widely adopted methodologies to fabricate GEC sensors with functionalized graphene dispersions. Such graphene dispersions, however, usually contain a mixture of mono-, bi-, few layer graphene flakes with uncontrolled and even unknown defect, impurities, or chemical functionalities. In order to unambiguously address the electrochemical properties of graphene, the difference in the electrochemical activity of the edge and the basal plane of graphene have been carefully studied (Figure 1.4a).^[51] Graphene edges (with current density $j = 0.11 \text{ A cm}^{-2}$) exhibit a faster electron transfer than the basal plane ($j = 2.2 \times 10^{-4} \text{ A cm}^{-2}$), though convergent diffusion induced a faster mass transport can contribute to a higher current density for edges (Figure 1.4b). Previous studies carried out on clean graphene monolayer with a well-defined surface area,^[62] on free-standing graphene samples over a nanopore,^[63] and on graphene and graphite step edges using scanning electrochemical microscopy (SECM),^[52, 64] confirmed this trend that edges are electrochemically more active than the basal plane.^[65] In combination with Raman spectroscopy (Figure 1.4c), SECM is able to quantitatively correlate the defect density of graphene with its localized electrochemical activity (Figure 1.4d),^[52] providing new possibilities to systematically study the electrochemical properties of graphene. The correlation indicates that the electrochemical activity first increases with the defect density (in line with earlier

reported higher reactivity for covalent derivatization^[66]), and then decreases when 'defective' graphene sheet loses its structure integrity (i.e., presumably when the aromaticity of graphene is totally lost). As a perspective, a GFET sensor can in principle be combined with a GEC sensor as described here in a same device, and thus providing a fully complementary sensing platform to study both the electrostatic charge of the molecules but also the electron transfer during redox reaction at the graphene surface. Such device configuration has already been realized in organic electrochemical transistors with graphene-modified gate electrodes, which was proved to significantly improve the selectivity of the organic electrochemical transistors for dopamine detection.^[67]

1.2.2 Graphene-based electrocatalysis

Chemical functionalization and defects in graphene endow it with high electrocatalytic activity to various (bio)chemical reactions. Specifically, graphene upon nitrogen (N) doping, referred to as nitrogenated graphene or N-doped graphene, has been considered as alternative catalysts to the traditional noble metal based catalysts for oxygen reduction reaction (ORR).^[68] As the cathode reaction in fuel cells, electrochemical ORR is known for its notoriously sluggish kinetics. Therefore, considerable attention have been drawn for the development of cathode catalysts with high activity and/or selectivity to gain more energy.^[69] ORR involves multiple steps of reaction and electron transfer, in which the pathway is determined by the catalyst itself and electrolyte solution.^[70] In aqueous media, ORR mainly produces water via a four-electron pathway or hydrogen peroxide through a two-step two-electron process. Highly selective ORR with exclusive $2e^-$ or $4e^-$ product is equally desired for practical applications. To obtain a higher catalytic efficiency, tremendous efforts have been devoted to experimentally and theoretically determine the active sites in N-doped carbon materials for ORR catalysis.^[71] In particular, positive charge in the carbon atoms adjacent to the doped nitrogen atoms have been suggested to preferentially adsorb O_2 molecules. Nevertheless, controversies still remain. For example, there is still a debate on whether pyridinic N (N atom bonded to two carbon atoms) or graphitic N (N atom bonded to three carbon atoms) generates the active sites.^[72] On other respect, doubts also arise concerning that N-dopant are not active, or are less active than other doping sites like vacancy defects.^[71c, 73] Recently, vacancy defects is proposed to exhibit a higher ORR activity than the pyridinic sites in nitrogenated graphite.^[74] In summary, all the above-mentioned contradictions mainly originate from the significantly varied structure and surface chemistry of the studied carbon-based materials. For N-doped graphene, the nanoflakes dispersions can be very inhomogeneous in terms of size and crystallinity, caused by unpredictable chemical or physical reactions. Therefore a more reliable and well-defined N-doped

graphene catalyst is desired to disclose the structure–activity correlations for ORR.

1.3 Chemical functionalization of graphene for sensing applications

The main requirements for sensing applications are that the detection is sensitive and selective.^[75] However, graphene is intrinsically chemically inert due to its large aromatic sp^2 carbon lattice that is free of dangling bonds.^[46] The broad sensing potential of graphene can only be unlocked by the introduction of sensitizer (bio)molecules and structures, e.g. various inorganic groups,^[42, 76] organic or organometallic molecules,^[12, 77] DNAs,^[78] proteins,^[79] peptides,^[58b, 80] nanoparticles,^[81] and 2D heterostructure^[28b, 28c, 35c, 82]. These molecules are able to respond chemically or physically to their nearby environment, whose responses could then be transduced into an appreciable change in the conductivity of the carbon-based honeycomb scaffold. The introduction of such chemical moieties on the graphene surface or edge is often referred to as graphene functionalization.^[83] Chemical functionalization of graphene is commonly achieved using either covalent or non-covalent strategies. The resulting graphene materials contain specific recognition moieties for biochemical sensing, but still share, to a large extent, the same carbon honeycomb backbone and the electrical properties, especially the field effect, of graphene. Typically, covalent approaches modify the graphene surface with various functional (bio)chemical molecules^[84] by reacting with the sp^2 carbon centers in the aromatic lattice, introducing sp^3 centers at the reaction sites. Precautions have to be taken because chemical modification reduces the flatness, but more importantly, destroys the aromaticity of the graphene lattice and renders the modified material inferior in terms of electrical mobility compared to pristine graphene. On the contrary, non-covalent approaches provide the opportunity to functionalize graphene without disrupting its intrinsic aromaticity.^[85]

1.3.1 Covalent functionalization

Covalent chemical modification of graphene allows engineering the properties of graphene to a large extent, particularly with the scope of band gap engineering, surface modification, and bio-interfacing.^[83a] Introducing atomic hydrogen or fluorine into the honeycomb scaffold, reveals the possibility to continuously transform this highly conductive zero-band gap semimetal into an insulator known as graphane^[76a] (Figure 1.5a) or 2D Teflon,^[76b, 76c] as initially proposed by the Manchester group. Regarding sensing applications, calculations showed that (partially) hydrogenated graphene has a high affinity for NO_2 ,^[86] while graphane doped with Li atoms was predicted to be sensitive to H_2S and NH_3 .^[87] Moreover, the reduced carrier mobility of highly hydrogenated graphene is still sufficient for sensor applications.^[88]

Fluorographene, on the other hand, was applied for the detection of ammonia^[89] and ascorbic acid and uric acid.^[90] The fluorine-enriched material could also be further functionalized with thiol groups for genosensing.^[91] Underlying mechanisms and selectivity of the sensor are still under debate.

Separately, graphene sheets are now routinely covalently modified with oxygen functional groups (e.g. carboxyl, hydroxyl and epoxy moieties, see also Figure 1.5b) by using oxidative reactions, forming graphene oxide (GO), a material known since the early 1960s.^[92] The synthetic process consists in dispersing graphite into stable single layer GO and is suitable for large scale production of dispersible single layer graphene using a thermal or chemical reduction step. The resulting material is often referred to as reduced GO, or rGO.^[93] Remarkably, when used as an active sensing electrode, GO and rGO usually show improved sensing responses, presumably due to the large concentration of defects compared to near defect-free single layer graphene obtained via mechanical exfoliation of graphite.^[42, 94] One of the first works on rGO as an active material for high-performance molecular sensing describes a conductance change of the rGO networks upon exposure to trace levels of vapor (including three main classes of chemical-warfare agents and an explosive at parts-per-billion concentrations).^[42] It was shown that the optimal defect density should balance the gains in the sensor response against the rapid degradation in low frequency $1/f$ noise due to the increased density of defects.^[42] The difficulties in controlling the density of the defect as well as the lack of knowledge on the nature of the defect, however, represents significant limitations for utilizing GO or rGO for sensing applications. Reactive oxygen-rich groups, inherently present on rGO, can be exploited to synthetically conjugate the material with various chemical or biological groups.^[84] A viable synthetic strategy is depicted in Figure 1.5b: a GO-polyethylene glycol dispersion (i.e., PEGylated GO) was prepared; the hydrophilic six-armed PEG-NH₂ could then be labelled by conjugating an antibody (for potential antibody-antigen detection^[84]).

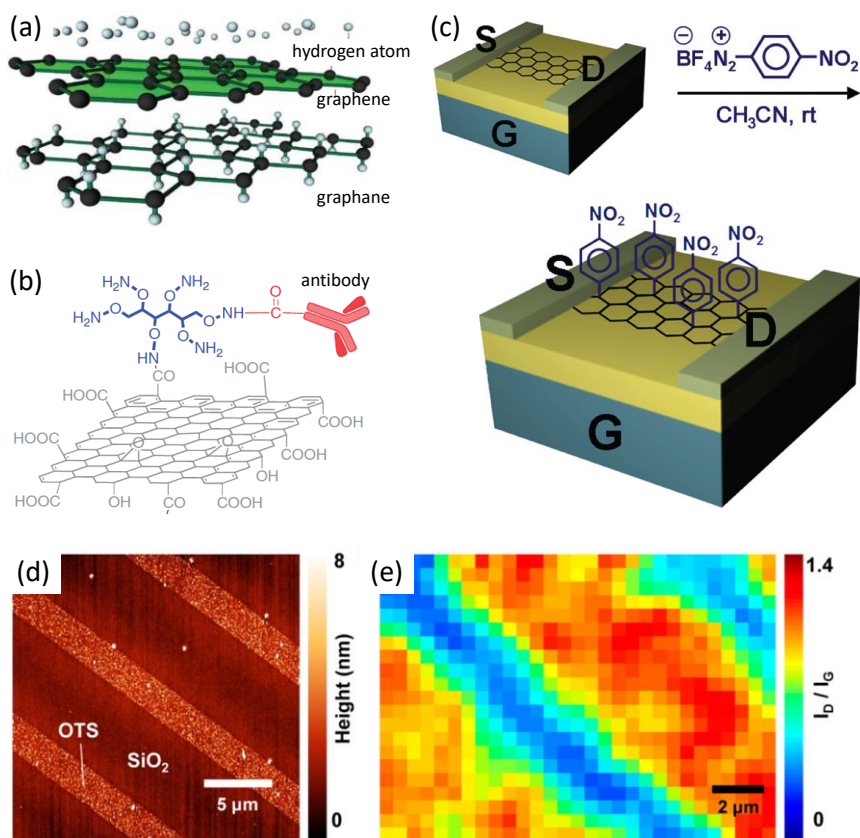


Figure 1.5 Covalent functionalization of graphene. a) Chemical modification of a graphene layer (in green) with cold plasma hydrogen atoms produces graphane.^[76a] b) Bioconjugation of PEGylated GO with antibody.^[92] c) Schematic of the chemical functionalization of a GFET devices with 4-nitrobenzene diazonium tetrafluoroborate (4-NBD).^[95] d) AFM image of octadecyltrichlorosilane (OTS) lines patterned on SiO₂ surface. e) Raman mapping of I_D/I_G for graphene after 4-NBD reactions: 10mM 4-NBD in aqueous solution with 0.5 wt% sodium dodecyl sulfate (SDS) at 35°C for 1.5 h.^[96]

Hydrogenated graphene, fluorinated graphene (or halogenated graphene^[97] in general), and GO (or rGO) are the few examples of materials that resulted from covalent modification of the graphene scaffold. Instead of providing an extensive list of the methods available to induce such modifications, more focus will be on discussing a grafting strategy, frequently applied to covalently attach chemical moieties to graphene surface (or edges) usually proceeds via free-radical reactions.^[65, 66b, 83a, 96, 98] Graphene grafting uses alkyl or aryl diazonium salts as grafting agents, where the diazonium salt precursor is first chemically or electrochemically reduced (liberating nitrogen gas), to form a reactive alkyl or aryl radical that reacts with the aromatic system of the graphene sheet (the conductive channel of the transistor

device fabricated on a 200 nm SiO₂/highly doped Si substrate as shown in Figure 1.5c).^[95] The disruption of the aromatic system by transformation of carbon atoms from *sp*² to *sp*³ hybridization results in a remarkable decrease in graphene conductivity, which can be controlled by reaction time. The reaction efficiency depends on several parameters: the number of graphene layers,^[66b] the electrostatic environment,^[98c] and the defect density on the graphene surface.^[98d] A previous study exploited the graphene reactivity, induced by electrostatic charge doping on different substrates using reactivity imprint lithography (RIL).^[98c] The RIL technique made use of a polydimethylsiloxane (PDMS) stamp to pattern octadecyltrichlorosilane (OTS) lines on a SiO₂/Si substrate (Figure 1.5d). During the electrografting of graphene with 4-nitrobenzene diazonium tetrafluoroborate (4-NBD),^[96] bare SiO₂-supported graphene showed a stronger reactivity with the diazonium salt than graphene resting on OTS-protected SiO₂ (Figure 1.5e). OTS increases the distance between the graphene sheet and the charged impurities in the SiO₂ substrate, rendering the portion of graphene resting on it less reactive to the 4-NBD.^[98c] Similarly, in case of GO (or rGO), grafting chemistries are best represented by localized reactivity of the carboxyl, carbonyl, and other oxygen-containing groups by substitution reactions.^[98d]

1.3.2 Non-covalent functionalization

Non-covalent functionalization have the major advantage of fully preserving the graphene lattice (i.e., the aromaticity), and thus the electrical performances. In addition, non-covalent bond can also be quite strong. For example, the π - π interactions of graphene-benzene and naphthalene result in a considerable binding energy of almost 0.1 eV per carbon atom; consistently, the binding energy of graphene-TTP (tetraphenylporphyrin) was calculated to be 3.2 eV, i.e., $\approx 90\%$ of a typical C-C covalent binding energy (≈ 3.6 eV).^[99] Given the aforementioned advantages, it is a common approach to anchor a molecule onto the graphene surface using an aromatic linker group via noncovalent bonds with excellent sensing performance in aqueous solutions.^[83a] Still, it is of note here that non-covalent functionalization is expected to be less compatible with long term usage, at least if compared to stronger covalent functionalization (although the covalent modifications of graphene inevitably lead to a severe degradation in the electrical properties). Nevertheless, non-covalent functionalization could also be an asset if the sensor surface has to be regenerated, for example, for recycling the sensor devices.

In general, non-covalent graphene functionalization approaches can be classified based on their corresponding intermolecular interactions, including π - π or hydrophobic stacking, electrostatic interaction, and van der Waals interaction.^[83a] The self-assembly process of these molecules on the surface of graphene could be

highly controlled and accurately characterized in favor of actual sensor design.^[83] For example, Figure 1.6a shows a scanning tunneling microscopy (STM) image of well-ordered aromatic perylene-3,4,9,10-tetracarboxylic-3,4,9,10-dianhydride (PTCDA) molecules on graphene (as indicated by the **a** and **b** vectors), where π - π interaction are the driving force of the self-assembly.^[77b] The perylene-based monolayer is stable and robust even when exposed to ambient conditions. π - π or hydrophobic interactions between aromatic surface and nucleic acid moieties can also facilitate the decoration of graphene surface with single-stranded DNA (ssDNA) as shown in Figure 1.6b (right panel, highly oriented pyrolytic graphite (HOPG) was applied in this case).^[100] This strong non-specific ssDNA adsorption can be avoided by first self-assembling a monolayer of pyrene ethylene glycol, thus rendering the surface of graphene hydrophilic and preventing ssDNA adsorption via hydrophobic interactions (left panel, Figure 1.6b). Besides DNA, proteins^[79] or peptides^[80a, 80b] containing aromatic moieties could also self-assemble on a graphene scaffold. As illustrated in Figure 1.6c, the incubation of graphene with the peptides resulted in the formation of a uniform mesh-like layer whilst silicon oxide surface was unaffected. This indicates that the adsorption occurred specifically on graphene.^[80b]

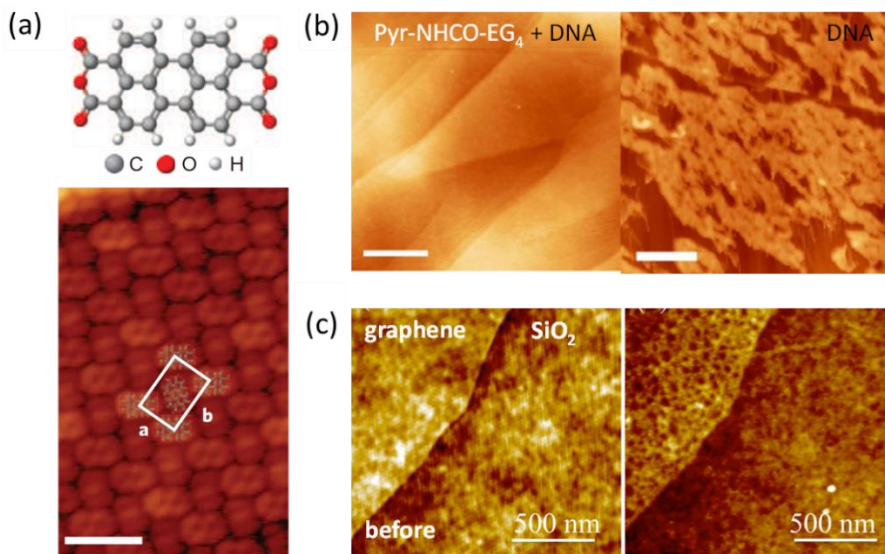


Figure 1.6 Non-covalent functionalization of graphene. a) STM image of a self-assembled monolayer of an aromatic molecule (peryene-3,4,9,10-tetracarboxylic-3,4,9,10-dianhydride, PTCDA) (gas-phase deposition) on a graphene surface (scale bar is 3 nm). Upper panel: molecular structure of PTCDA.^[77b] b) Left panel: AFM of highly oriented pyrolytic graphite (HOPG) incubated for 5 min with a solution of 3 M KCl and 8 M urea and rinsed with ultrapure water (scale bar is 200 nm). Right panel: HOPG incubated for 5 min with single-stranded M13 DNA ($10 \text{ ng } \mu\text{l}^{-1}$) in the same buffer (scale bar is 200 nm).^[100] c) AFM topographic image of graphene before (left panel) and after (right panel) incubation with the peptide.^[80b]

Electrostatic interaction is another driving force of the non-covalent assembly. For instance, voltage-biased graphene can act as an electrophoretic electrode for immobilization of charged molecules. The subsequent detection of complementary analysts can be achieved by using the same graphene transistor devices.^[17, 77h, 101]

As suggested by Geim and co-workers,^[82] weak van der Waals-like interaction between layers could be exploited to sandwich (a process called ‘encapsulation’) graphene with other 2D layers of, e.g. MoS₂, mica, or hexagonal boron nitride (h-BN). This innovative technique allows the formation of unprecedented multilayer heterostructures that may be used in devices with adjustable and astonishing electronic properties. For example, by encapsulating graphene in a h-BN stacking layer, researchers managed to obtain very high electric performances GFETs, including an exceptionally high carrier mobility of 140,000 cm² V⁻¹ s⁻¹ at room temperature, which is close to the theoretical limit as imposed by acoustic phonon scattering. This extremely high mobility could be ascribed to very clean interfaces above and below graphene and effective screening of all the defects.^[28a] Very recently, even higher mobilities, up to a staggering 197,600 cm² V⁻¹ s⁻¹ and 350,000 cm² V⁻¹ s⁻¹, have been observed for hBN-sandwiched graphene samples.^[28c, 35c] One could also explore various 2D crystals as active sensing elements, MoS₂ or h-BN capped MoS₂,^[29, 102] for instance. Please note that even in a stack such as encapsulated graphene, the encapsulating layers can be functionalized in the quest of sensing (with the requirement that the encapsulating layer is sufficiently thin).

As previously discussed, chemical functionalization is essential for unlocking the sensing potential of graphene surface, but important is also to realize that chemical functionalization also plays a critical role in passivating the surface of graphene. Surface passivation against unwanted non-specific binding (pyrene ethylene glycol to prevent any hydrophobic interactions,^[100] for example) is crucial to achieve very low detection limits in the presence of high ionic background levels and to avoid false positives when complex biological samples are assayed.^[103]

Importantly, the transfer of large and clean (and crack- and fold-free) graphene sheets is still a critical challenge. Long chain polymers including poly(methyl methacrylate) (PMMA) – conventionally used for transferring two-dimensional materials – irreversibly adsorb on the graphene surface, yielding a range of contaminations with unwanted chemical functions.^[104] It is therefore a necessity to take into account the influences of these possible polymer residues as they impede the functionalization of the graphene surface (which is actually not always discussed, nor clarified in the literature). There is therefore also a large demand for decent polymer-free transfer methods.^[105]

1.4 Aims and outline

Graphene as a 2D surface with unique band structure, extraordinary high mobility and versatile (electro-)chemical reactivity has great potential and advantages for sensing applications. The thesis aims to understand at a fundamental level the electrical, electrochemical and mechanical properties of graphene surface upon chemical modifications, and thus using these properties for sensing applications.

In chapter 2, the electrical transport properties and electrochemical kinetics of graphene upon hydrogenation are discussed. As the electronic density of states (DOS) is closely related to both the electrical and electrochemical properties, the correlations between the DOS, quantum capacitance and the heterogeneous electron transfer rate were established and discussed. Furthermore, by correlating the charged impurity density and the density of hydrogenated defects, hydrogenation treatment via the mild hydrogen plasma was found to clean the graphene lattice by removing airborne hydrocarbons.

In Chapter 3, nitrogen atoms were incorporated into graphene lattice using an ammonia plasma to study the electrocatalysis of oxygen reduction reaction (ORR). Nitrogen doping sites in graphene, as generally believed to be the active sites for ORR, were found not to be responsible for the activity improvement. Instead, oxygen containing groups which coexist with the nitrogen dopants at graphene surface are at the origin of the enhanced ORR activity.

The 2D nature of graphene makes its surface chemistry very sensitive to the environment. Chapter 4 reveals the enhanced surface cleanliness of graphene using hydrogenation treatment. Characterization by multiscale surface spectroscopy techniques showed that hydrogenation is able to remove hydrocarbons contaminations from the surface of graphene. As compared to pristine graphene, hydrogenation induced more water adsorption that forms a layer protecting the graphene surface from airborne contaminants.

Surface chemistry modification not only alters the electrical and electrochemical properties, but also exerts significant impact on the mechanical properties of graphene. In Chapter 5, the mechanical strength of centimeter-scale graphene via a biaxial compression method is investigated. When graphene floats on water, the natural perturbations of graphene remain untouched, which provides a unique strategy to evaluate the in-plane stiffness of graphene. In the framework of the anharmonic coupling the stretching and flexural modes, the mechanical stiffness of graphene is proven to be very sensitive to lattice defects including hydrogenation and

vacancy.

Hydrogenated and nitrogenated graphene are used for field effect detection of a range of gas in Chapter 6. Compared to pristine graphene, the chemically modified graphene exhibits p-doping behaviors and improved sensing responses with low selectivity. Upon continuous gas detection, the graphene devices tend to show saturated and then decreased responses due to the reduction of active adsorption sites caused by trapped gas molecules. Further exploration suggests that p-doping in the modified graphene is positively correlated to the enhanced sensitivity of graphene to gas detection.

1.6 References

- [1] A. K. Geim, K. S. Novoselov, *Nat. Mater.* **2007**, 6, 183.
- [2] Y. Wu, D. B. Farmer, F. Xia, P. Avouris, *Proc. IEEE* **2013**, 101, 1620.
- [3] a) A. A. Balandin, *Nat. Nanotechnol.* **2013**, 8, 549; b) Z. Cheng, Q. Li, Z. Li, Q. Zhou, Y. Fang, *Nano Lett.* **2010**, 10, 1864.
- [4] Q. He, S. Wu, Z. Yin, H. Zhang, *Chem. Sci.* **2012**, 3, 1764.
- [5] S. Wu, Q. He, C. Tan, Y. Wang, H. Zhang, *Small* **2013**, 9, 1160.
- [6] C. T. Lin, P. T. K. Loan, T. Y. Chen, K. K. Liu, C. H. Chen, K. H. Wei, L. J. Li, *Adv. Funct. Mater.* **2013**, 23, 2301.
- [7] S. Chen, Z.-B. Zhang, L. Ma, P. Ahlberg, X. Gao, Z. Qiu, D. Wu, W. Ren, H.-M. Cheng, S.-L. Zhang, *Appl. Phys. Lett.* **2012**, 101, 154106.
- [8] W. Fu, C. Nef, A. Tarasov, M. Wipf, R. Stoop, O. Knopfmacher, M. Weiss, M. Calame, C. Schönenberger, *Nanoscale* **2013**, 5, 12104.
- [9] K. S. Novoselov, A. K. Geim, S. V. Morozov, D. Jiang, Y. Zhang, S. V. Dubonos, I. V. Grigorieva, A. A. Firsov, *Science* **2004**, 306, 666.
- [10] a) F. Schedin, A. Geim, S. Morozov, E. Hill, P. Blake, M. Katsnelson, K. Novoselov, *Nat. Mater.* **2007**, 6, 652; b) Y. Ohno, K. Maehashi, K. Matsumoto, presented at Micro-and Nanotechnology Sensors, Systems, and Applications III **2011**; c) I. Heller, S. Chatoor, J. Männik, M. A. Zevenbergen, C. Dekker, S. G. Lemay, *J. Am. Chem. Soc.* **2010**, 132, 17149.
- [11] Y. Dan, Y. Lu, N. J. Kybert, Z. Luo, A. C. Johnson, *Nano Lett.* **2009**, 9, 1472.
- [12] W. Fu, C. Nef, A. Tarasov, M. Wipf, R. Stoop, O. Knopfmacher, M. Weiss, M. Calame, C. Schönenberger, *Nanoscale* **2013**, 5, 12104.
- [13] a) J. L. Xia, F. Chen, J. H. Li, N. J. Tao, *Nat. Nanotechnol.* **2009**, 4, 505; b) S. Luryi, *Appl. Phys. Lett.* **1988**, 52, 501.
- [14] J. O. Bockris, E. Gileadi, K. Muller, *J. Chem. Phys.* **1966**, 44, 1445.
- [15] V. M. Aguilera, J. Pellicer, M. Aguilera-Arzo, *Langmuir* **1999**, 15, 6156.

- [16] a) P. Bergveld, *Sensor. Actuat. B* **2003**, 88, 1; b) P. Bergveld, *IEEE Trans. Biomed. Eng.* **1970**, Bm17, 70.
- [17] G. Y. Xu, J. Abbott, L. Qin, K. Y. M. Yeung, Y. Song, H. Yoon, J. Kong, D. Ham, *Nat. Commun.* **2014**, 5, 4866.
- [18] J. J. Gooding, *Small* **2006**, 2, 313.
- [19] X. P. A. Gao, G. F. Zheng, C. M. Lieber, *Nano Lett.* **2010**, 10, 547.
- [20] G. S. Kulkarni, Z. H. Zhong, *Nano Lett.* **2012**, 12, 719.
- [21] K. S. Chang, C. C. Chen, J. T. Sheu, Y. K. Li, *Sensor. Actuat. B* **2009**, 138, 148.
- [22] C. T. Lin, P. T. K. Loan, T. Y. Chen, K. K. Liu, C. H. Chen, K. H. Wei, L. J. Li, *Adv. Funct. Mater.* **2013**, 23, 2301.
- [23] S. Chen, Z. B. Zhang, L. P. Ma, P. Ahlberg, X. D. Gao, Z. J. Qiu, D. P. Wu, W. C. Ren, H. M. Cheng, S. L. Zhang, *Appl. Phys. Lett.* **2012**, 101, 154106.
- [24] V. Singh, D. Joung, L. Zhai, S. Das, S. I. Khondaker, S. Seal, *Prog. Mater. Sci.* **2011**, 56, 1178.
- [25] a) E. W. Hill, A. Vijayaragahvan, K. Novoselov, *IEEE Sens. J.* **2011**, 11, 3161; b) H. C. Cheng, R. J. Shiue, C. C. Tsai, W. H. Wang, Y. T. Chen, *ACS Nano* **2011**, 5, 2051.
- [26] E. Stern, J. F. Klemic, D. A. Routenberg, P. N. Wyrembak, D. B. Turner-Evans, A. D. Hamilton, D. A. LaVan, T. M. Fahmy, M. A. Reed, *Nature* **2007**, 445, 519.
- [27] F. Schedin, A. K. Geim, S. V. Morozov, E. W. Hill, P. Blake, M. I. Katsnelson, K. S. Novoselov, *Nat. Mater.* **2007**, 6, 652.
- [28] a) L. Wang, I. Meric, P. Y. Huang, Q. Gao, Y. Gao, H. Tran, T. Taniguchi, K. Watanabe, L. M. Campos, D. A. Muller, J. Guo, P. Kim, J. Hone, K. L. Shepard, C. R. Dean, *Science* **2013**, 342, 614; b) D. H. Tien, J.-Y. Park, K. B. Kim, N. Lee, T. Choi, P. Kim, T. Taniguchi, K. Watanabe, Y. Seo, *ACS Appl. Mater. Interfaces* **2016**, 8, 3072; c) G. Auton, J. Zhang, R. K. Kumar, H. Wang, X. Zhang, Q. Wang, E. Hill, A. Song, *Nat. Commun.* **2016**, 7, 11670.
- [29] G. Liu, S. L. Romyantsev, C. Jiang, M. S. Shur, A. A. Balandin, *IEEE Electron Device Lett.* **2015**, 36, 1202.

- [30] a) K. S. Kim, Y. Zhao, H. Jang, S. Y. Lee, J. M. Kim, K. S. Kim, J. H. Ahn, P. Kim, J. Y. Choi, B. H. Hong, *Nature* **2009**, 457, 706; b) X. S. Li, W. W. Cai, J. H. An, S. Kim, J. Nah, D. X. Yang, R. Piner, A. Velamakanni, I. Jung, E. Tutuc, S. K. Banerjee, L. Colombo, R. S. Ruoff, *Science* **2009**, 324, 1312.
- [31] A. W. Tsen, L. Brown, M. P. Levendorf, F. Ghahari, P. Y. Huang, R. W. Havener, C. S. Ruiz-Vargas, D. A. Muller, P. Kim, J. Park, *Science* **2012**, 336, 1143.
- [32] a) *SIGMA-ALDRICH*, Graphene field effect transistor chip, **2016**, <http://www.sigmaaldrich.com/technical-documents/articles/materials-science/graphene-field-effect-transistors.html#newMaterials>, DOI: <http://www.sigmaaldrich.com/catalog/product/aldrich/803995?lang=en®ion=NL>; b) *L. BGT Materials Limited*, Grat-FET™, **2015**, http://bgtmaterials.com/uploads/BGT%20Materials%20Limited_Grat%20FET_Data%20Sheet%2017Jun2015.pdf.
- [33] H. S. Song, S. L. Li, H. Miyazaki, S. Sato, K. Hayashi, A. Yamada, N. Yokoyama, K. Tsukagoshi, *Sci. Rep.* **2012**, 2, 337.
- [34] a) Z. Yan, Z. W. Peng, J. M. Tour, *Acc. Chem. Res.* **2014**, 47, 1327; b) T. R. Wu, X. F. Zhang, Q. H. Yuan, J. C. Xue, G. Y. Lu, Z. H. Liu, H. S. Wang, H. M. Wang, F. Ding, Q. K. Yu, X. M. Xie, M. H. Jiang, *Nat. Mater.* **2016**, 15, 43.
- [35] a) K. H. Lee, H. J. Shin, J. Lee, I. Y. Lee, G. H. Kim, J. Y. Choi, S. W. Kim, *Nano Lett.* **2012**, 12, 714; b) N. Petrone, C. R. Dean, I. Meric, A. M. van der Zande, P. Y. Huang, L. Wang, D. Muller, K. L. Shepard, J. Hone, *Nano Lett.* **2012**, 12, 2751; c) L. Banszerus, M. Schmitz, S. Engels, J. Dauber, M. Oellers, F. Haupt, K. Watanabe, T. Taniguchi, B. Beschoten, C. Stampfer, *Sci Adv* **2015**, 1, e1500222.
- [36] F. Hooge, T. Kleinpenning, L. Vandamme, *Rep. Prog. Phys.* **1981**, 44, 479.
- [37] a) N. K. Rajan, D. A. Routenberg, M. A. Reed, *Appl. Phys. Lett.* **2011**, 98, 264107; b) G. Liu, S. Rumyantsev, M. S. Shur, A. A. Balandin, *Appl. Phys. Lett.* **2013**, 102, 093111.
- [38] Y.-M. Lin, P. Avouris, *Nano Lett.* **2008**, 8, 2119.
- [39] M. A. Stolyarov, G. X. Liu, S. L. Rumyantsev, M. Shur, A. A. Balandin, *Appl. Phys. Lett.* **2015**, 107, 023106.
- [40] L. H. Hess, M. Seifert, J. A. Garrido, *Proc. IEEE* **2013**, 101, 1780.

- [41] G. X. Liu, S. Rumyantsev, M. S. Shur, A. A. Balandin, *Appl. Phys. Lett.* **2013**, 102, 093111.
- [42] J. T. Robinson, F. K. Perkins, E. S. Snow, Z. Q. Wei, P. E. Sheehan, *Nano Lett.* **2008**, 8, 3137.
- [43] G. Liu, W. Stillman, S. Rumyantsev, Q. Shao, M. Shur, A. A. Balandin, *Appl. Phys. Lett.* **2009**, 95, 033103.
- [44] N. K. Rajan, K. Brower, X. X. Duan, M. A. Reed, *Appl. Phys. Lett.* **2014**, 104, 084106.
- [45] S. Sorgenfrei, C. Y. Chiu, M. Johnston, C. Nuckolls, K. L. Shepard, *Nano Lett.* **2011**, 11, 3739.
- [46] W. Y. Fu, C. Nef, O. Knopfnacher, A. Tarasov, M. Weiss, M. Calame, C. Schonenberger, *Nano Lett.* **2011**, 11, 3597.
- [47] Y. Y. Shao, J. Wang, H. Wu, J. Liu, I. A. Aksay, Y. H. Lin, *Electroanalysis* **2010**, 22, 1027.
- [48] M. D. Stoller, S. Park, Y. Zhu, J. An, R. S. Ruoff, *Nano Lett.* **2008**, 8, 3498.
- [49] W. J. Royea, T. W. Hamann, B. S. Brunschwig, N. S. Lewis, *J. Phys. Chem. B* **2006**, 110, 19433.
- [50] R. L. McCreery, *Chem. Rev.* **2008**, 108, 2646.
- [51] W. Yuan, Y. Zhou, Y. Li, C. Li, H. Peng, J. Zhang, Z. Liu, L. Dai, G. Shi, *Sci. Rep.* **2013**, 3, 2248.
- [52] J.-H. Zhong, J. Zhang, X. Jin, J.-Y. Liu, Q. Li, M.-H. Li, W. Cai, D.-Y. Wu, D. Zhan, B. Ren, *J. Am. Chem. Soc.* **2014**, 136, 16609.
- [53] a) Y. Wang, Y. Shao, D. W. Matson, J. Li, Y. Lin, *ACS Nano* **2010**, 4, 1790; b) O. Akhavan, E. Ghaderi, R. Rahighi, *ACS Nano* **2012**, 6, 2904; c) J. Guo, T. Zhang, C. Hu, L. Fu, *Nanoscale* **2015**, 7, 1290; d) V. Urbanová, F. Karlický, A. Matěj, F. Šembera, Z. Janoušek, J. A. Perman, V. Ranc, K. Čépe, J. Michl, M. Otyepka, *Nanoscale* **2016**, 8, 12134.
- [54] a) C. Ruan, W. Shi, H. Jiang, Y. Sun, X. Liu, X. Zhang, Z. Sun, L. Dai, D. Ge, *Sens. Actuators. B* **2013**, 177, 826; b) B. Unnikrishnan, S. Palanisamy, S.-M. Chen, *Biosens. Bioelectron.* **2013**, 39, 70.

- [55] S. S. J. Aravind, T. T. Baby, T. Arockiadoss, R. B. Rakhi, S. Ramaprabhu, *Thin Solid Films* **2011**, 519, 5667.
- [56] a) Y. Guo, Y. Guo, C. Dong, *Electrochim. Acta* **2013**, 113, 69; b) K.-J. Huang, Y.-J. Liu, H.-B. Wang, T. Gan, Y.-M. Liu, L.-L. Wang, *Sens. Actuators. B* **2014**, 191, 828; c) Y. Ni, P. Wang, H. Song, X. Lin, S. Kokot, *Anal. Chim. Acta* **2014**, 821, 34; d) L. Zhu, L. Luo, Z. Wang, *Biosens. Bioelectron.* **2012**, 35, 507.
- [57] a) B. Jin, P. Wang, H. Mao, B. Hu, H. Zhang, Z. Cheng, Z. Wu, X. Bian, C. Jia, F. Jing, *Biosens. Bioelectron.* **2014**, 55, 464; b) F. Liu, K. S. Choi, T. J. Park, S. Y. Lee, T. S. Seo, *BioChip J.* **2011**, 5, 123; c) Z. Wang, F. Li, J. Xia, L. Xia, F. Zhang, S. Bi, G. Shi, Y. Xia, J. Liu, Y. Li, *Biosens. Bioelectron.* **2014b**, 61, 391.
- [58] a) Y. Wang, Z. Li, D. Hu, C.-T. Lin, J. Li, Y. Lin, *J. Am. Chem. Soc.* **2010**, 132, 9274; b) L. Feng, Y. Chen, J. Ren, X. Qu, *Biomaterials* **2011**, 32, 2930.
- [59] A. Muthurasu, V. Ganesh, *Appl. Biochem. Biotechnol.* **2014**, 174, 945.
- [60] a) J. C. Claussen, A. Kumar, D. B. Jaroch, M. H. Khawaja, A. B. Hibbard, D. M. Porterfield, T. S. Fisher, *Adv. Funct. Mater.* **2012**, 22, 3399; b) D. Pan, Y. Gu, H. Lan, Y. Sun, H. Gao, *Anal. Chim. Acta* **2015**, 853, 297; c) Z. Yang, Y. Cao, J. Li, Z. Jian, Y. Zhang, X. Hu, *Anal. Chim. Acta* **2015**, 871, 35.
- [61] Y. Yang, M. Kang, S. Fang, M. Wang, L. He, J. Zhao, H. Zhang, Z. Zhang, *Sens. Actuators. B* **2015**, 214, 63.
- [62] W. Li, C. Tan, M. A. Lowe, H. D. Abruna, D. C. Ralph, *ACS Nano* **2011**, 5, 2264.
- [63] S. Banerjee, J. Shim, J. Rivera, X. Jin, D. Estrada, V. Solovyeva, X. You, J. Pak, E. Pop, N. Aluru, *ACS Nano* **2012**, 7, 834.
- [64] a) C. Tan, J. n. Rodríguez-López, J. J. Parks, N. L. Ritzert, D. C. Ralph, H. c. D. Abruña, *ACS Nano* **2012**, 6, 3070; b) N. L. Ritzert, J. Rodríguez-López, C. Tan, H. c. D. Abruña, *Langmuir* **2013**, 29, 1683; c) A. G. Guell, A. S. Cuharuc, Y. R. Kim, G. H. Zhang, S. Y. Tan, N. Ebejer, P. R. Unwin, *ACS Nano* **2015**, 9, 3558.
- [65] A. Bellunato, H. Arjmandi Tash, Y. Cesa, G. F. Schneider, *ChemPhysChem* **2016**, 17, 785.
- [66] a) R. Sharma, J. H. Baik, C. J. Perera, M. S. Strano, *Nano Lett.* **2010**, 10, 398; b) F. M. Koehler, A. Jacobsen, K. Ensslin, C. Stampfer, W. J. Stark, *Small* **2010**, 6, 1125; c) K. S. Mali, J. Greenwood, J. Adisojoso, R. Phillipson, S. De Feyter,

- Nanoscale* **2015**, 7, 1566; d) K. Yong-Jin, K. Yuna, N. Konstantin, H. Byung Hee, *2D Mater.* **2015**, 2, 042001; e) A. Criado, M. Melchionna, S. Marchesan, M. Prato, *Angew. Chem. Int. Ed.* **2015**, 54, 10734.
- [67] C. Z. Liao, M. Zhang, L. Y. Niu, Z. J. Zheng, F. Yan, *J. Mater. Chem. B* **2014**, 2, 191.
- [68] S. K. Singh, K. Takeyasu, J. Nakamura, *Adv. Mater.* **2018**, 31, 1804297.
- [69] a) K. Gong, F. Du, Z. Xia, M. Durstock, L. Dai, *Science* **2009**, 323, 760; b) J. Shui, M. Wang, F. Du, L. Dai, *Sci. Adv.* **2015**, 1, e1400129; c) Y. Ito, H. J. Qiu, T. Fujita, Y. Tanabe, K. Tanigaki, M. Chen, *Adv. Mater.* **2014**, 26, 4145; d) L. Qu, Y. Liu, J.-B. Baek, L. Dai, *ACS Nano* **2010**, 4, 1321.
- [70] M. Shao, Q. Chang, J.-P. Dodelet, R. Chenitz, *Chem. Rev.* **2016**, 116, 3594.
- [71] a) D. Guo, R. Shibuya, C. Akiba, S. Saji, T. Kondo, J. Nakamura, *Science* **2016**, 351, 361; b) H. B. Yang, J. Miao, S.-F. Hung, J. Chen, H. B. Tao, X. Wang, L. Zhang, R. Chen, J. Gao, H. M. Chen, *Sci. Adv.* **2016**, 2, e1501122; c) L. Lai, J. R. Potts, D. Zhan, L. Wang, C. K. Poh, C. Tang, H. Gong, Z. Shen, J. Lin, R. S. Ruoff, *Energy Environ. Sci.* **2012**, 5, 7936; d) T. Wang, Z.-X. Chen, Y.-G. Chen, L.-J. Yang, X.-D. Yang, J.-Y. Ye, H.-P. Xia, Z.-Y. Zhou, S.-G. Sun, *ACS Energy Lett.* **2018**, 3, 986.
- [72] a) H.-W. Liang, X. Zhuang, S. Brüller, X. Feng, K. Müllen, *Nat. Commun.* **2014**, 5, 4973; b) W. Ding, Z. Wei, S. Chen, X. Qi, T. Yang, J. Hu, D. Wang, L. J. Wan, S. F. Alvi, L. Li, *Angew. Chem. Int. Ed.* **2013**, 52, 11755.
- [73] a) Z. Luo, S. Lim, Z. Tian, J. Shang, L. Lai, B. MacDonald, C. Fu, Z. Shen, T. Yu, J. Lin, *J. Mater. Chem.* **2011**, 21, 8038; b) Y. Jia, L. Zhang, A. Du, G. Gao, J. Chen, X. Yan, C. L. Brown, X. Yao, *Adv. Mater.* **2016**, 28, 9532.
- [74] Y. Jia, L. Zhang, L. Zhuang, H. Liu, X. Yan, X. Wang, J. Liu, J. Wang, Y. Zheng, Z. Xiao, *Nat. Catal.* **2019**, 2, 688.
- [75] a) A. P. F. Turner, *Chem. Soc. Rev.* **2013**, 42, 3184; b) T. M. H. Lee, *Sensors* **2008**, 8, 5535; c) M. Y. Shen, B. R. Li, Y. K. Li, *Biosens. Bioelectron.* **2014**, 60, 101.
- [76] a) D. C. Elias, R. R. Nair, T. M. G. Mohiuddin, S. V. Morozov, P. Blake, M. P. Halsall, A. C. Ferrari, D. W. Boukhvalov, M. I. Katsnelson, A. K. Geim, K. S. Novoselov, *Science* **2009**, 323, 610; b) J. T. Robinson, J. S. Burgess, C. E.

Junkermeier, S. C. Badescu, T. L. Reinecke, F. K. Perkins, M. K. Zalalutdniov, J. W. Baldwin, J. C. Culbertson, P. E. Sheehan, E. S. Snow, *Nano Lett.* **2010**, 10, 3001; c) R. R. Nair, W. C. Ren, R. Jalil, I. Riaz, V. G. Kravets, L. Britnell, P. Blake, F. Schedin, A. S. Mayorov, S. J. Yuan, M. I. Katsnelson, H. M. Cheng, W. Strupinski, L. G. Bulusheva, A. V. Okotrub, I. V. Grigorieva, A. N. Grigorenko, K. S. Novoselov, A. K. Geim, *Small* **2010**, 6, 2877; d) J. S. Burgess, B. R. Matis, J. T. Robinson, F. A. Bulat, F. Keith Perkins, B. H. Houston, J. W. Baldwin, *Carbon* **2011**, 49, 4420; e) F. Withers, M. Dubois, A. K. Savchenko, *Phys. Rev. B* **2010**, 82, 073403; f) K.-I. Ho, C.-H. Huang, J.-H. Liao, W. Zhang, L.-J. Li, C.-S. Lai, C.-Y. Su, *Sci. Rep.* **2014**, 4, 5893; g) X. Zhang, A. Hsu, H. Wang, Y. Song, J. Kong, M. S. Dresselhaus, T. Palacios, *ACS Nano* **2013**, 7, 7262; h) B. Li, L. Zhou, D. Wu, H. Peng, K. Yan, Y. Zhou, Z. Liu, *ACS Nano* **2011**, 5, 5957; i) A. Wei, J. Wang, Q. Long, X. Liu, X. Li, X. Dong, W. Huang, *Mater. Res. Bull.* **2011**, 46, 2131; j) H. Feng, R. Cheng, X. Zhao, X. Duan, J. Li, *Nat. Commun.* **2013**, 4, 1539; k) X. Dong, Q. Long, A. Wei, W. Zhang, L.-J. Li, P. Chen, W. Huang, *Carbon* **2012**, 50, 1517; l) H. Zhang, E. Bekyarova, J.-W. Huang, Z. Zhao, W. Bao, F. Wang, R. C. Haddon, C. N. Lau, *Nano Lett.* **2011**, 11, 4047.

[77] a) X. C. Dong, D. L. Fu, W. J. Fang, Y. M. Shi, P. Chen, L. J. Li, *Small* **2009**, 5, 1422; b) Q. H. Wang, M. C. Hersam, *Nat. Chem.* **2009**, 1, 206; c) Y. Zhu, Y. Hao, E. A. Adogla, J. Yan, D. Li, K. Xu, Q. Wang, J. Hone, Q. Lin, *Nanoscale* **2016**, 8, 5815; d) F. M. Koehler, N. A. Luechinger, D. Ziegler, E. K. Athanassiou, R. N. Grass, A. Rossi, C. Hierold, A. Stemmer, W. J. Stark, *Angew. Chem. Int. Ed.* **2009**, 48, 224; e) T. F. v. Dijkman, *Copper trispyrazolylborate complexes for ethene detection*, Doctoral Thesis Leiden University, **2016**. Retrieved from <http://hdl.handle.net/1887/39518>; f) C. Li, K. Komatsu, S. Bertrand, G. Clavé, S. Campidelli, A. Filoramo, S. Guéron, H. Bouchiat, *Phys. Rev. B* **2016**, 93, 045403; g) X. Wang, J.-B. Xu, W. Xie, J. Du, *J. Phys. Chem. C* **2011**, 115, 7596; h) Y. Y. Wang, P. J. Burke, *Nano Res.* **2014**, 7, 1650.

[78] a) N. Dontschuk, A. Stacey, A. Tadich, K. J. Rietwyk, A. Schenk, M. T. Edmonds, O. Shimoni, C. I. Pakes, S. Prawer, J. Cervenka, *Nat. Commun.* **2015**, 6, 6563; b) N. S. Green, M. L. Norton, *Anal. Chim. Acta* **2015**, 853, 127; c) N. Mohanty, V. Berry, *Nano Lett.* **2008**, 8, 4469; d) A. R. Gao, N. L. Zou, P. F. Dai, N. Lu, T. Li, Y. L. Wang, J. L. Zhao, H. J. Mao, *Nano Lett.* **2013**, 13, 4123; e) C.-T. Lin, P. T. K. Loan, T.-Y. Chen, K.-K. Liu, C.-H. Chen, K.-H. Wei, L.-J. Li, *Adv. Funct. Mater.* **2013**, 23, 2301.

[79] a) J. Wang, H. Zhu, Y. Xu, W. Yang, A. Liu, F. Shan, M. Cao, J. Liu, *Sens. Actuators. B* **2015**, 220, 1186; b) Q. Guo, H. Zhu, F. Liu, A. Y. Zhu, J. C. Reed, F. Yi, E.

- Cubukcu, *ACS Photonics* **2014**, *1*, 221; c) M. B. Lerner, F. Matsunaga, G. H. Han, S. J. Hong, J. Xi, A. Crook, J. M. Perez-Aguilar, Y. W. Park, J. G. Saven, R. Liu, A. T. C. Johnson, *Nano Lett.* **2014**, *14*, 2709; d) S. Eissa, C. Tlili, L. L'Hocine, M. Zourob, *Biosens. Bioelectron.* **2012**, *38*, 308.
- [80] a) Y. Cui, S. N. Kim, S. E. Jones, L. L. Wissler, R. R. Naik, M. C. McAlpine, *Nano Lett.* **2010**, *10*, 4559; b) J. Katoch, S. N. Kim, Z. F. Kuang, B. L. Farmer, R. R. Nalk, S. A. Tatulian, M. Ishigami, *Nano Lett.* **2012**, *12*, 2342; c) L. Feng, L. Wu, J. Wang, J. Ren, D. Miyoshi, N. Sugimoto, X. Qu, *Adv. Mater.* **2012**, *24*, 125; d) H. Zhang, Y. Wang, D. Zhao, D. Zeng, J. Xia, A. Aldalbahi, C. Wang, L. San, C. Fan, X. Zuo, X. Mi, *ACS Appl. Mater. Interfaces* **2015**, *7*, 16152.
- [81] a) S. Li, X. Zhong, H. Yang, Y. Hu, F. Zhang, Z. Niu, W. Hu, Z. Dong, J. Jin, R. Li, J. Ma, *Carbon* **2011**, *49*, 4239; b) L.-M. Lu, H.-B. Li, F. Qu, X.-B. Zhang, G.-L. Shen, R.-Q. Yu, *Biosens. Bioelectron.* **2011**, *26*, 3500; c) J. Luo, S. Jiang, H. Zhang, J. Jiang, X. Liu, *Anal. Chim. Acta* **2012**, *709*, 47; d) B. C. Zhong, M. A. Uddin, A. Singh, R. Webb, G. Koley, *Appl. Phys. Lett.* **2016**, *108*, 093102; e) F. Jimenez-Villacorta, E. Climent-Pascual, R. Ramirez-Jimenez, J. Sanchez-Marcos, C. Prieto, A. de Andrés, *Carbon* **2016**, *101*, 305.
- [82] K. S. Novoselov, D. Jiang, F. Schedin, T. J. Booth, V. V. Khotkevich, S. V. Morozov, A. K. Geim, *Proc. Natl. Acad. Sci. U. S. A.* **2005**, *102*, 10451.
- [83] a) V. Georgakilas, M. Otyepka, A. B. Bourlinos, V. Chandra, N. Kim, K. C. Kemp, P. Hobza, R. Zboril, K. S. Kim, *Chem. Rev.* **2012**, *112*, 6156; b) F. Yan, M. Zhang, J. H. Li, *Adv. Healthcare Mater.* **2014**, *3*, 313.
- [84] K. Yang, L. Z. Feng, H. Hong, W. B. Cai, Z. Liu, *Nat. Protoc.* **2013**, *8*, 2392.
- [85] Z. X. Zhang, H. L. Huang, X. M. Yang, L. Zang, *J. Phys. Chem. Lett.* **2011**, *2*, 2897.
- [86] H. Tanveer, P. Puspamitra, A. Rajeev, *Nanotechnology* **2014**, *25*, 325501.
- [87] T. Hussain, P. Panigrahi, R. Ahuja, *Phys. Chem. Chem. Phys.* **2014**, *16*, 8100.
- [88] A. Y. S. Eng, Z. Sofer, P. Šimek, J. Kosina, M. Pumera, *Chem. Eur. J.* **2013**, *19*, 15583.
- [89] K. K. Tadi, S. Pal, T. N. Narayanan, *Sci. Rep.* **2016**, *6*, 25221.
- [90] X. Chia, A. Ambrosi, M. Otyepka, R. Zbořil, M. Pumera, *Chem. Eur. J.* **2014**, *20*, 6665.

- [91] V. Urbanová, K. Holá, A. B. Bourlinos, K. Čépe, A. Ambrosi, A. H. Loo, M. Pumera, F. Karlický, M. Otyepka, R. Zbořil, *Adv. Mater.* **2015**, 27, 2305.
- [92] H. P. Boehm, A. Clauss, U. Hofmann, G. O. Fischer, *Zeitschrift Für Naturforschung B* **1962**, B 17, 150.
- [93] D. A. Dikin, S. Stankovich, E. J. Zimney, R. D. Piner, G. H. B. Dommett, G. Evmenenko, S. T. Nguyen, R. S. Ruoff, *Nature* **2007**, 448, 457.
- [94] a) S. Seo, M. Min, J. Lee, T. Lee, S. Y. Choi, H. Lee, *Angew. Chem. Int. Ed.* **2012**, 51, 108; b) S. Borini, R. White, D. Wei, M. Astley, S. Haque, E. Spigone, N. Harris, J. Kivioja, T. Ryhanen, *ACS Nano* **2013**, 7, 11166; c) X. H. Zhang, Y. Zhang, Q. L. Liao, Y. Song, S. W. Ma, *Small* **2013**, 9, 4045.
- [95] A. Sinitskii, A. Dimiev, D. A. Corley, A. A. Fursina, D. V. Kosynkin, J. M. Tour, *ACS Nano* **2010**, 4, 1949.
- [96] F. M. Koehler, N. A. Luechinger, D. Ziegler, E. K. Athanassiou, R. N. Grass, A. Rossi, C. Hierold, A. Stemmer, W. J. Stark, *Angew. Chem. Int. Ed.* **2009**, 48, 224.
- [97] F. Karlicky, K. K. R. Datta, M. Otyepka, R. Zboril, *ACS Nano* **2013**, 7, 6434.
- [98] a) E. Bekyarova, M. E. Itkis, P. Ramesh, C. Berger, M. Sprinkle, W. A. de Heer, R. C. Haddon, *J. Am. Chem. Soc.* **2009**, 131, 1336; b) D. E. Jiang, B. G. Sumpter, S. Dai, *J. Phys. Chem. B* **2006**, 110, 23628; c) Q. H. Wang, Z. Jin, K. K. Kim, A. J. Hilmer, G. L. C. Paulus, C. J. Shih, M. H. Ham, J. D. Sanchez-Yamagishi, K. Watanabe, T. Taniguchi, J. Kong, P. Jarillo-Herrero, M. S. Strano, *Nat. Chem.* **2012**, 4, 724; d) G. L. C. Paulus, Q. H. Wang, M. S. Strano, *Acc. Chem. Res.* **2013**, 46, 160; e) F. M. Koehler, W. J. Stark, *Acc. Chem. Res.* **2013**, 46, 2297; f) R. K. Shervedani, A. Amini, N. Sadeghi, *Biosens. Bioelectron.* **2016**, 77, 478; g) C. S. Rao Vusa, V. Manju, S. Berchmans, P. Arumugam, *RSC Adv.* **2016**, 6, 33409; h) M. Mooste, E. Kibena, J. Kozlova, M. Marandi, L. Matisen, A. Niilisk, V. Sammelselg, K. Tammeveski, *Electrochim. Acta* **2015**, 161, 195.
- [99] S. D. Chakarova-Käck, E. Schröder, B. I. Lundqvist, D. C. Langreth, *Phys. Rev. Lett.* **2006**, 96, 146107.
- [100] G. F. Schneider, Q. Xu, S. Hage, S. Luik, J. N. H. Spoor, S. Malladi, H. Zandbergen, C. Dekker, *Nat. Commun.* **2013**, 4, 2619.
- [101] W. Sun, Y. Lu, Y. Wu, Y. Zhang, P. Wang, Y. Chen, G. Li, *Sens. Actuators. B* **2014**, 202, 160.

- [102] a) F. K. Perkins, A. L. Friedman, E. Cobas, P. M. Campbell, G. G. Jernigan, B. T. Jonker, *Nano Lett.* **2013**, 13, 668; b) B. Cho, M. G. Hahm, M. Choi, J. Yoon, A. R. Kim, Y. J. Lee, S. G. Park, J. D. Kwon, C. S. Kim, M. Song, Y. Jeong, K. S. Nam, S. Lee, T. J. Yoo, C. G. Kang, B. H. Lee, H. C. Ko, P. M. Ajayan, D. H. Kim, *Sci. Rep.* **2015**, 5, 8052.
- [103] a) L. Y. Feng, L. Wu, J. S. Wang, J. S. Ren, D. Miyoshi, N. Sugimoto, X. G. Qu, *Adv. Mater.* **2012**, 24, 125; b) J. P. Wang, B. J. Zou, J. Z. Rui, Q. X. Song, T. Kajiyama, H. Kambara, G. H. Zhou, *Microchim. Acta* **2015**, 182, 1095.
- [104] a) X. S. Li, Y. W. Zhu, W. W. Cai, M. Borysiak, B. Y. Han, D. Chen, R. D. Piner, L. Colombo, R. S. Ruoff, *Nano Lett.* **2009**, 9, 4359; b) L. B. Gao, G. X. Ni, Y. P. Liu, B. Liu, A. H. C. Neto, K. P. Loh, *Nature* **2014**, 505, 190; c) Y. D. Su, H. L. Han, Q. Cai, Q. Wu, M. X. Xie, D. Y. Chen, B. S. Geng, Y. B. Zhang, F. Wang, Y. R. Shen, C. S. Tian, *Nano Lett.* **2015**, 15, 6501.
- [105] a) W. H. Lin, T. H. Chen, J. K. Chang, J. I. Taur, Y. Y. Lo, W. L. Lee, C. S. Chang, W. B. Su, C. I. Wu, *ACS Nano* **2014**, 8, 1784; b) I. Pasternak, A. Krajewska, K. Grodecki, I. Jozwik-Biala, K. Sobczak, W. Strupinski, *AIP Adv.* **2014**, 4, 097133; c) G. Zhang, A. G. Güell, P. M. Kirkman, R. A. Lazenby, T. S. Miller, P. R. Unwin, *ACS Appl. Mater. Interfaces* **2016**, 8, 8008.

Chapter 2

Quantum and electrochemical interplay in hydrogenated graphene

The design of electrochemically gated graphene field-effect transistors for detecting charged species in real time, greatly depends on our ability to understand and maintain a low level of electrochemical current. Here, the interplay between the electrical in-plane transport and the electrochemical activity of graphene is explored. The addition of one H- sp^3 defect per hundred thousand carbon atoms reduces the electron transfer rate of the graphene basal plane by more than five times while preserving its excellent carrier mobility. Remarkably, the quantum capacitance provides insight into the changes of the electronic structure of graphene upon hydrogenation, which predicts well the suppression of the electrochemical activity based on the non-adiabatic theory of electron transfer. Thus, our work unravels the interplay between the quantum transport and electrochemical kinetics of graphene and suggests hydrogenated graphene as a potent material for sensing applications with performances going beyond previously reported graphene transistor-based sensors.

2.1 Introduction

Graphene is unique among other solid-state materials in that all carbon atoms are located on the surface, making the graphene surface highly sensitive for the detection of changes in the environment. Particularly, the concept of electrochemically gated graphene field-effect transistor (GFET) enables the label-free detection of charged molecules on a small footprint upon their bindings at/near the graphene surface:^[1] a binding event modulates the electrical current in the graphene channel through the local variation of the electric field^[2]. The creation of practical electrochemically gated GFETs for detecting charged species, however, greatly depends on our ability to understand and maintain a low level of electrochemical current. Specifically, the electrochemical current rests on the current flowing between the graphene channel and redox active molecules in the solution phase.

Complementary to the GFET sensors, the electrochemical current towards a redox probe in solution has been widely studied and is at the basis of graphene electrochemical (GEC) sensors. Previous studies have revealed that the electrochemical activity is largely sensitive to the intrinsic chemical structure of the graphene basal plane.^[3] Among the multiple approaches used to chemically modify graphene, for example, post-growth chemical modifications using various oxidative reactions^[4] are effective routes to incorporate oxygen atoms, although at the cost of a poor control over the chemical structure of the resulting functional groups (i.e., epoxy, carbonyl, carboxylic acid, alcohol, all at the same time). Particularly, hydrogenated or fluorinated graphene endows a large range of possibilities to progressively tweak graphene with sp^3 defects without significantly pinning the lattice integrity or breaking the resilient basal plane C-C bonds.^[5]

Here, a low density of H- sp^3 defects are introduced into monolayer graphene using a hydrogen plasma. Only one second of plasma treatment is able to render a pristine graphene surface (with few H- sp^3 defects) from the as-grown graphene (referred as untreated graphene) by removing the adsorbed hydrocarbons at the surface, as manifested by the dramatic boost in the electron transfer rate. Importantly, further addition of only one H- sp^3 defect per hundred thousand carbon atoms (more than 1 s of hydrogen plasma), allows us to substantially reduce the electron transfer rate of hydrogenated graphene (H-graphene) compared to untreated graphene. Remarkably, the degradation of the electrochemical kinetics of the graphene basal plane was successfully correlated with the density of states (DOS) by tuning the density of H- sp^3 defects. Although the H- sp^3 termination could contribute to a higher electrochemical activity, the electronic structure (DOS) in graphene plays an even more decisive role

in the rate of electron transfer between graphene and redox probes for a low defect density, indicating a non-adiabatic transfer process on the graphene basal plane.

2.2 Results

2.2.1 Raman characterization

To determine the density and the nature of the defects induced by hydrogen radicals, Raman spectroscopy (Figure 2.1a) and mapping (Figure AI. 1a) characterization was conducted on graphene prepared by chemical vapor deposition (CVD). The similarities between the Raman spectra for both CVD and exfoliated graphene (Figure AI. 2) indicate that the defects induced by the H₂ plasma – particularly the defect density n_D – are respectively equivalent. Importantly, the D peak at $\sim 1340\text{ cm}^{-1}$, due to single phonon intervalley scattering events, is caused by the apparition of H- sp^3 defects.^[6] After a hydrogenation time of 10 s, a D' peak at 1620 cm^{-1} appears in the Raman spectrum as a shoulder of the G peak. The D' peak also associates with H- sp^3 defects.^[7] The values determined for $I(D)/I(D')$ (~ 10) after 30 s and 60 s of hydrogenation are consistent with previous report and confirm the sp^3 nature of hydrogenated defects (Figure 2.1b).^[8] Meanwhile, the intensity ratio $I(2D)/I(G)$, a sensitive parameter to graphene doping, decreases continuously from 2.2 to 1.3 upon extended hydrogenation (see Figure 2.1b).^[9]

Derived from the $I(D)/I(G)$ ratio (a quantitative indicator of point defects in graphene samples),^[10] the defect density n_D increases linearly with hydrogenation time from $n_D = (0.2 \pm 0.3) \times 10^{10}\text{ cm}^{-2}$ at 0 s (untreated graphene) to $n_D = (3.2 \pm 0.7) \times 10^{11}\text{ cm}^{-2}$ at 60 s, corresponding to a decrease in average distance between defects sites (L_D) from 122.6 nm to 10.0 nm (Figure 2.1c, see Appendix I. 2 for the calculation of n_D and L_D). Notably, the Raman mapping (D peak intensity) in Figure AI. 1b on exfoliated graphene flakes (which contains minimal native defects, except for edges), confirms the uniform defect distribution upon hydrogenation. Other surface characterizations including scanning electron microscopy (SEM) and atomic force microscopy (AFM) (Figure AI. 3) further revealed the non-cracked and preserved lattice of H-graphene. Moreover, the low defect densities are also in agreement with the relatively small variations observed for the full width at half maximum (FWHM) of the D and G peaks ($2\text{-}5\text{ cm}^{-1}$, Figure 2.1e).^[22] In addition, the peak broadening as hydrogenation proceeds is mainly due to the shortened lifetime of phonons caused by increasing amounts of defects.^[10-11]

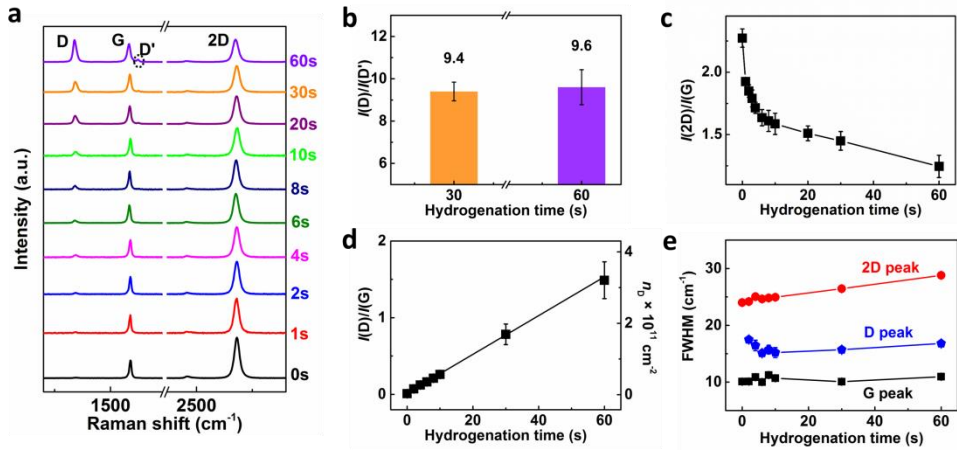


Figure 2.1 Raman characterization of hydrogenated graphene. a) Averaged Raman spectra of CVD graphene on a Si/SiO₂ substrate after 0-60 s of H₂ plasma (10 W, 1.0 mbar). b) The intensity ratio $I(D)/I(D')$ after 30 s and 60 s of hydrogenation. c) The intensity ratio $I(2D)/I(G)$ for hydrogenation times ranging from 0 to 60 s. d) The intensity ratio $I(D)/I(G)$ and the derived defect density n_D , plotted vs the hydrogenation time. The error bars include results from both exfoliated and CVD graphene. e) The FWHM of the 2D, G, and D peaks vs the hydrogenation time. The spectra are recorded using a 2.33 eV (532 nm) laser excitation. The error bars in (b–e) are the standard deviation of experimental values.

2.2.2 Electron transport measurement

High-quality, large-area CVD graphene was used for the device fabrication following a facile and clean fabrication strategy as illustrated in Figure 2.2a (see also Methods for details).^[12] Specifically, the topside of CVD graphene (at Cu foil) was first glued on the supporting glass substrate and protected by the photopolymer of pentaerythritol tetra(3-mercaptopropionate) and triallyl-1,3,5-triazine-2,4,6-trione (PETMP-TATATO).^[13] After the removal of backside graphene (by oxygen plasma), the copper ends were protected by covering them with a film of cellulose acetate butyrate (CAB). Then the graphene surface was exposed by etching the Cu in a solution of ammonium persulfate, followed by a series of hydrogen plasma treatments to introduce defects with controlled densities. During the procedure, a low-temperature annealing process (110°C for ~1-3 h) was employed to ensure a good adhesion of graphene on the underlying polymer substrate. Only the fabricated graphene devices exhibiting mobilities on the order of 1000 – 1500 cm² V⁻¹ s⁻¹ went through a series of field-effect, quantum capacitance, and cyclic voltammetry (CV) experiments immediately after each hydrogenation treatment. To rule out any possible sample-to-sample variations, all the aforementioned measurements were conducted on the same graphene samples.

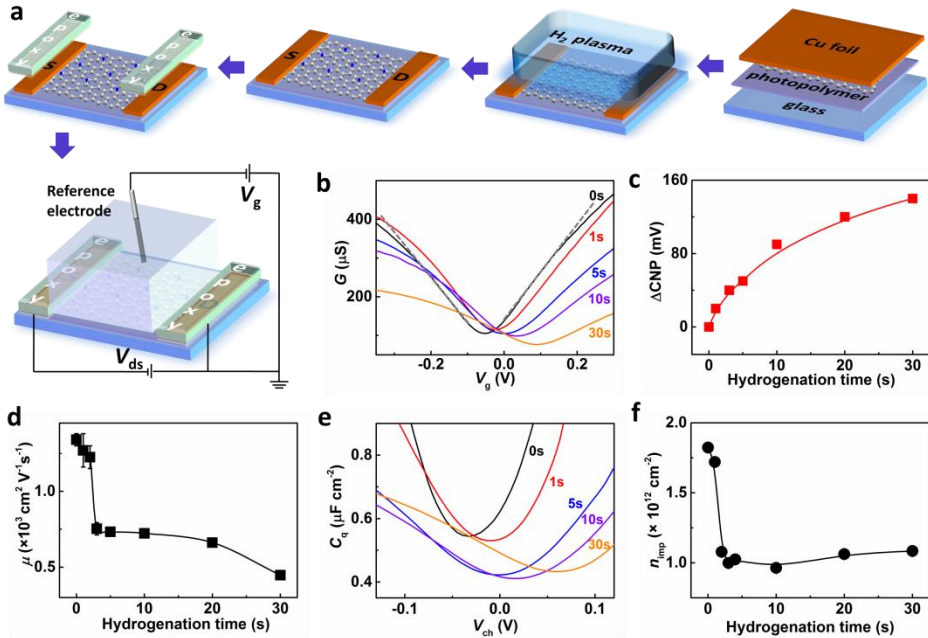


Figure 2.2 Transport characteristic and quantum capacitance of CVD graphene upon hydrogenation. a) Illustration of the field effect transistor setup fabricated from CVD graphene. b) Room temperature conductance (G) plots as a function of the gate voltage (V_g) showing the p-doping effect upon hydrogenation from 0 to 30 s. The gray dashed line is a guide-to-the-eye, highlighting the sublinear behavior of the $G(V_g)$ curves. c) The shifts of the charge neutrality point (CNP) upon hydrogenation. d) The carrier mobility of graphene, μ , vs the hydrogenation time. e) Quantum capacitance C_q of graphene measured as a function of V_{ch} for 0–30 s of hydrogenation. f) Impurity density n_{imp} vs hydrogenation time. The electrolyte solution is 0.1 M KCl with 10 mM Tris (pH 8). The error bars in (d, f) are the standard deviation of experimental values.

Figure 2.2a depicts a GFET device with a source (S) and a drain (D) electrode bridged via a conductive graphene channel. A gate voltage (V_g) is applied to the electrolyte solution via a Ag/AgCl reference electrode, to modulate the conductivity (G) of the GFET. Specifically, when the V_g is swept from negative to positive, the Fermi level (E_F) of graphene shifts from the valence band (hole carriers) to the conduction band (electron carriers). At the so-called charge neutrality point (CNP), the concentration of hole carriers equals that of electron carriers and the conductivity of graphene reaches its minimum G_{min} (Figure 2.2b). The slopes of the sublinear $G(V_g)$ curves are the measure for the carrier mobility μ , while the observed negative voltage of the CNP for

untreated graphene implies an electron (n) doping induced by the underlying photopolymer substrate.

As hydrogenation proceeds, the CNP continuously shifts to more positive voltages, a characteristics of hole (p) doping. This doping effect can be attributed to water adsorption, which occurs more readily on H-graphene than on untreated graphene.^[5b, 14] Upon 1 s hydrogenation, graphene exhibits a slightly increased G_{\min} (Figure 2.2b) and a rather stable carrier mobility μ (Figure 2.2d), suggesting that the mild hydrogenation treatment barely influence – even improves – the electrical properties of graphene.³⁶ As a result, the H radicals after only one second of hydrogenation are hypothesized to yield a cleaner graphene by effectively removing hydrocarbon adsorbates on the surface.³⁷ Further hydrogenation reduces the mobility μ (and G_{\min}) of graphene down to $\sim 750 \text{ cm}^2 \text{ V}^{-1} \text{ s}^{-1}$ (after 2 to 5 s of hydrogenation), after which μ stabilizes at $450\text{-}660 \text{ cm}^2 \text{ V}^{-1} \text{ s}^{-1}$ (after 5 to 30 s of hydrogenation). As a result, the carrier mobility in graphene is mostly sensitive to the introduction of one H- sp^3 scattering centre per $\sim 250,000$ down to $\sim 145,000$ sp^2 hybridized carbon atoms (correspondingly $L_D = 45$ down to 35 nm). In addition to the sublinear behavior of the $G(V_g)$ curves (even after a series of hydrogenation), the remarkable decrease of G_{\min} also suggests that the conductivity of (hydrogenated) graphene is dominated by the short-range scattering mechanism.^[15] Such an observation is also confirmed by previous work in which hydrogenation introduced short-range scatterings in graphene lattice.^[16]

2.2.3 Quantum capacitance measurement

As a direct manifestation of the Pauli exclusion principle, the quantum capacitance effect in graphene is particularly prominent due to its low density of states (DOS).^[17] The quantum capacitance C_q of graphene, can be directly determined as a function of the channel potential across the graphene sheet V_{ch} using an electrochemical configuration (see Figure AI. 4).^[18] In Figure 2.2e, the measured C_q generally displays a broad minimum, $C_{q,\min}$, at the voltage of CNP and linearly increases with V_{ch} on both sides of the CNP. Similar to the conductivity changes after hydrogenation (Figure 2.2b), the V-shaped $C_q(V_{\text{ch}})$ curves exhibit not only positive CNP shifts, but also broader and decreased minimums, as well as more creeping increases of C_q with the voltage. In nature $C_{q,\min}$ is directly related to the density of effective charged impurities, n^* (since these impurities can cause local potential fluctuations in graphene), which can reveal the global behavior of defects in graphene (see Appendix I. 3).^[9a] Notably, our reported capacitance values are generally lower than those reported in previous studies. The difference is ascribed to the cleanness of our

graphene surface, which gives a $n^* = 9.73 \times 10^{10} \text{ cm}^{-2}$, ~ 8 time lower than, for example, CVD graphene on SiO_2/Si wafer ($n^* = 8.0 \times 10^{11} \text{ cm}^{-2}$).^[18] Such a remarkably lowered n^* can be ascribed to our clean fabrication strategy (see Methods) which introduces less charged impurities, or reflects the differences between the substrates, which could lead to different degrees of charge transfer.

More importantly, the effective charged concentration n^* can be related to the impurity density n_{imp} , referred as the impurities at the interfaces between graphene and the substrate, or between graphene and air, or resulting from the intrinsic defects caused by the growth or transfer process of CVD graphene (see Appendix I. 3 for details). In Figure 2.2f, n_{imp} decreases in the first 5 s and then settles till 30 s hydrogenation, a scenario suggesting that the mild hydrogenation (within 1-5 s) sweeps away the trapped/adsorbed charge impurities at graphene interfaces. The evolution of the defect density n_D and of the impurity density n_{imp} are closely related and critical to the electron transport and electrochemical kinetics, which will be discussed in more detail below (see Correlation of n_D with n_{imp}).

2.2.4 Electrochemical kinetics measurement

Cyclic voltammetry (CV) was employed to investigate the electrochemical behavior of H-graphene. Specifically, the hexaammineruthenium (II)/hexaammineruthenium (III) redox couple, $\text{Ru}(\text{NH}_3)_6^{2+/3+}$, was adopted as an outer-sphere redox mediator: i) it is surface insensitive and thus the electron transfer from the mediator to graphene (vice versa) mainly relies on the electronic structures of electrode and the mediator itself, and ii) it possesses a standard potential in the vicinity of the Fermi level of graphene.^[19]

From the CVs in Figure 2.3a, the electrochemical activity of graphene towards the redox probe before and after 1-30 s of hydrogenation was determined. The current densities (j) of the oxidation peak (at -170 mV) and reduction peak (at -290 mV) show that 1 s of hydrogenation is sufficient to increase the electrochemical activity of graphene by a factor of 4 compared to untreated graphene, while further hydrogenation brings about an immediate decrease of activity. The peak-to-peak separation (ΔE_p), a qualitative indicator of the electrochemical reversibility in graphene, displays a minimum at 1 s hydrogenation time in accordance with the current density (Figure A1. 5c).

Furthermore, from the data in Figure 2.3b the heterogeneous electron transfer rate (k^0) between the graphene basal plane and the redox probe was extracted to quantitatively evaluate the electrochemical kinetics of graphene upon hydrogenation.

Specifically, ΔE_p of the quasi-reversible redox peaks are below 220 mV as the scan rate (ν) increases, which meets the criteria of the Nicholson's method to estimate the kinetic parameters^[19-20] (See Appendix I. 4). Consistent with the current density depicted in Figure 2.3a, the deduced values of k^0 exhibit a peaked behavior as a function of the hydrogenation time (Figure 2.3c). In details, k^0 increases by up to ~ 12 fold ($6.77 \times 10^{-4} \text{ cm s}^{-1}$) after one second of hydrogenation compared to untreated graphene ($5.37 \times 10^{-4} \text{ cm s}^{-1}$). For longer hydrogenation times, k^0 sharply drops down to $\sim 1.70 \times 10^{-4} \text{ cm s}^{-1}$ within 5 s and stabilizes at $1.50 \times 10^{-4} \text{ cm s}^{-1}$ after 30 s hydrogenation. Such a trend is reproducible for different batches (see Figure AI. 5a-b and Appendix I. 5).

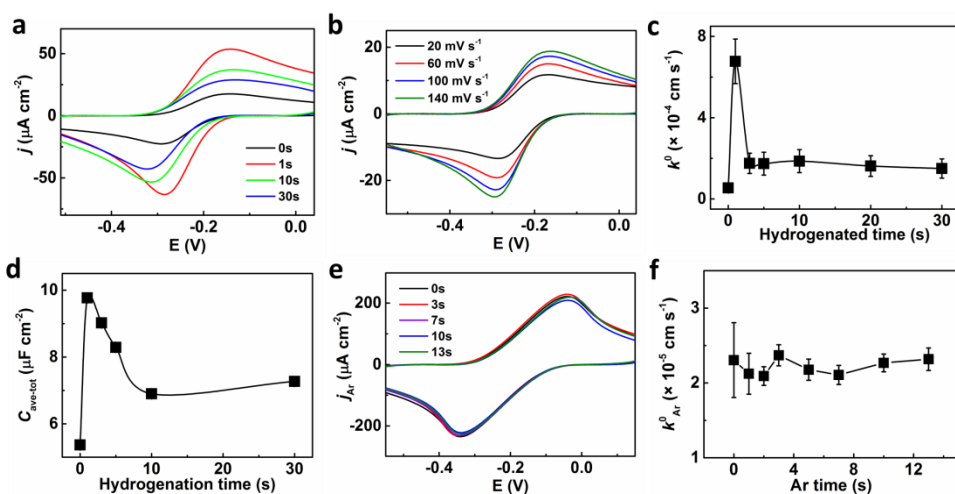


Figure 2.3 Electrochemical behavior of CVD graphene upon hydrogenation. a) Cyclic voltammograms (CVs) obtained on graphene after 0–30 s of hydrogenation at a scan rate of 100 mV s^{-1} . b) Current density vs scan rate for untreated graphene shown in a. c) The electron transfer rate k^0 vs hydrogenation time from 0 to 30 s. d) The averaged total capacitance $C_{\text{ave-tot}}$ vs hydrogenation time from 0 to 30 s. e) CV curves obtained on graphene after 0–13 s of Ar treatment at a scan rate of 100 mV s^{-1} . f) k_{Ar}^0 vs argon plasma treating time from 0 to 13 s. The aqueous electrolyte solution contains 0.1 M KCl supplemented with 10 mM Tris at pH 8. The redox probe employed is 1 mM hexaammineruthenium (II)/hexaammineruthenium (III) chloride. The error bars in (c, d, f) are the standard deviation of experimental values.

The total electrical capacitance (C_{tot}) per unit area of graphene, consists of the electrical double layer capacitance (C_{dl}) and the graphene quantum capacitance (C_{q}) connected in series^[21]. C_{tot} can be obtained either by using a lock-in technique (see Methods) or by measuring the capacitive CV current for different scan rates, which is an averaged evaluation over a relatively wide potential ($C_{\text{ave-tot}}$, Figure AI. 6 and Appendix I. 6). Additionally, the basic rectangular shapes of the capacitive current curves imply purely capacitive behavior without Faradaic processes. Furthermore,

upon hydrogenation $C_{\text{ave-tot}}$ first increases after 1 s, then drops till 10 s and saturate till 30 s, varying similarly as k° (Figure 2.3d). The observed changes in $C_{\text{ave-tot}}$ can be mainly attributed to the DOS variations with hydrogenation (as C_q dominates in the series circuit).

2.2.5 Electrochemistry of H- sp^3 vs vacancy defects

To further evaluate the exact impact of defects on the electrochemical kinetics of graphene, samples that were treated with an argon plasma (referred as Ar-graphene) was studied with comparable defect densities as to hydrogenated graphene (Figure AI. 7 and Appendix I. 7). In contrast to the sensitive electrochemical behavior in H-graphene (Figure 2.3a, c), both the current density and k° on Ar-graphene show negligible sensitivity to the argon plasma treatment (Figure 2.3e, f). Such trends are consistent with the previous report that a low density of vacancy defects hardly impacts the electrochemical activity of graphene^[22].

Based on the different $I(D)/I(D')$ ratios characterized using Raman spectroscopy (i.e., ~ 7 for Ar-graphene and ~ 10 for H-graphene),^[23] argon plasma is identified to forms vacancy defects by removing carbon atoms, while hydrogenation changes graphene hybridization from sp^2 to sp^3 . Thus, the insight is gained into the driving mechanism for the observed electrochemical behavior. Rather than the vacancy defect, the change of hybridization (in H-graphene) is closely related to the electrochemical properties of hydrogenated graphene (Figure 2.3). Meanwhile, coincident to the boost of k° , the G_{min} and μ increase slightly after 1 s of hydrogenation (Figure 2.2), indicating a cleaner graphene with less surface scattering centers: hydrogen radicals are expected to react with the hydrocarbons adsorbed on the surface of graphene. Such a cleaning effect is due to the much higher reactivity of hydrocarbons with hydrogen radicals compared to the reactivity of the graphene itself with the same radicals. As airborne contaminations, hydrocarbons can adsorb onto any surface, as revealed from the observation that the wetting of graphitic surface dramatically changes over short time periods^[24]. Indeed, such cleaning effect is in agreement with prior observations that graphite – more specifically freshly exfoliated highly oriented pyrolytic graphite – exhibits high but instantly decaying electrochemical activity due to the exposure to airborne contaminants.^[25] Notably, no cleaning effect using argon plasma under our condition is expected (ion energy ~ 60 eV)^[26], as also confirmed by the high-resolution transmission electron microscopy images of Ar-graphene (not shown here).

In addition, X-ray photoelectron spectroscopy (XPS, Figure AI. 8 and Appendix I. 8) in complementary to Raman was employed to compare graphene containing similar

defect densities (according to Raman analysis) after 60 s of hydrogenation and after 15 s of argon plasma treatment. The presence of C- sp^2 (284 eV), C- sp^3 (285 eV), C-O (286 – 286.2 eV), and C = O (287.8 – 288 eV) in C 1s spectra, suggest that both samples contain sp^2 and sp^3 carbon with minor oxygen contaminants from PMMA residues (only used for XPS samples to transfer graphene onto the Si substrate). As XPS probes both the surface chemistry of graphene and its surface adsorbents, a higher content of sp^3 carbon was observed from XPS analysis (Table AI. 1), compared to the results of Raman spectroscopy. Thus, the observed sp^3 C in both H-graphene (6.2–8.0%) and Ar-graphene (3%) is ascribed to possible surface adsorbents including PMMA residues and hydrocarbons. A trace amount of sp^3 doping in the graphene lattice (up to 0.8% sp^3 C in H-graphene) was, however, determined by Raman spectroscopy.

2.2.6 Correlation of n_D with n_{imp}

To shed light on the influence of the electrochemical current on the performance of GFET sensors, the interplay between the in-plane charge transport and the electrochemical activity of H-graphene is discussed here. Particularly, the correlations between the DOS, the mobility of charge carriers μ , and the electron transfer rate k^0 , with respect to the density of charged impurity n_{imp} and defect density n_D are systematically investigated. Finally, a comprehensive discussion on the driving mechanism for the electrical and electrochemical behavior observed for H-graphene is provided.

To understand the correlation between defect density n_D and impurity density n_{imp} (presented in Figure 2.4a), it is important to consider their relation to the electronic properties of graphene. It is well-known from studies on supported graphene that defects yield short-range electron scattering in graphene. Impurities, on the other hand, cause long-range (Coulomb) scattering resulting in trapped electron states. The overall conductivity of graphene is dictated by the prevalence of either impurities or defects in the sample; n_D dominates at high charge carrier density while n_{imp} leads at low density regime.^[15b, 27] Impurities are generally present on the graphene-air surface or at the interface between graphene and the underlying substrate. The cleaning effect in the first second of hydrogenation appears in Figure 2.4a as the decreasing onset for n_{imp} (from 9.05 to $8.52 \times 10^{12} \text{ cm}^{-2}$).

Aside from the cleaning effect, the subsequent drop in n_{imp} from $8.52 \times 10^{12} \text{ cm}^{-2}$ to $5.01 \times 10^{12} \text{ cm}^{-2}$ occurs as hydrogenation induces changes in hybridization from sp^2 to sp^3 , steadily increasing n_D . The presence of sp^3 hybridized spots in the lattice causes the lattice to expand and to curve. The increased distance between the lattice

and substrate-related impurities explains the sharp drop in n_{imp} . Further on, n_{imp} slightly increases (from $5.01 \times 10^{12} \text{ cm}^{-2}$ to $5.31 \times 10^{12} \text{ cm}^{-2}$), which can be ascribed to the accumulation of trapped water molecules at the graphene surface, accompanying the increasing n_{D} ($n_{\text{D}} > (2.6 \pm 0.5) \times 10^{10} \text{ cm}^{-2}$).

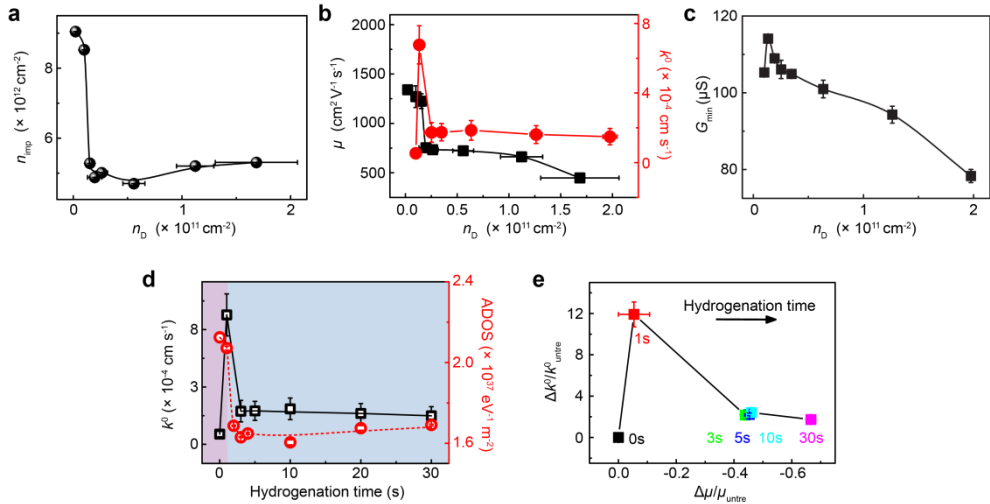


Figure 2.4 Quantum and electrochemical interplays in hydrogenated graphene. a) The dependence of n_{imp} on n_{D} . b) Correlations of μ and k^0 with n_{D} , respectively. c) The minimum conductivity (G_{min}) vs n_{D} . d) The correspondence between ADOS and k^0 as a function of the hydrogenation time. The purple region represents the cleaning-dominated regime and the blue region represents the regime where the chemical modification dominates. e) The relative variations of $\Delta \mu/\mu_{\text{untre}}$ correlating with $\Delta k^0/k_{\text{untre}}^0$ according to the corresponding hydrogenation time. The subscript "untre" represents the untreated graphene. The error bars are the standard deviation of experimental values.

2.2.7 Correlation of k^0 and μ with n_{D}

The first report on the correlation of k^0 with the density of vacancy defects in monolayer graphene showed that k^0 remained constant at low densities but underwent a tenfold increase at a defect density of 10^{12} cm^{-2} ($I_{\text{D}}/I_{\text{G}} \cong 2.95$).^[22] However, the high density of vacancy defects lowers the electrical performance of graphene. In our work, k^0 is improved up to 12-fold (to $6.77 \times 10^{-4} \text{ cm}^2 \text{ s}^{-1}$) at a low H- sp^3 defect density of $n_{\text{D}} = (1.0 \pm 0.1) \times 10^{10} \text{ cm}^{-2}$ ($I_{\text{D}}/I_{\text{G}} \cong 0.4$). Then, when n_{D} continues to rise, k^0 drops sharply to stabilize between $1.5 - 1.7 \times 10^{-4} \text{ cm}^2 \text{ s}^{-1}$ (red line, Figure 2.4b).

Separately, when k^0 increases, the carrier mobility μ stays unchanged (or becomes slightly higher) compared to untreated graphene (black line, Figure 2.4b) at $n_{\text{D}} =$

$(1.0 \pm 0.1) \times 10^{10} \text{ cm}^{-2}$. With the continuous growth of defect density up to $n_D = (2.0 \pm 0.7) \times 10^{10} \text{ cm}^{-2}$, μ exhibits a deep drop, indicating that the carrier transport in graphene is sensitive to the existence of even low densities of H- sp^3 defects ($n_D \leq 2.0 \times 10^{10} \text{ cm}^{-2}$ corresponds to inter-distance L_D of $\sim 40 \text{ nm}$). For higher defect densities, however, the decrease of μ is less pronounced (till $n_D = (1.7 \pm 0.4) \times 10^{11} \text{ cm}^{-2}$, that is $L_D \sim 14 \text{ nm}$). The minimum conductivity (G_{\min}) changes with n_D in Figure 2.4c, correlating well with the fluctuations in mobility (Figure 2.4b).

Based on Boltzmann theory, the conductivity of graphene (G) is proportional to $1/\sqrt{n_D}$ at high carrier density (far from the CNP).^[28] In consequence, μ is expected to decrease with increasing n_D upon hydrogenation, while at low carrier density (near the CNP), G is proportional to $\sqrt{n_{\text{imp}}}$ and G_{\min} is expected to reduce with the decrease of n_{imp} . The data in Figure 2.4b,c follow to the theory, except for the increase in both G_{\min} and μ at the initial dose of hydrogenation ($n_D = (1.0 \pm 0.1) \times 10^{10} \text{ cm}^{-2}$). This can be explained by considering the cleaning of adsorbates from the graphene surface. To be specific, hydrogenation introduces H- sp^3 defects while also removing surface short-range scatterers outweighing the effect on the conductivity and mobility of graphene. Separately, the decrease of ADOS after hydrogenation contributes to the decrease of intrinsic charge carrier density n rather than affecting the carrier mobility in graphene.

2.2.8 Correlation between the DOS and k^0

In electrochemistry, the kinetics of electron transfer from graphene to a redox probe is dependent on the electrochemical potential of electrons in graphene (that is the Fermi level, E_F) with respect to the electrochemical potential of the redox couple in solution.^[17, 29] For example, for the electron to flow from the graphene to the redox probe, the graphene E_F that can be tuned by varying the potential applied to the graphene electrode or by sweeping the gate voltage, should at least align with the LUMO level of the oxidative molecule to allow an efficient electron transfer. For a non-adiabatic process, the DOS in graphene decides – whether or not – a basal plane electron could tunnel to the redox probe. Practically, the electron transfer occurs when the electronic resonance between the redox molecule and graphene is reached, that is for a given value of the applied potential, and is measured by studying how fast the electron transfer reaction can reach its equilibrium (*kinetics*).^[30] In short, the electrochemical kinetics (reflected by k^0) of graphene relies on the DOS on the premise of non-adiabatic electron transfer.

In 2D materials like graphene, its minimal quantum capacitance, $C_{q,\min}$, can be used to deduce its average DOS (ADOS) at a specific E_F : $\langle \rho \rangle = C_{q,\min}/e^2$, where e is the

electron charge.^[31] The change of ADOS with k^o as hydrogenation proceeds is plotted and compared in Figure 2.4d. During the first second (within the grey region), the ADOS decreases a little, however k^o increases dramatically, which can be mainly ascribed to the volatilization of hydrocarbon contaminants. That is, the hydrogen radicals first remove the hydrocarbon adsorbates to reveal the electrochemical activity of the underlying graphene, as the kinetic process involves interface-sensitive electron tunneling. Notably, H radicals can also attack the graphene lattice during the hydrocarbon cleaning and the resulted H- sp^3 defects could lead to the observed decrease in the ADOS.^[22] Upon further hydrogenation (the beginning of the green region), the ADOS and k^o decrease sharply, which are mainly due to the modification of graphene basal plane by hydrogen radicals. The decay of k^o with DOS is in concordance with the non-adiabatic electron transfer, in which the rate depends on the electronic properties of the electrode due to the weak electronic interaction between the redox mediator and the electrode, according to the Levich–Dogonadze theory^[32] and Fermi’s golden rule^[33]. It is of note here that the decrease in k^o (Figure 2.4d) is unlikely due to H- sp^3 termination, as the formed C-H dipole is more susceptible towards nucleophilic attack,^[34] which could increase the electrochemical activity. Nor is it likely that the kinetics were affected by surface oxidation during exposure to air: XPS spectra on hydrogenated graphene demonstrate stable and negligible presence of hydroxyl/epoxy groups (Figure AI. 8 and Table AI. 1). Additionally, the DOS was predicted to contribute more significantly to the kinetics compared to surface modification. Thus for the first time the electrochemical kinetics in the single layer graphene is demonstrated to be highly sensitive to the ADOS upon the addition of even a single H- sp^3 defect per 100,000 sp^2 carbon atoms. More importantly, the correlation between k^o and DOS in return confirms the importance of graphene electronic properties (DOS) in terms of defining the electrochemical current for sensing application.

2.2.9 Correlation between μ and k^o

Figure 2.4e shows the dependence of the relative variation of $\Delta k^o/k_{\text{untre}}^o$ with $\Delta\mu/\mu_{\text{untre}}$, where $\Delta k^o/k_{\text{untre}}^o = \frac{k^o/k_{\text{untre}}^o - 1}{k_{\text{untre}}^o}$, $\Delta\mu/\mu_{\text{untre}} = \frac{\mu - \mu_{\text{untre}}}{\mu_{\text{untre}}}$, and the subscript “untre” denotes untreated graphene. Notably, the negative values of $\Delta\mu/\mu_{\text{untre}}$ corresponds to the degradation of the carrier mobility upon hydrogenation time (see also Figure 2.2). Specifically, the peak value of the $\Delta k^o/k_{\text{untre}}^o$ after one second of hydrogenation is ascribed to the disclosure of the intrinsic electrochemical activity of the graphene basal plane resulting from the volatilization of hydrocarbon adsorbates. For hydrogenation times longer than 3-5 s, $\Delta k^o/k_{\text{untre}}^o$ decreases by ~ 5 times compared to the peak value (at 1 s) with preserved mobility (~ 50 -60 %). Our results therefore

suggest the importance of H- sp^3 defects towards achieving a low electrochemical activity in GFET by suppressing its DOS. Interestingly, the boosted k^o after surface cleaning reveals a relatively high electrochemical activity of graphene basal plane, which was often believed to be inert and inactive in electrochemistry.^[35]

2.3 Discussions

A hydrogen radical plasma is demonstrated to clean the surface of graphene and chemically modify the graphene lattice upon continuous exposure. For the chemical modification, the hydrogen radical forms a covalent bond with the carbon atom in the graphene lattice, changing its hybridization from sp^2 to sp^3 . In the beginning (the first 1–5 s), the introduced H radicals mainly sweep the hydrocarbon adsorbates away from the graphene surface. In particular, within the first second of hydrogenation a large enhancement of the electrochemical activity on the surface of pristine graphene (with a minimum of H- sp^3 defects) is observed. It is postulated that in untreated graphene, the electrochemical activity was initially blocked by the presence of hydrocarbon adsorbates which are now removed by the hydrogen plasma^[36] (Figure 2.3c and Figure 2.4d). Remarkably, even traces amounts of H- sp^3 defects in graphene (only one sp^3 defect per $\sim 400,000$ carbon atoms) results in the decrease of the DOS, a quantity considerably sensitive to the changes of electronic and chemical properties of graphene. Additionally, further hydrogenation of the graphene basal plane largely depresses k^o down to one fifth of its original value (pristine graphene), presumably by lowering its DOS. Interestingly, however, the mobility of graphene is preserved to a large extent (Figure 2.2), promising future development of electrochemical field-effect transistors based on H-graphene.

Given the relatively depressed mobility for the starting samples, the intrinsic defect (i.e. vacancy, grain boundary) and scatterings from the substrate are assumed to already exist. Therefore, the carrier transport properties is limited by the lowest impedance pathways already existing within the graphene lattice. Anything that affects the number of scatters and their cross section will disproportionately register as a mobility change. In other words, it is only specific defects at certain locations that will have the most influence on the mobility. In addition, the mobility changes with the defect density in Figure 2.2d in an implied and non-linear trend. As the density of hydrogenated defect grows, the interdefect distance between defective sites (randomly and uniformly distributed) decreases. In other words, the defect distribution evolves from random to “cluster”. In consequence, the influence of defect at high density level on the transport properties of graphene becomes less sensitive than the low density level.

Besides hydrogenation, the physisorption of water molecules at the graphene surface reflected by the observed p-doping effect (Figure 2.2b)^[14] is also considered. As non-covalent functionalization, water molecules can barely disturb the intrinsic aromaticity,^[37] and are thus expected to exert little impact on the electronic structure and electrochemistry of graphene^[38]. For example, the resistivity at the CNP as well as the carrier mobility barely changed after removal of the adsorbed water^[14]. Separately, negligible oxidation is found using XPS characterization even in aged graphene, as shown in Figure AI. 5. Therefore the major contributions of surface-adsorbed water and graphene oxidation can be excluded to the observed electrical and electrochemical properties of hydrogenated graphene.

2.4 Conclusions

In summary, we have systematically probed the interplay between the in-plane electron transport and the electrochemical activity of the graphene basal plane by modulating the density of H-*sp*³ defects. Interestingly, the mild hydrogenation within 1–5 s largely preserves the basic electrical mobility while effectively depresses the electrochemical kinetics k° and lowers the DOS in graphene, manifesting as a plausible way to improve the sensitivity of GFET. For the first time, we demonstrated that the electrochemical kinetics in single layer H-graphene is highly dependent on the ADOS, which supports the theory of non-adiabatic electron transfer on graphene. Additionally, the electrochemical activity of the pristine graphene basal plane can be restored by the removal of surface-adsorbed hydrocarbons using a low dose of hydrogen radicals, a result that will further promote graphene as an electrode for electrochemical studies. The correlation between the carrier mobility and the electrochemical kinetics suggests that the electrical conductivity of H-graphene is an important parameter to consider, for example, in GEC sensors. We believe our work will inspire several research communities to consider hydrogenated graphene as a potent material for sensing applications with performances going beyond previously reported (G)FET sensors.

2.5 References

- [1] a) A. Zhang, C. M. Lieber, *Chem. Rev.* **2015**, 116, 215; b) W. Fu, L. Jiang, E. P. van Geest, L. Lima, G. F. Schneider, *Adv. Mater.* **2016**, 6, 1603610.
- [2] a) M. T. Hwang, P. B. Landon, J. Lee, D. Choi, A. H. Mo, G. Glinsky, R. Lal, *Proc. Natl. Acad. Sci.* **2016**, 113, 7088; b) N. Gao, T. Gao, X. Yang, X. Dai, W. Zhou, A. Zhang, C. M. Lieber, *Proc. Natl. Acad. Sci.* **2016**, 113, 14633.

- [3] a) Y. Wang, Y. Shao, D. W. Matson, J. Li, Y. Lin, *ACS nano* **2010**, 4, 1790; b) Z. Xia, F. Leonardi, M. Gobbi, Y. Liu, V. Bellani, A. Liscio, A. Kovtun, R. Li, X. Feng, E. Orgiu, *ACS Nano* **2016**, 10, 7125; c) P. Fortgang, T. Tite, V. Barnier, N. Zehani, C. Maddi, F. Lagarde, A.-S. Loir, N. Jaffrezic-Renault, C. Donnet, F. Garrelie, *ACS Appl. Mater. Interfaces* **2016**, 8, 1424; d) A. Y. S. Eng, Z. Sofer, Š. Huber, D. Bouša, M. Maryško, M. Pumera, *Chem. Eur. J.* **2015**, 21, 16828.
- [4] a) S. Eigler, A. Hirsch, *Angew. Chem. Int. Ed.* **2014**, 53, 7720; b) Z. Bai, L. Zhang, L. Liu, *J. Phys. Chem. C* **2015**, 119, 26793; c) A. Bagri, C. Mattevi, M. Acik, Y. J. Chabal, M. Chhowalla, V. B. Shenoy, *Nat. Chem.* **2010**, 2, 581.
- [5] a) Z. Sun, C. L. Pint, D. C. Marcano, C. Zhang, J. Yao, G. Ruan, Z. Yan, Y. Zhu, R. H. Hauge, J. M. Tour, *Nat. Commun.* **2011**, 2, 559; b) D. C. Elias, R. R. Nair, T. Mohiuddin, S. Morozov, P. Blake, M. Halsall, A. Ferrari, D. Boukhvalov, M. Katsnelson, A. Geim, *Science* **2009**, 323, 610; c) R. R. Nair, W. Ren, R. Jalil, I. Riaz, V. G. Kravets, L. Britnell, P. Blake, F. Schedin, A. S. Mayorov, S. Yuan, *Small* **2010**, 6, 2877; d) J. Son, S. Lee, S. J. Kim, B. C. Park, H.-K. Lee, S. Kim, J. H. Kim, B. H. Hong, J. Hong, *Nat. Commun.* **2016**, 7, 13261.
- [6] F. Tuinstra, J. L. Koenig, *J. Chem. Phys.* **1970**, 53, 1126.
- [7] P. Lespade, A. Marchand, M. Couzi, F. Cruege, *Carbon* **1984**, 22, 375.
- [8] A. Eckmann, A. Felten, A. Mishchenko, L. Britnell, R. Krupke, K. S. Novoselov, C. Casiraghi, *Nano Lett.* **2012**, 12, 3925.
- [9] a) A. Das, S. Pisana, B. Chakraborty, S. Piscanec, S. Saha, U. Waghmare, K. Novoselov, H. Krishnamurthy, A. Geim, A. Ferrari, *Nat. Nanotechnol.* **2008**, 3, 210; b) Q. H. Wang, C.-J. Shih, G. L. Paulus, M. S. Strano, *J. Am. Chem. Soc.* **2013**, 135, 18866.
- [10] L. G. Cançado, A. Jorio, E. M. Ferreira, F. Stavale, C. Achete, R. Capaz, M. Moutinho, A. Lombardo, T. Kulmala, A. Ferrari, *Nano Lett.* **2011**, 11, 3190.
- [11] A. C. Ferrari, D. M. Basko, *Nat. Nanotechnol.* **2013**, 8, 235.
- [12] W. Fu, C. Nef, A. Tarasov, M. Wipf, R. Stoop, O. Knopfmacher, M. Weiss, M. Calame, C. Schönenberger, *Nanoscale* **2013**, 5, 12104.
- [13] N. B. Cramer, C. L. Couch, K. M. Schreck, J. A. Carioscia, J. E. Boulden, J. W. Stansbury, C. N. Bowman, *Dent. Mater.* **2010**, 26, 21.

- [14] B. R. Matis, J. S. Burgess, F. A. Bulat, A. L. Friedman, B. H. Houston, J. W. Baldwin, *ACS Nano* **2012**, 6, 17.
- [15] a) F. Schedin, A. Geim, S. Morozov, E. Hill, P. Blake, M. Katsnelson, K. Novoselov, *Nature materials* **2007**, 6, 652; b) E. Hwang, S. Adam, S. D. Sarma, *Phys. Rev. Lett.* **2007**, 98, 186806; c) M. Trushin, J. Schliemann, *EPL (Europhysics Letters)* **2008**, 83, 17001.
- [16] J. Balakrishnan, G. K. W. Koon, M. Jaiswal, A. C. Neto, B. Özyilmaz, *Nat. Phys.* **2013**, 9, 284.
- [17] I. Heller, J. Kong, K. A. Williams, C. Dekker, S. G. Lemay, *J. Am. Chem. Soc.* **2006**, 128, 7353.
- [18] J. Xia, F. Chen, J. Li, N. Tao, *Nat. Nanotechnol.* **2009**, 4, 505.
- [19] M. Velicky, D. F. Bradley, A. J. Cooper, E. W. Hill, I. A. Kinloch, A. Mishchenko, K. S. Novoselov, H. V. Patten, P. S. Toth, A. T. Valota, *ACS Nano* **2014**, 8, 10089.
- [20] R. S. Nicholson, *Anal. Chem.* **1965**, 37, 1351.
- [21] H. Ji, X. Zhao, Z. Qiao, J. Jung, Y. Zhu, Y. Lu, L. L. Zhang, A. H. MacDonald, R. S. Ruoff, *Nat. Commun.* **2014**, 5, 3317.
- [22] J.-H. Zhong, J. Zhang, X. Jin, J.-Y. Liu, Q. Li, M.-H. Li, W. Cai, D.-Y. Wu, D. Zhan, B. Ren, *J. Am. Chem. Soc.* **2014**, 136, 16609.
- [23] A. Eckmann, A. Felten, I. Verzhbitskiy, R. Davey, C. Casiraghi, *Phys. Rev. B* **2013**, 88, 035426.
- [24] Z. Li, Y. Wang, A. Kozbial, G. Shenoy, F. Zhou, R. McGinley, P. Ireland, B. Morganstein, A. Kunkel, S. P. Surwade, L. Li, H. Liu, *Nat. Mater.* **2013**, 12, 925.
- [25] a) A. N. Patel, M. G. Collignon, M. A. O'Connell, W. O. Y. Hung, K. McKelvey, J. V. Macpherson, P. R. Unwin, *J. Am. Chem. Soc.* **2012**, 134, 20117; b) M. Velický, M. A. Bissett, P. S. Toth, H. V. Patten, S. D. Worrall, A. N. J. Rodgers, E. W. Hill, I. A. Kinloch, K. S. Novoselov, T. Georgiou, L. Britnell, R. A. W. Dryfe, *Phys. Chem. Chem. Phys.* **2015**, 17, 17844.
- [26] Y.-D. Lim, D.-Y. Lee, T.-Z. Shen, C.-H. Ra, J.-Y. Choi, W. J. Yoo, *ACS Nano* **2012**, 6, 4410.

- [27] J.-H. Chen, C. Jang, S. Adam, M. Fuhrer, E. Williams, M. Ishigami, *Nat. Phys.* **2008**, 4, 377.
- [28] S. Adam, E. Hwang, E. Rossi, S. D. Sarma, *Solid State Commun.* **2009**, 149, 1072.
- [29] G. L. Paulus, Q. H. Wang, M. S. Strano, *Acc. Chem. Res.* **2012**, 46, 160.
- [30] D. M. Adams, L. Brus, C. E. Chidsey, S. Creager, C. Creutz, C. R. Kagan, P. V. Kamat, M. Lieberman, S. Lindsay, R. A. Marcus, *J. Phys. Chem. B* **2003**, 107, 6668.
- [31] J. Eisenstein, L. Pfeiffer, K. West, *Phys. Rev. Lett.* **1992**, 68, 674.
- [32] V. Levich, *Physical chemistry, and advanced treatise, vol Xb. Academic, New York* **1970**.
- [33] R. Nissim, C. Batchelor-McAuley, M. C. Henstridge, R. G. Compton, *Chem. Commun.* **2012**, 48, 3294.
- [34] A. M. Debela, M. Ortiz, V. Beni, C. K. O'Sullivan, *Chem. Eur. J.* **2014**, 20, 7646.
- [35] D. A. C. Brownson, D. K. Kampouris, C. E. Banks, *Chem. Soc. Rev.* **2012**, 41, 6944.
- [36] Z. Li, A. Kozbial, N. Nioradze, D. Parobek, G. J. Shenoy, M. Salim, S. Amemiya, L. Li, H. Liu, *ACS Nano* **2016**, 10, 349.
- [37] Z. Zhang, H. Huang, X. Yang, L. Zang, *J. Phys. Chem. Lett.* **2011**, 2, 2897.
- [38] Y. F. Peng, J. Wang, Z. S. Lu, X. Y. Han, *IOP Conf. Ser. Mater. Sci. Eng.* **2015**, 87, 012101.

Chapter 3

Oxygen reduction reaction on nitrogen-doped graphene activated by co-doped oxygen functional groups

Nitrogen-doped carbon materials have gained considerable attention as non-platinum-group catalysts for oxygen reduction reaction (ORR). However, there has been much controversy about the active sites, not only concerning the different nitrogen doping configurations but also the correlation of activity with nitrogen dopants. Here, nitrogen dopants are systematically introduced into a monolayer graphene – a model carbon-based catalyst – to reveal the potential active sites for oxygen reduction catalysis. Upon nitrogenation treatment, pure graphene with minimal surface oxidation shows decreased ORR activity, while a graphene surface containing air-induced oxidation sites enhances the activity. Regardless of the nitrogen dopants, graphene exhibits improved catalytic activity upon oxygen doping. Further correlation of the chemical compositions with the catalytic activity of nitrogenated and oxygenated graphene reveals for the first time that oxygen containing groups, instead of N-doping sites, are at the origin of the enhanced activity of nitrogenated graphene for ORR electrocatalysis.

This chapter is prepared as an article: Lin Jiang, Bas van Dijk, Longfei Wu, Jan P. Hofmann, Viorica Tudor, Marc T. M. Koper, Dennis G. H. Hetterscheid, Grégory F. Schneider, submitted.

3.1 Introduction

Nitrogen-doped (N-doped) carbon-based metal-free materials like graphene and carbon nanotubes have been reported as effective and promising alternatives to platinum catalysts for the oxygen reduction reaction (ORR), a critical reaction for renewable energy technologies including fuel cells.^[1] Both experimental and theoretical efforts have been devoted to determine the active sites of N-doped carbon materials for the ORR.^[2] Particularly, positively charged carbon atoms next to pyridinic nitrogen atoms have been suggested to preferentially adsorb O₂ molecules and thus favor fast ORR kinetics.^[3] However, such a mechanism does not explain the catalytic effect in boron and/or sulphur doped carbon materials.^[4] Moreover, it has been reported that in some cases graphene containing N dopants, such as chemical vapor deposited (CVD) graphene with dominantly pyridinic N dopants, are not active for the ORR.^[2b, 5] In fact, graphene with vacancy defects is in some cases more active than N-doped graphene towards the ORR.^[5b, 6] The controversy about the ORR activity of N-doped graphene can be ascribed to the significant structure and morphology variations in the studied materials, which are mostly based on graphene nanoflakes dispersions.^[7] Typically overlooked issues for these materials are the inhomogeneous and undervalued active sites for ORR catalysis, caused by flake aggregation, irreversible pyrolysis or vigorous chemical treatments. For example, oxygen groups are abundant in graphene nanoflakes due to their high oxygen affinity. In fact, oxygen-containing functionalities in carbon nanotubes and reduced graphene oxide have been reported to directly correlated to the active ORR performance.^[8] In addition, a recent computational paper describing proton-coupled electron transfer on graphene surfaces showed that carbene type active sites are stabilized by a combination of pyridinic nitrogen and quinone type oxygen functionalities.^[9] However, little experimental attention has been given to the role of oxygen functionalities within N-doped graphene in the ORR mechanism.

Therefore, a detailed study disclosing the relationships between ORR activity and the surface chemistry of N-doped carbon materials is desired. For that purpose, a reliable and well-defined system is required. Consequently, monolayer graphene film grown via the chemical vapor deposition (CVD) method were used in this study.^[10] Homogeneous graphitization level and sensitive surface chemistry make the monolayer CVD graphene an ideal model for carbon-based metal-free catalysts.^[11] Specifically, ORR performance of a monolayer graphene upon N- and O-doping was systematically studied. Indeed, this N-doped graphene has a high level of graphitization and conductivity as characterized by Raman spectroscopy and electrical transport measurements. To study the electrochemical performance for ORR catalysis, both an epoxy resin and a rotating glassy carbon disk electrode were

used as the support of the graphene. According to the XPS characterization, it is found that oxygen functional groups (C-O), instead of nitrogen dopants, are the most active sites for oxygen reduction on nitrogenated graphene.

3.2 Results and Discussion

3.2.1 Raman characterization of N-doped graphene

Raman spectroscopy (Figure 3.1a) was conducted to evaluate the N-doping process on chemical vapor deposition (CVD) graphene supported by a SiO₂/Si substrate. For pristine graphene, two main characteristic peaks for monolayer graphene can be found. The G peak ($\sim 1580\text{ cm}^{-1}$) arises from the C-C stretching within all sp^2 carbon systems. The sharp 2D peak ($\sim 2670\text{ cm}^{-1}$) corresponds to the overtone of breathing modes of six-atom rings and is sensitive to the number of graphene layers and doping effect.^[12] After more than 2 s of nitrogenation, a D peak appears at $\sim 1340\text{ cm}^{-1}$ that corresponds to single phonon intervalley scattering events and is associated with the incorporation of nitrogen atoms into the lattice of graphene as defect sites.^[13] Upon longer nitrogenation times ($> 6\text{ s}$), a D' peak at 1620 cm^{-1} emerges as a shoulder of the G peak due to the intervalley scattering induced by nitrogen defects.^[14] When the nitrogenation time increases from 0 to 60 s, the intensity ratio $I(2D)/I(G)$ decreases from 2.0 to 0.7 (Figure 3.1b) and the 2D peak shifts from 2674 to 2665 cm^{-1} (Figure 3.1c), both suggesting an electron (n-) doping effect in nitrogenated graphene.^[15] The full width at half maxima (FWHMs) for the D, G and 2D peaks (Figure 3.1d) slightly increase upon increasing the nitrogenation time from 0 to 30 s and saturate at 60 s. The increase of the FWHMs indicates a growth of defect density. As a quantitative reflection of the defect density (n_D) and interdefect distance (L_D),^[16] the ratio of $I(D)/I(G)$ in Figure 3.1d (black line) exhibits a similar growth trend with the peak widths (see n_D and L_D in Table AII. 1). Such consistent saturation trends may correspond to the clustering of nitrogen defects at high doping level.^[5a, 17] This is reflected by a domain-like defect distribution in graphene after 30 s of nitrogenation (Figure AII. 1). Specifically, the increasing trends for both the $I(D)/I(G)$ ratio and the FWHM of the G peak confirm the dominance of sp^2 -hybridized carbon network over the introduced defects, thus it is concluded that the N-doped graphene still has a high lattice integrity. It is reported that a ratio of circa 3 for $I(D)/I(D')$ represents boundary defects while a ratio of circa 7 indicates vacancy defects as based on a model of uniform defect distribution without clustering.^[18] In our case, the $I(D)/I(D')$ ratios vary from 6.5 (10-20 s of nitrogenation) to 5 (more than 30 s of nitrogenation) (Figure 3.1d, blue dots) indicating that nitrogen dopants behave more like vacancy defects. To conclude, Raman spectroscopy shows that N-doped graphene has a high, uniform graphitization level and vacancy-like defects.

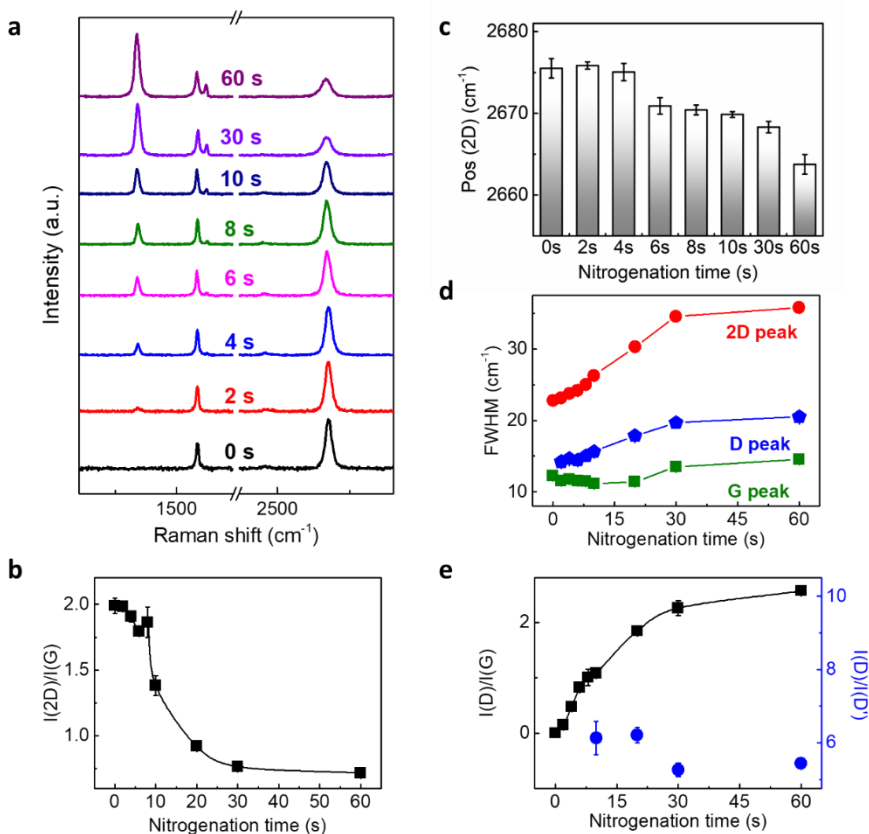


Figure 3.1 Raman spectroscopy of N-doped graphene. a) Raman spectra of exfoliated graphene after 0–60 s of nitrogenation. The spectra are recorded using 2.33 eV (532 nm) laser excitation. b) Intensity ratio $I(2D)/I(G)$ as a function of nitrogenation times. c) Red-shift of 2D peak position vs nitrogenation times. d) Variations of full width at half maxima (FWHMs) for D, G and 2D peaks upon 0 to 60 s nitrogenation. e) Evolution of intensity ratio $I(D)/I(G)$ (black) and $I(D)/I(D')$ (blue) with respect to the nitrogenation time.

3.2.2 Structure characterization of N-doped graphene

X-ray photoelectron spectroscopy (XPS) characterization was further performed to analyze the chemical structure of nitrogenated graphene. XPS survey spectra for pristine and 60 s N-doped graphene are displayed in Figure AII. 2a–b, with O1s peaks mainly originating from the underlying copper substrate. Figure 3.2 shows the high resolution XPS C1s (a) and N1s (b) spectra for pristine, 30 s and 60 s of N-doped graphene. The C1s spectra can be deconvoluted into five peaks: sp^2 C–C (284.4 eV), sp^3 C–C (285.0 eV), C–O/C=N (286.4 eV), C=O/C–N (288.0 eV), and O–C=O (289.0 eV), respectively.^[19] The oxygen-containing groups in C1s indicate oxidation in pristine graphene induced by air exposure (even for a short period). A higher content of

oxygen in aged graphene samples (Figure AII. 2c) confirms the unavoidable oxidation during handling. As a result, to obtain reliable comparisons of the chemical structure, fresh graphene samples with similar aging degrees (i.e. within one week after the CVD growth) were used for different doping treatments. Upon nitrogenation, the O:C ratio evolves from 2.3% for pristine, to 4.2% and 10.2% for 30 s and 60 s N-doped graphene, respectively. Nitrogenation treatments create high reactive sites for oxygen uptake, which explains the increased oxidation degree of N-doped graphene.^[20] Specifically, vacancy defects that are created during the more clustered N-doping process (30 to 60 s nitrogenation times) are mainly responsible for the increased oxidation. The N 1s spectra for 30 s N-doped samples consist of two main peaks centered at 398.9 eV and 399.9 eV, corresponding to pyridinic (pyrid-) and pyrrolic (pyrro-) N.^[5b, 19a] For 60 s N-doped graphene, in addition to the pyrid- and pyrro-N peaks, another peak at 401.1 eV is observed and assigned to quaternary (quat-) N. Moreover, the dominant forms of pyrid- and pyrro-N agree well with the observed n-type doping effect in Figure 3.1 (see Figure AII. 1).

3.2.3 Electrical transport characteristics of N-doped graphene

Next, the electron transport characteristics of graphene was studied in the configuration of an electrochemically-gated graphene field effect transistor (GFET) that was fabricated following a previously reported facile strategy (see Methods).^[21] An epoxy substrate was used to support a clean, pristine graphene surface that was protected by a clean and annealed copper substrate. Moreover, this graphene surface was never in contact with and thus contaminated by any polymer that is generally used for graphene transfer,^[22] and was only exposed to the ambient oxygen in a short period before measurements. The surface purity is better than that of graphene transferred by the polymer assisted method as the graphene contains a lower density of charged impurities (i.e. originating from ambient oxidation or trapped impurities).^[21] The conductance (G) of this clean graphene demonstrates an ambipolar behavior with respect to the gate voltage (V_g) as shown in Figure 3.2c (black line) (see discussion in Appendix II. 3). The $G(V_g)$ curves start to shift negatively after 10 s of nitrogenation and the charge neutrality point (CNP) shifts by -30 to -60 mV between 20 to 60 s of nitrogenation. This shift suggests an n-doping effect in graphene (Figure 3.2d). Using the capacitor model in the electrochemical-gating configuration^[23], it is found that the carrier mobility (μ) of pristine graphene decreases from $\sim 3800 \text{ cm}^2 \text{ V}^{-1} \text{ s}^{-1}$ to $\sim 550 \text{ cm}^2 \text{ V}^{-1} \text{ s}^{-1}$ after 30 s of nitrogenation and subsequently levels off at 60 s of nitrogenation (Figure 3.2d, black). Notably, the high carrier mobility value for pristine graphene confirms its intrinsic high-quality and surface purity. Corresponding to the similar saturation trend of $I(D)/I(G)$ ratios in Figure 3.1d, graphene carrier mobility is predicted to be closely related to the

distribution of nitrogen dopants. At low doping levels (< 30 s nitrogenation), nitrogen atoms independently implant into the carbon lattice, resulting in a rapid conductivity degradation of graphene. In contrast, at high doping levels (between 30 and 60 s nitrogenation), clustering at the pre-existing nitrogen doping sites occurs and results in no further degradation of the conductivity of graphene. Moreover, the large decrease of the minimum conductivity G_{\min} from 0 to 30 s nitrogenation and stable value of G_{\min} between 30 to 60 s of nitrogenation (Figure 3.2e) further confirm that nitrogenated defects are the dominating scatterers for the charge carriers in graphene.^[24] These observations reveal that nitrogen dopants in the monolayer graphene lattice cause significant intervalley scattering, reduce the carrier mobility and (minimum) conductivity, and negatively shift the CNP by inducing an n-doping effect.

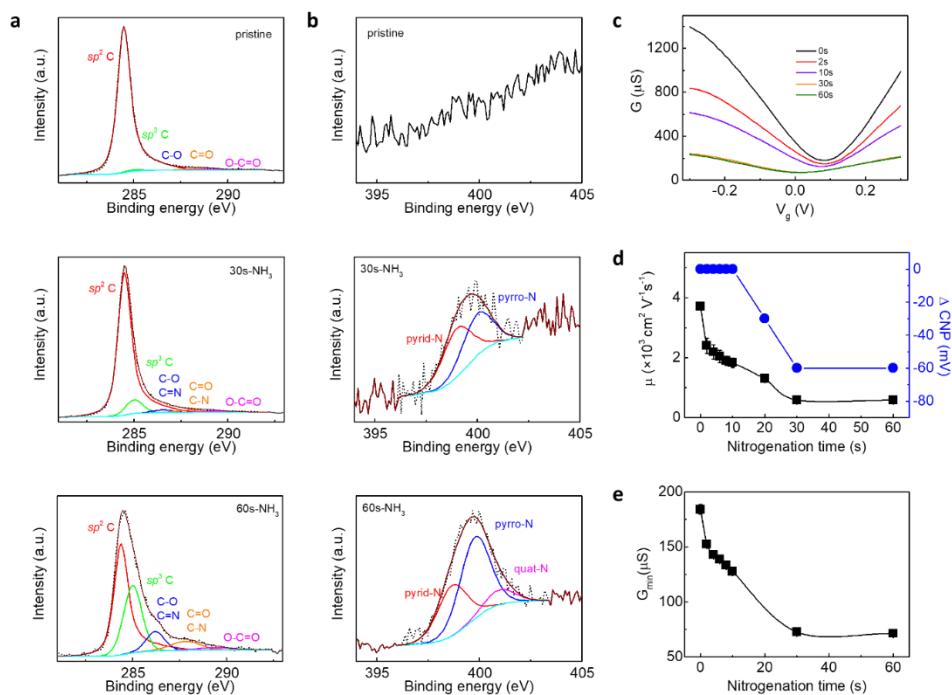


Figure 3.2 Electronic/structural characterization of N-doped graphene. a) C1s core level high-resolution XPS spectra of pristine, 30 s and 60 s N-doped graphene. b) N1s core level spectra of pristine, 30 s and 60 s N-doped graphene. All the spectra were collected from the CVD graphene as grown on copper foil in a fresh status (i.e. within one week after the CVD growth). c) Conductance (G) vs the gate voltage (V_g) curves of graphene upon nitrogenation time from 0 to 60 s. The electrolyte solution is 0.1 M KCl with 10 mM Tris (pH 8). d) The carrier mobility (μ , black square) and charge neutrality point (CNP, blue dot) evolve with the nitrogenated times. e) The minimum conductance (G_{\min}) as a function of the nitrogenation time.

3.2.4 ORR activity of N-doped and O-doped graphene

The ORR activity was first studied with the clean graphene surface on the epoxy substrate (illustrated in Figure AII. 3a), which was also used for the transport measurements described in the previous section.^[21] In this setup, the well-defined monolayer graphene is the only catalytic surface available to perform the ORR, and is referred to as pure graphene. More importantly, the obtained pure graphene samples were tested as fresh as possible, to minimize air contaminations (i.e. oxidation or hydrocarbon adsorption).^[21, 25] As will be shown later, the ORR polarization curves can also reflect sample freshness and reliability. Figure 3.3 shows the cyclic voltammograms (CVs) and the linear sweep voltammograms (LSVs) of the pure graphene in 0.1 M H₂SO₄ and 0.1 M NaOH solution saturated with O₂ in a stationary configuration. A more positive onset potential in alkaline medium (~0.68V) than in acidic medium (~0 V), and a higher current density (~4-fold at -0.2 V) in 0.1 M NaOH shows the higher ORR activity in alkaline medium (Figure 3.3a). It is well known that carbon-based catalyst are more active for the ORR in alkaline media. This is most likely due to O₂⁻ being the first intermediate in the mechanism of ORR, which is formed by an electron transfer reaction that is not coupled to proton transfer and therefore does not scale linearly with the RHE reference scale.^[26] The LSV curves in alkaline medium have an extra reduction peak at ca. 0.45V. This peak is ascribed to oxygen reduction catalyzed by the oxygen-containing groups present on the surface of graphene and other carbon electrodes including glassy carbon.^[27] In addition, more aged pristine graphene showed increased current in this region (Figure AII. 4a). Therefore, only pristine graphene samples producing similar or lower peak currents at 0.45 V compared to the LSV in Figure 3.3a are used for doping treatment studies. Upon nitrogen doping from 0 to 60 s, the catalytic current densities are observed to decrease monotonically both in acidic (Figure 3.3b) and in alkaline medium (Figure 3.3c). This is in contrast with the earlier reports that claim that n-doping of nitrogenated graphene improves ORR activity by creating Lewis basic sites which enhance initial O₂ adsorption.^[2a, 3] In our case, the observed decrease in ORR activity of graphene after nitrogenation suggests that the N-doping sites within the graphene surface do not contribute to the generation of active catalytic sites. In fact, recent reports support the observation that the catalytic activity of graphene decreases upon nitrogenation.^[5] For example, N-doped graphene was reported to show similar ORR activity with pristine graphene.^[5b] A theoretical study proposes that the nitrogen atoms in N-doped graphene could actually hinder the adsorption of oxygen molecules onto the graphene surface due to their higher electron density.^[28]

Inspired by the recent work that oxygen-containing groups in carbon-based materials are closely related to the active ORR performance,^[2a, 3] oxygen groups via oxygen

plasma treatment was further co-doped into the nitrogenated graphene. As illustrated in Figure 3.3d, the ORR activity for 60 s nitrogenated graphene is decreased as compared to pristine graphene. In contrast, co-doped graphene that is treated by both 60 s nitrogenation and 10 s of oxygenation enhances the ORR activity. However, more oxygen doping in the co-doped graphene (60 s nitrogenation and 30 s oxygenation) impairs the positive effect of oxygen doping on the ORR activity. Apparently, nitrogenated graphene is only active for ORR catalysis in the presence of a certain amount of co-doped oxygen groups.

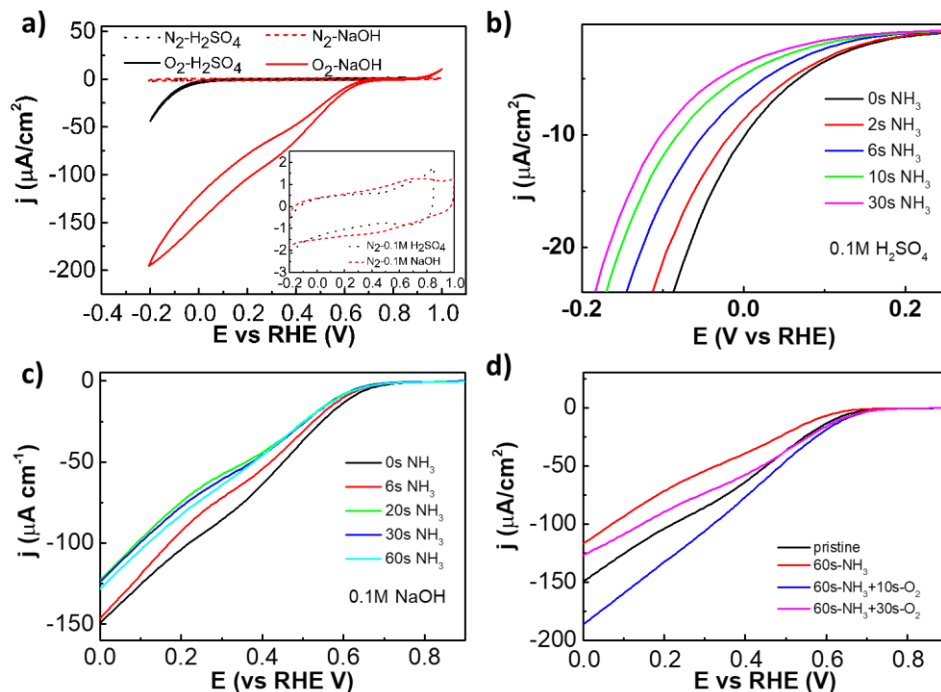


Figure 3.3 ORR activity on the pure graphene upon nitrogenation and oxygenation treatments. a) Cyclic voltammetry (CV) curves of monolayer graphene in 0.1 M H₂SO₄ and 0.1 M NaOH solutions saturated with N₂ and O₂, respectively. b) Linear sweep voltammetry (LSV) polarization curves of graphene upon 0 to 30 s of nitrogenation in O₂-saturated 0.1 M H₂SO₄. c) LSV curves of graphene upon 0 to 60 s of nitrogenation in O₂-saturated 0.1 M NaOH. d) Comparison of LSV curves in O₂-saturated 0.1 M NaOH for pristine graphene, nitrogenated graphene (60s-NH₃), and graphene co-doped with nitrogen and oxygen (60s-NH₃+10s-O₂) and 30 s (60s-NH₃+30s-O₂).

3.2.5 ORR kinetics and selectivity of N-doped and O-doped graphene

A rotating ring-disk electrode (RRDE) method was further employed to gain insights into the product selectivity and the ORR kinetics of nitrogenated graphene. The current was measured at both the glassy carbon (GC) disk and the platinum ring. The

Pt ring was held at a potential of 1.2 V, to oxidize ORR products such as hydrogen peroxide HO_2^- (the form of H_2O_2 in alkaline medium) and/or superoxide O_2^- . Graphene was transferred onto the GC disk via the traditional polymer assistant method (see Figure AII. 3b and Methods).^[22] Importantly, the opposite face of graphene is exposed as compared to the previously described graphene on epoxy substrate (pure graphene). XPS analysis reveals that this graphene surface contains oxygen functionalities, which is probably due to air-induced contaminations and oxidation (Figure 3.2). As shown in Figure 3.4a, a monolayer graphene on the GC disk decreases the ORR current compared to that of bare GC, indicating that fewer active sites are available on the graphene surface. Furthermore, bilayer graphene on GC has an even more reduced ORR current compared to the monolayer graphene. This implies that the GC as the underlying substrate has a certain influence on the catalysis of the graphene overlayer, for instance through cracks in this monolayer graphene film. In contrast, the bilayer graphene displays better reproducibility and reliability (see Figure AII. 4 and Appendix II. 4). Therefore, the bilayer graphene was used for the RRDE measurements and referred to as RRDE graphene. Compared to the LSV of pure graphene, RRDE graphene (at 0 rpm) has a more pronounced peak at 0.45 V (Figure 3.4b). As previously described, this feature relates to a higher surface oxidation of RRDE graphene as compared to pure graphene.

Under rotating conditions from 400 to 1000 rpm, the LSV of bare GC in O_2 saturated 0.1 M NaOH shows increasing disk and ring currents (Figure 3.4c). Fully diffusion-limited currents were never reached at the GC disk nor for RRDE graphene (*vide infra*), neither for HOPG as was reported previously.^[3] Figure 3.4d shows the LSV curves of RRDE graphene before (as the pristine sample) and after nitrogenation and oxygenation treatments. The ORR activity of 30 s nitrogenated RRDE graphene (N30) is slightly decreased as compared to pristine graphene. In contrast, 60 s nitrogenated graphene (N60) shows significantly increased ORR activity. Likewise, 10 s oxygenated graphene (O10) also displays an improved current, indicating that nitrogen atoms in graphene are not necessary for enhanced ORR activity. The co-doped graphene with 30 s of nitrogenation and 10 s of oxygenation (N30-O10) demonstrates the highest current among all the doped samples. Of note, the increased ORR current for N60 RRDE graphene conflicts with the decreased activity found for the corresponding pure graphene (see Figure 3.3c). As stated before, RRDE graphene has more oxygen containing groups than pure graphene due to the differently exposed faces of graphene. A different explanation is that vacancy defects, that are generally generated together with N dopants, might expose the underlying GC disk and thus GC could contribute to the ORR activity for the RRDE graphene. To test this possibility, the ORR currents of N60 graphene (on RRDE), a bare GC disk and partially

exposed GC (from 10% to 50% in terms of area) were compared (Figure AII. 5). Due to the large amounts of defects and oxygen functionalities, bare GC exhibits a distinct polarization curve with a prominent extra peak at ca. 0.45 V. In contrast, N60 graphene exhibits a much larger ORR current at high overpotential (near 0 V vs RHE) and a relatively lower current at 0.45 V compared to all partially exposed GC electrodes. It can therefore be concluded that the underlying GC substrate plays a negligible role in the ORR activity of N60 RRDE graphene.

The RRDE method allows for product selectivity studies by using both the Koutecky-Levich method and by comparing currents obtained on the ring and on the disk ($I_{\text{ring}}/I_{\text{disk}}$, see Appendix II. 5). At the ring, both superoxide O_2^- and hydrogen peroxide H_2O_2 can be oxidized. Higher ratios of $I_{\text{ring}}/I_{\text{disk}}$ reflect higher selectivity towards O_2^- and H_2O_2 , while in return lower ratios indicate that more H_2O may be produced. In Figure AII. 8b, the selectivity is calculated based on the current values in the potential range of 0~0.1 V with a collection efficiency of 22.5% at the ring (see Figure AII. 6 and Appendix II. 5). The $I_{\text{ring}}/I_{\text{disk}}$ ratio is as low as 36% for bare GC, which is traditionally known to reduce O_2 to HO_2^- with 100% through a 2e⁻ pathway.^[29] The observed lower ratio suggest that the collection efficiency of HO_2^- is underestimated by the RRDE technique, as the oxidation of HO_2^- at the platinum ring is surface dependent and therefore not fully mass transport limited. Therefore, the collection efficiency can be lower than that for the ferricyanide.^[30] In comparison to GC, pristine graphene exhibits a higher selectivity ratio of 47%. Similar ratios are found for N30 (~48%) and N60 (~47%), while slightly decreased ratios for O10 (~45%) and N30-O10 (~42%) are found. The higher selectivity ratios on pristine and doped graphene samples suggest that more superoxide might be produced (it is anticipated that superoxide, in contrast to peroxide, is oxidized via an outer-sphere reaction), which agrees well with the lower n values (~1.6 – 1.8). Most likely, most active sites produce HO_2^- and/or O_2^- but no clear correlation was found with the presence of certain nitrogen and/or oxygen functionalities.

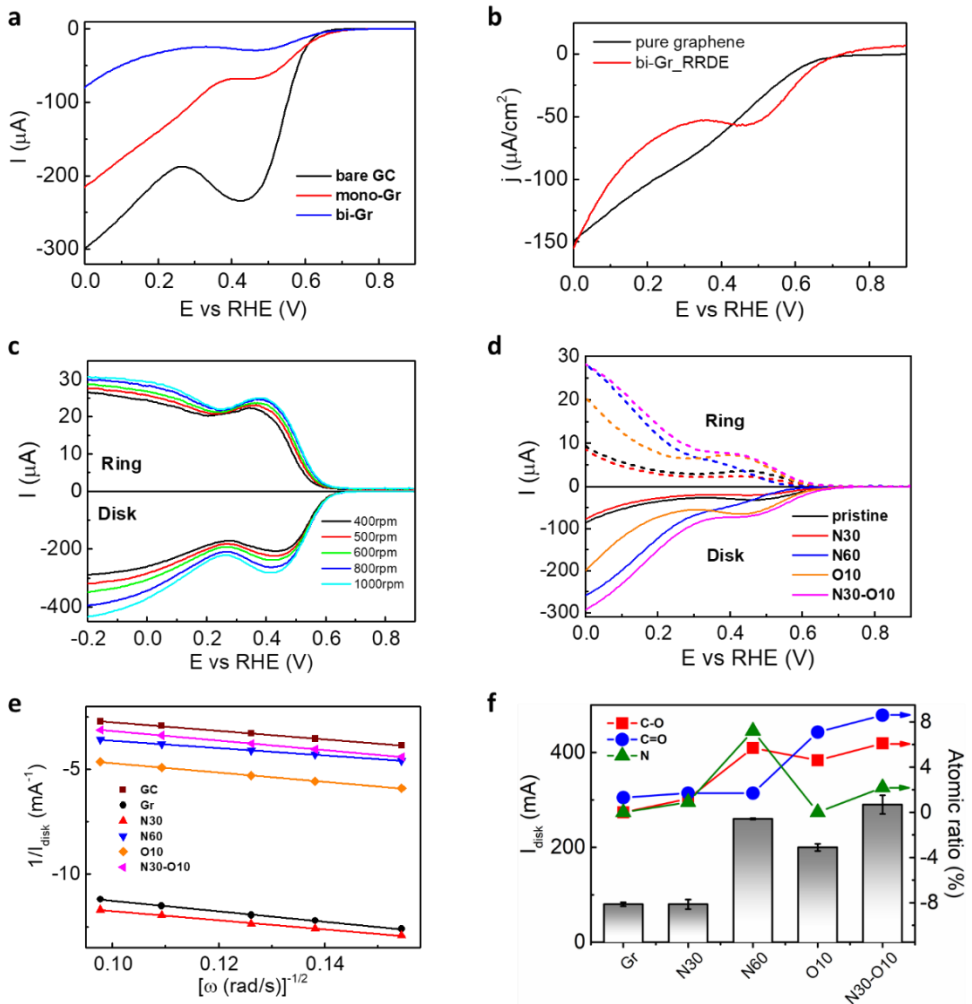


Figure 3.4 ORR activity and selectivity of N-doped graphene. a) LSV curves of bare GC, monolayer (mono-Gr) and bilayer (bi-Gr) graphene on the GC disk at 600 rpm. b) Polarization curves of a pure graphene supported by epoxy substrate and a (bilayer) RREDE graphene on the GC without rotation. c) Polarization curves of bare GC and ring electrode at rotation speed varying from 400 to 1000 rpm. d) Polarization curves of graphene after nitrogenation and/or oxygenation and simultaneous H_2O_2 detection currents at the ring electrode (at 800 rpm). "Pristine" denotes the pristine RRDE graphene. "N30" and "N60" represent 30 s and 60 s of nitrogenated graphene, respectively, while "O10" for 10 s of oxygenated graphene. e) Koutecky-Levich plots of different doped graphene samples at 0 V. f) Correlation of cathodic currents at 0 V with atomic ratios (%) of C-O, C=O and N dopants for the different doped graphene samples. All the ORR experiments were performed in 0.1 M NaOH solutions saturated with O_2 .

The Koutecky-Levich method (Figure 3.4e) confirms the best ORR activity on the co-doped sample (N30-O10) while the lowest activity on the pristine and N30 graphene. The origins of the Koutecky-Levich plots are summarized in Figure AII. 7. Based on the Koutecky-Levich curves, we calculate the electron transfer number (n) per O_2 molecule in the potential window of 0 to 0.2 V for the GC and different graphene surfaces. In contrast to bare GC which has an n value of 2 (Figure AII. 8a), pristine graphene has a lower value of 1.6, indicating the formation of less reduced products, i.e. O_2^- ($1e^-$). After doping treatments, the n value rises to 1.8 for most of the N- or O-doped samples suggesting that the heteroatoms doping may improve the selectivity of $2e^-$ or even $4e^-$ processes and thus produce more H_2O_2 and/or H_2O . Particularly, the largest n value of 2.3 for N60 suggests a higher selectivity for H_2O ($4e^-$) as product. The presence of quat-N only in 60 s N-doped graphene is the origin of this selectivity and agrees well with reports stating that quaternary nitrogen at the edge sites is positively related to this $4e^-$ pathway.^[2a]

Table 3.1 XPS analysis results for different doped graphene samples

samples	N/C (%)	Concentrations of species (%)									
		sp^2 C 284.4eV	sp^3 C 285.0eV	C-O/C=N 286.4eV		C=O/C-N 288eV		O-C=O 289.5eV	Pyrid-N 398.9eV	Pyrro-N 399.9eV	Quat-N 401.1eV
Pristine	0	96.6	1.1	0	0	1.3	0	1.0	-	-	-
N30	1.0	86.8	7.2	1.2	0.5	1.7	0.4	1.3	0.5	0.4	-
N60	7.7	47.3	29.0	5.7	2.7	1.7	4.5	2.1	2.4	4.5	0.3
O10	0	76.2	7.4	4.6	0	7.1	0	4.7	-	-	-
N30-O10	2.3	68.4	8.4	6.1	0.6	8.6	1.6	4.0	0.6	1.6	-

3.2.6 Identification of ORR catalytic sites in N-doped and O-doped graphene

The same graphene surfaces used for RRDE experiments were analyzed by XPS as well. This way, the ORR activity can be correlated with the chemical structures of different doped graphene samples. Table 3.1 summarizes the concentrations of different C and N species and their relative ratios (the C1s spectra of O10 and N30-O10 graphene are displayed in Figure AII. 2d-e). As shown in the C1s deconvolution, the binding energies of C-O and C=O overlap with that of C=N (pyrid- and quat-N) and C-N (pyrro-N), respectively. By calibrating the atomic ratios according to the peak areas and relative sensitivity factor (RSF), the respective atomic ratios (abbreviated: at.%) for C-O and C=O groups are obtained. Figure 3.4f shows the correlations of the ORR activities of different doped graphene samples with their corresponding atomic ratios of C-O, C=O and N atoms. The disk currents at 0 V vs RHE increase with the

percentage of C-O whereas no apparent correlation with the content of C=O or N dopants is found. The high atomic ratios of C-O in N60 graphene as well as the improved activity in O10 samples both suggest that nitrogen functionalities are of less relevance for the ORR activity as compared to C-O groups. In other words, C-O functionalities in nitrogenated graphene are responsible for enhanced ORR activity. To the best of our knowledge, this is the first experimental evidence revealing that oxygen containing groups, instead of nitrogen atoms, are the origin for improved ORR electrocatalysis in nitrogenated graphene.

3.3 Conclusions

In summary, nitrogenation and oxygenation of graphene have been systematically controlled for the investigation of the corresponding impacts on its electrical properties and ORR performance. Characterized by Raman spectroscopy and transport measurements, after nitrogenation treatments graphene preserves a high graphitization level and lattice integrity with an n-doping effect. Graphene supported by epoxy substrate is found to be inactive for ORR upon nitrogen doping unless oxygen groups are introduced as co-doping contents. In contrast, RRDE graphene exhibits enhanced ORR activity after the same nitrogenation treatments due to the higher amount of surface oxidation. Further structure-activity correlations obtained from the RRDE system reveal that singly bonded carbon-oxygen groups rather than the N-doping sites in nitrogenated graphene are positively correlated to the enhanced ORR activity. In this study, C-O groups in the basal plane of nitrogenated graphene are pinpointed as the active sites for the ORR. Furthermore our work shows that research into nitrogen-doped graphene for enhanced ORR catalysis should critically evaluate the role of oxygen impurities.

3.4 References

- [1] a) K. Gong, F. Du, Z. Xia, M. Durstock, L. Dai, *Science* **2009**, 323, 760; b) J. Shui, M. Wang, F. Du, L. Dai, *Sci. Adv.* **2015**, 1, e1400129; c) Y. Ito, H. J. Qiu, T. Fujita, Y. Tanabe, K. Tanigaki, M. Chen, *Adv. Mater.* **2014**, 26, 4145; d) L. Qu, Y. Liu, J.-B. Baek, L. Dai, *ACS Nano* **2010**, 4, 1321.
- [2] a) H. B. Yang, J. Miao, S.-F. Hung, J. Chen, H. B. Tao, X. Wang, L. Zhang, R. Chen, J. Gao, H. M. Chen, *Sci. Adv.* **2016**, 2, e1501122; b) L. Lai, J. R. Potts, D. Zhan, L. Wang, C. K. Poh, C. Tang, H. Gong, Z. Shen, J. Lin, R. S. Ruoff, *Energy Environ. Sci.* **2012**, 5, 7936; c) T. Wang, Z.-X. Chen, Y.-G. Chen, L.-J. Yang, X.-D. Yang, J.-Y. Ye, H.-P. Xia, Z.-Y. Zhou, S.-G. Sun, *ACS Energy Lett.* **2018**, 3, 986.

- [3] D. Guo, R. Shibuya, C. Akiba, S. Saji, T. Kondo, J. Nakamura, *Science* **2016**, 351, 361.
- [4] Y. Zheng, Y. Jiao, L. H. Li, T. Xing, Y. Chen, M. Jaroniec, S. Z. Qiao, *ACS Nano* **2014**, 8, 5290.
- [5] a) Z. Luo, S. Lim, Z. Tian, J. Shang, L. Lai, B. MacDonald, C. Fu, Z. Shen, T. Yu, J. Lin, *J. Mater. Chem.* **2011**, 21, 8038; b) Y. Jia, L. Zhang, A. Du, G. Gao, J. Chen, X. Yan, C. L. Brown, X. Yao, *Adv. Mater.* **2016**, 28, 9532.
- [6] Y. Jia, L. Zhang, L. Zhuang, H. Liu, X. Yan, X. Wang, J. Liu, J. Wang, Y. Zheng, Z. Xiao, *Nat. Catal.* **2019**, 2, 688.
- [7] a) Q. Li, S. Zhang, L. Dai, L.-s. Li, *J. Am. Chem. Soc.* **2012**, 134, 18932; b) L. J. Cote, F. Kim, J. Huang, *J. Am. Chem. Soc.* **2008**, 131, 1043.
- [8] a) Z. Lu, G. Chen, S. Siahrostami, Z. Chen, K. Liu, J. Xie, L. Liao, T. Wu, D. Lin, Y. Liu, *Nat. Catal.* **2018**, 1, 156; b) H. W. Kim, M. B. Ross, N. Kornienko, L. Zhang, J. Guo, P. Yang, B. D. McCloskey, *Nat. Catal.* **2018**, 1, 282.
- [9] L. R. Radovic, A. J. Salgado-Casanova, *Carbon* **2018**, 126, 443.
- [10] L. A. Belyaeva, W. Fu, H. Arjmandi-Tash, G. g. F. Schneider, *ACS Cent. Sci.* **2016**, 2, 904.
- [11] a) A. V. Prydatko, L. A. Belyaeva, L. Jiang, L. M. Lima, G. F. Schneider, *Nat. Commun.* **2018**, 9, 4185; b) L. Zhang, J. Yu, M. Yang, Q. Xie, H. Peng, Z. Liu, *Nat. Commun.* **2013**, 4, 1443.
- [12] A. C. Ferrari, D. M. Basko, *Nat. Nanotechnol.* **2013**, 8, 235.
- [13] F. Tuinstra, J. L. Koenig, *J. Chem. Phys.* **1970**, 53, 1126.
- [14] a) P. Lespade, A. Marchand, M. Couzi, F. Cruege, *Carbon* **1984**, 22, 375; b) A. Eckmann, A. Felten, I. Verzhbitskiy, R. Davey, C. Casiraghi, *Phys. Rev. B* **2013**, 88, 035426.
- [15] a) M. Bruna, A. K. Ott, M. Ijäs, D. Yoon, U. Sassi, A. C. Ferrari, *ACS Nano* **2014**, 8, 7432; b) A. Das, S. Pisana, B. Chakraborty, S. Piscanec, S. Saha, U. Waghmare, K. Novoselov, H. Krishnamurthy, A. Geim, A. Ferrari, *Nat. Nanotechnol.* **2008**, 3, 210; c) Q. H. Wang, C.-J. Shih, G. L. Paulus, M. S. Strano, *J. Am. Chem. Soc.* **2013**, 135, 18866.

- [16] M. M. Lucchese, F. Stavale, E. M. Ferreira, C. Vilani, M. Moutinho, R. B. Capaz, C. Achete, A. Jorio, *Carbon* **2010**, 48, 1592.
- [17] Z. Zafar, Z. H. Ni, X. Wu, Z. X. Shi, H. Y. Nan, J. Bai, L. T. Sun, *Carbon* **2013**, 61, 57.
- [18] A. Eckmann, A. Felten, A. Mishchenko, L. Britnell, R. Krupke, K. S. Novoselov, C. Casiraghi, *Nano Lett.* **2012**, 12, 3925.
- [19] a) C. Zhang, L. Fu, N. Liu, M. Liu, Y. Wang, Z. Liu, *Adv. Mater.* **2011**, 23, 1020; b) L. Tang, R. Ji, X. Li, K. S. Teng, S. P. Lau, *J. Mater. Chem. C* **2013**, 1, 4908.
- [20] G. Abbas, P. Papakonstantinou, G. R. Iyer, I. W. Kirkman, L. C. Chen, *Phys. Rev. B* **2007**, 75, 195429.
- [21] L. Jiang, W. Fu, Y. Y. Birdja, M. T. Koper, G. F. Schneider, *Nat. Commun.* **2018**, 9, 793.
- [22] J. W. Suk, A. Kitt, C. W. Magnuson, Y. Hao, S. Ahmed, J. An, A. K. Swan, B. B. Goldberg, R. S. Ruoff, *ACS Nano* **2011**, 5, 6916.
- [23] F. Chen, Q. Qing, J. Xia, N. Tao, *Chem. Asian J.* **2010**, 5, 2144.
- [24] J.-H. Chen, W. Cullen, C. Jang, M. Fuhrer, E. Williams, *Phys. Rev. Lett.* **2009**, 102, 236805.
- [25] A. Ashraf, Y. Wu, M. C. Wang, N. R. Aluru, S. A. Dastgheib, S. Nam, *Langmuir* **2014**, 30, 12827.
- [26] B. Blizanac, P. Ross, N. Markovic, *Electrochim. Acta* **2007**, 52, 2264.
- [27] A. Sarapuu, K. Helstein, K. Vaik, D. J. Schiffrin, K. Tammeveski, *Electrochim. Acta* **2010**, 55, 6376.
- [28] N. Daems, X. Sheng, I. F. Vankelecom, P. P. Pescarmona, *J. Mater. Chem. A* **2014**, 2, 4085.
- [29] C. Song, J. Zhang, in *PEM fuel cell electrocatalysts and catalyst layers*, Springer **2008**, p. 89.
- [30] a) S. B. Hall, E. A. Khudaish, A. L. Hart, *Electrochim. Acta* **1999**, 44, 4573; b) R. Zhou, Y. Zheng, M. Jaroniec, S.-Z. Qiao, *ACS Catal.* **2016**, 6, 4720; c) S. B. Hall, E. A. Khudaish, A. L. Hart, *Electrochim. Acta* **1998**, 43, 579.

Chapter 4

Hydrogenation cleans up airborne contamination from graphene

Graphene as a two-dimensional surface is prone to airborne contaminations, which can significantly impact surface-related properties including electrochemistry and wettability. Here, by combining multiscale characterization techniques, hydrogenation treatment as a non-invasive strategy is demonstrated to remove the hydrocarbon contamination from the graphene surface while preserving graphene crystallinity. The hydrogenated graphene manifests enhanced water adsorption as compared to its pristine state, resulting in a protective layer against the redeposition of hydrocarbon molecules. Our findings provide a new strategy for graphene to maintain its surface cleanliness, inherently improving performance in biosensing and interfacing applications.

This chapter was prepared as an article: Lin Jiang, Pauline M.G. van Deursen, Hadi Arjmandi-Tash, Liubov A. Belyaeva, Haoyuan Qi, Jiao He, Vincent Kofman, Longfei Wu, Valerii Muravev, Ute Kaiser, Harold Linnartz, Emiel J.M. Hensen, Jan P. Hofmann, Grégory F. Schneider, submitted.

4.1 Introduction

Cutting-edge applications involving a graphene surface require a clean surface and a precise knowledge of the chemical structure of the basal plane. However, surface contaminations introduced during device fabrication processes can have a significant and unpredictable impact on the electrical and electrochemical properties of graphene. For chemical vapor deposition (CVD) graphene, the majority of the accumulated contaminations originate from the transfer-assisting polymer (typically poly(methyl methacrylate), PMMA). To date, many efforts have been devoted to removing PMMA residues, i.e. with the use of annealing in vacuum or specific atmospheres (air or H₂/Ar mixture)^[1], mechanical removal of contaminants by AFM scanning^[2], current cleaning^[3], electrostatic force cleaning^[4] or plasma dry-cleaning^[5]. In particular, hydrogen plasma has been intensively studied for patterning and etching graphite surfaces.^[6] By tuning the energy of the involved hydrogen species impinging on the surfaces one can control and customize, in principle, the morphology and functionalization of graphene.^[7]

In previous work, we showed that the electrochemical activity of graphene can be enhanced by just one second of hydrogen plasma treatment, but decreases with prolonged hydrogenation.^[8] The decrease of electrochemical activity can be attributed to changes in the electronic structure of the graphene layer. According to non-adiabatic theory for electron transfer, decreasing electrochemical activity is due to the reduction of the density of states (DOS) in graphene. On the other hand, the electrochemical activity improvement – by up to 12-fold after one second of hydrogenation – is expected to be related to the removal of airborne hydrocarbons at the graphene surface. Airborne contaminations mainly composed of various hydrocarbons, are pervasive in the ambient conditions, and can adsorb onto graphene via hydrophobic interactions to form an amorphous coating.^[9] However, few efforts have been devoted to removing airborne hydrocarbons,^[9] despite the influence of those hydrocarbons on the wettability and even the electrochemical kinetics of the surface of graphene or graphite.^[10] Such uncontrolled surface chemistry and substantial variation in electrical performances of graphene pose significant challenges which remain to be solved.

Here, the cleaning effect upon hydrogenation is demonstrated to result in graphene with well-maintained lattice integrity and crystallinity, as confirmed using aberration-corrected high-resolution transmission electron microscopy (AC-HRTEM). Further statistical analysis of the TEM images quantitatively evaluates the cleanliness of graphene surfaces, defined as the proportion of the area on the crystalline lattice without amorphous coverage in TEM images. Specifically the focus

is on water adsorption, which has been reported to act in concert with hydrogenation and effectively impacts the doping behavior in graphene.^[11] Furthermore, chemical water adsorption was confirmed to potentially minimize hydrocarbon contaminations at graphitic surfaces.^[12] As a result, it is hypothesized that in addition to chemically modifying the basal plane from sp^2 to sp^3 , hydrogenation also cleans graphene by removing surface adsorbed hydrocarbons, and preserves the cleanliness through the adsorption of a water protecting layer. Thus, hydrogenation can effectively improve the anti-fouling capability of the graphene basal plane towards airborne contaminations. This process is further studied using temperature programmed desorption-infrared spectroscopy (TPD-IR) and near-ambient pressure X-ray photoelectron spectroscopy (NAP-XPS) confirming the preferred adsorption of water at the hydrogenated graphene surface.

4.2 Results

4.2.1 High resolution transmission electron microscopy (HRTEM)

The surface morphology of graphene films grown by CVD method^[13] was studied by AC-HRTEM, to compare the effects of hydrogen and argon plasma on surface cleanliness. A capacitively coupled plasma system (Diener electronic, Femto) was used to form mild plasma via tuning the power and gas pressures. Three types of graphene treatments are investigated: 1) hydrogen-treated graphene (H-graphene), 2) argon treated graphene (Ar-graphene), 3) as-synthesized graphene without plasma exposure ("pristine" graphene). For a fair and reliable comparison, both the H- and Ar-graphene contain similar amounts of corresponding H or vacancy defects^[8], confirmed by Raman spectroscopy (Figure AIII. 1). Figure 4.1a shows the HRTEM image of H-graphene exposed to hydrogen plasma for 60 seconds, in which the first-order reflections of graphene are clearly visible in the fast Fourier transform (FFT) pattern. The amorphous residuals are surface contaminations, originating from the preparation procedures (unavoidable solvents or aqueous solutions) and airborne hydrocarbons.^[9] By introducing the same amount of defect density, argon plasma was tested as a control to further confirm the cleaning effect. In contrast to the HRTEM image of pristine graphene in Figure AIII. 2, both H-graphene and Ar-graphene graphene show improved cleanliness. Compared to the one treated with argon plasma (Ar-graphene) (Figure 4.1b), a cleaner graphene lattice with less coverage of amorphous carbon has been found in hydrogenated graphene (H-graphene) (Figure 4.1a). Particularly, a close-up of Figure 4.1a-b presented in Figure 4.1c-f clearly shows the atomically resolved graphene lattice, confirming the relatively larger area of clean and preserved surface crystallinity in H-graphene. Different from the visible hole/vacancy^[14] formed in Ar-graphene (Figure 4.1f), a point defect in H-graphene is suspected to be related to the hydrogenation or the damage by the electron beam during imaging (Figure 4.1e). As

a result, the hypothesis is that, without sacrificing the integrity and crystallinity, hydrogenation cleans off the amorphous contaminants on the graphene surface while uniformly hybridizing graphene lattice from sp^2 to sp^3 .

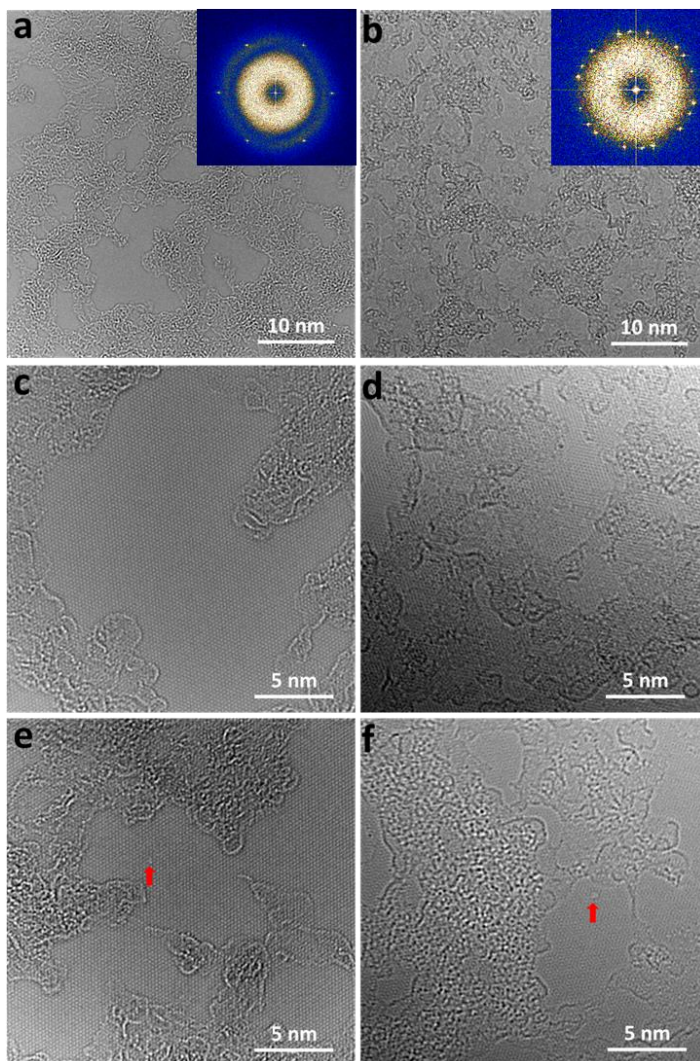


Figure 4.1 Comparison of graphene surfaces upon hydrogen vs argon plasma treatments by high resolution transmission electron microscopy (HRTEM). a) HRTEM image of graphene after 60 s of hydrogenation (H-graphene). The inset FFT pattern shows six reflections 4.7 nm^{-1} , demonstrating the preservation of graphene crystallinity. b) HRTEM image of graphene bombarded for 13 s of argon plasma (Ar-graphene). The FFT with 18 reflections suggests a trilayer-like graphene stack with 3 orientations. c) A zoomed-in HRTEM image of the H-graphene. d) A zoomed-in HRTEM image of the Ar-graphene. e) HRTEM image of H-graphene with visible lattice defect indicated by the red arrow. f) HRTEM image of Ar-graphene with a void indicated by the red arrow.

4.2.2 Quantitative analysis of the cleanliness of hydrogenated graphene

To gain quantitative insights into the cleaning effect upon hydrogenation, a statistical analysis of the TEM images of graphene acquired with a larger field-of-view was performed. For H-graphene (Figure 4.2a, 60 s of hydrogenation), contaminations appear in patterns with more rough sites while clean lattice being more smooth. By converting the TEM image into a black-white binary image, the cleanliness within the field-of-view can be quantitatively evaluated. A MATLAB script (see Appendix III. 2) was developed to process TEM micrographs and to identify the surface contaminations automatically. Table AIII. 1 details the process within the script. Figure 4.2a illustrates a selected region in the TEM image of H-graphene before (left) and after (right) image processing. The black pixels in the right panel correspond to the identified contaminations in graphene. Using the processed images, the graphene “cleanliness” is defined as the ratio of clean area in the image. Specifically, the cleanliness of the image is calculated as the sum of the number of white pixels (clean graphene area) normalized by the total number of pixels.

Figure 4.2b shows the contrast of the general cleanliness between the surfaces of pristine and H-graphene. Based on a statistical analysis of 15 images for the two types of surfaces, the quantitative evaluation of the cleanliness is summarized in Figure 4.2c. Both the narrower distribution around the average and clearly higher values of cleanliness indicate that contaminations on the surface of H-graphene are considerably less. Moreover, the amorphous contaminations exhibit a more homogeneous morphology after hydrogenation.

Hydrogen plasma has been found previously to be able to remove polymer (i.e. poly-methyl-methacrylate) that is prone to leave residues on graphene.^[5a, 5c] Here for the first time the cleaning effect of hydrogenation is demonstrated towards hydrocarbon contaminations adsorbed on graphene surfaces. In our previous study on H-graphene^[8], an hydrogenation-induced p-doping effect was reported, which can be ascribed to surface adsorbed water. In addition, H-graphene was reported to show n-doping behavior after heating the sample in vacuum.^[11] More unambiguous proof of the presence of adsorbed water on graphene surfaces and its cleaning effect towards the ubiquitous airborne contaminations is still lacking.

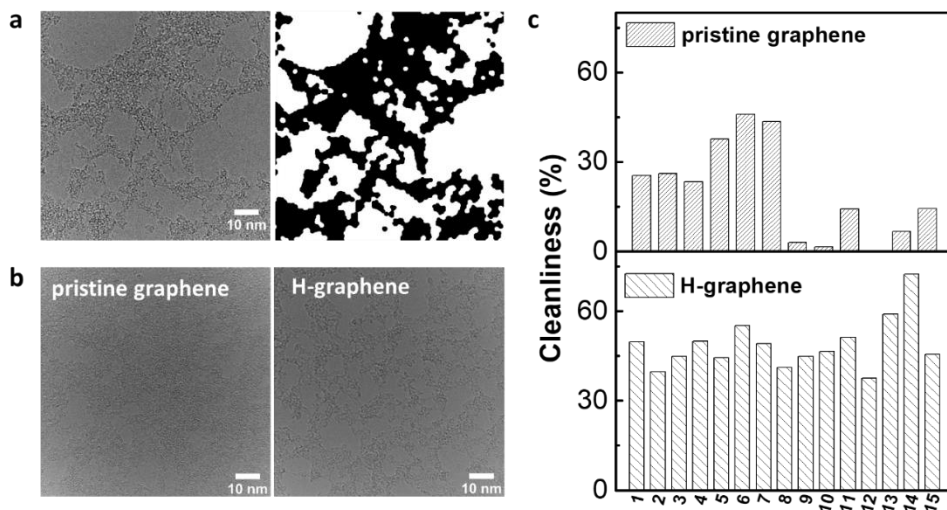


Figure 4.2 Quantitative analysis of graphene cleanliness in TEM images. a) TEM image of H-graphene (60 s) and its corresponding binary image distinguishing the clean and contaminated areas with white and black colors. The cleanliness ($\sim 52\%$) can be estimated based on the white pixels divided by the overall pixels. b) TEM image of pristine graphene and H-graphene upon 60 s of hydrogenation. c) Quantitative statistics of the cleanliness of graphene and hydrogenated graphene for 15 separate measurements.

4.2.3 Temperature programmed desorption-Infrared spectroscopy (TPD-IR)

To further understand the cleaning effect of hydrogenation and water adsorption on graphene, temperature-programmed desorption-infrared spectroscopy (TPD-IR) was performed. For this, a graphene sample was transferred via a biphasic polymer-free transfer method^[15] on one side of an IR-transparent BaF₂ window that is mounted on the tip of a 15 K cryostat, positioned in the center of a high vacuum (HV) chamber in which the measurements were performed.^[16] The HV chamber has a base pressure of 5×10^{-9} mbar when the cryostat is on, and residual gas in the chamber is dominated by H₂O and H₂. Sample temperatures are set with ~ 2 K precision using thermocouples and a temperature controller. It should be noted that the temperature during water deposition is intentionally set to be higher than the typical thermal desorption temperature of water ice (~ 160 K), ensuring that water ice does not build up on the sample. The monolayer quality and lattice integrity of the transferred pristine and H-graphene are confirmed by the sharp and single-Lorentz fitted 2D peak (~ 2670 cm⁻¹) of the Raman spectra in the inset of Figure 4.3a-b. Specifically, the peak at 1350 cm⁻¹, an indicator of the presence and density of defects in graphene lattice, is confirmed to be more intensive for H-graphene.

After the cryostat cooled down, the sample was heated to 324 K (highest accessible temperature) to degas any water potentially adsorbed to the sample during transfer through the atmosphere. Next the sample was cooled down to 180 K; at this stage any water adsorption is expected to happen through accretion from the background gas. During water deposition, almost no change was observed in the IR spectra, indicating that during cooling from 324 K to 180 K, the graphene surface was already water saturated. Further exposure to water did not lead to a further increase of H₂O related bands in the IR spectra. After water deposition, the sample was heated up with a linear ramp rate of 3 K per minute to 324 K to desorb the water from graphene. IR spectra were collected during the heating process.

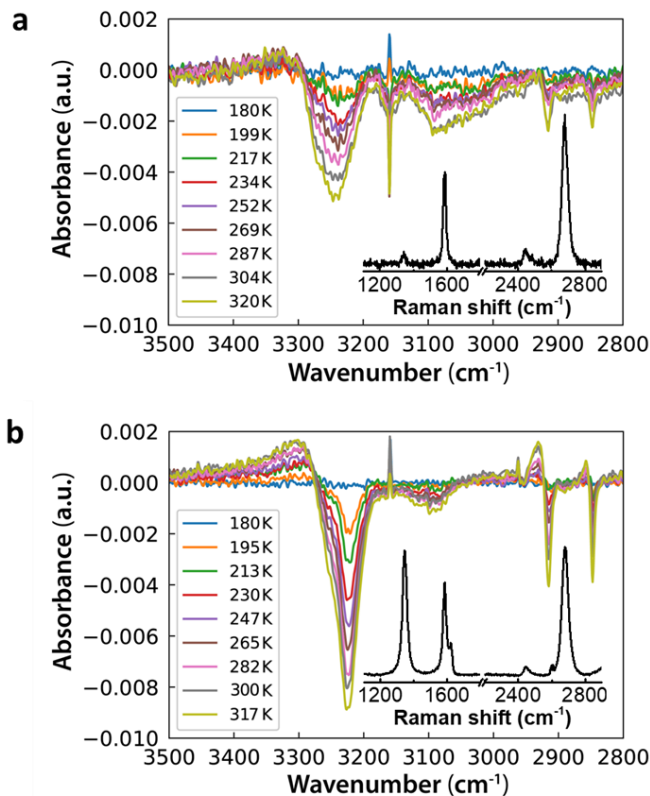


Figure 4.3 Water adsorption tests on graphene surfaces characterized by temperature-programmed desorption-infrared spectroscopy (TPD-IR). a) IR spectrum of pristine graphene for temperatures increasing from 180 to 320 K with increments of 15 to 20 K. b) IR spectrum of H-graphene (60 s) during a ramp-up in temperature from 180 to 317 K. All graphene samples are deposited on a BaF₂ window via a polymer-free transfer method. The inset corresponds to Raman spectrum of pristine and H-graphene on a barium fluoride substrate, respectively.

Figure 4.3 shows the IR absorption spectra of the pristine and H-graphene during heating up from 180 K to 324 K. Each spectrum was calculated with respect to the background scan performed at 180 K to obtain the desorption signals (see background spectrum in Figure AIII. 3a-b). Two peaks appear at ~ 2924 and ~ 2852 cm^{-1} , corresponding to the stretching mode of the C-H bond. Particularly, the broad band appearing at ~ 3250 cm^{-1} is one of the vibrational modes of water and illustrates the level of water desorption at the graphene surfaces. At increasing temperatures, more water molecules desorb from the surface resulting in higher peak intensities. In addition, the IR spectra on H-graphene when cooling down from room temperature to 180 K exhibit a similar change in peak intensity (Figure AIII. 3c), indicating the reversibility of water adsorption. This study reveals that there is more water desorption from H-graphene surface between 180 K and 324 K (right panel) than that for the pristine one (left panel). This supports the proposition that hydrogenation treatment increases the water adsorption on graphene surface.

4.2.4 Near-atmosphere pressure-XPS analysis (NAP-XPS)

Near-ambient pressure X-ray photoelectron spectroscopy (NAP-XPS) was used to analyze the affinity of water towards the surface of graphene upon hydrogenation at a water vapor pressure of 1 mbar. The characterization was conducted directly on the CVD graphene as-grown on copper foil. Figure 4.4a-b shows the C1s and O 1s spectra for graphene samples under ultra-high vacuum (UHV) at a chamber pressure of $<10^{-9}$ mbar. The C1s peak can be deconvoluted into sp^2 C (284.2 eV), sp^3 C (284.8 eV), C-O (286.3 eV) and C=O (288.3 eV) components. The origin of sp^3 C in pristine graphene can be ascribed to the adventitious carbon adsorbed on the surface. The O1s spectrum in UHV can be fitted by three main components: Cu_2O (530.3 eV), O=C (531.3 eV) and O-C (532.3 eV) (Figure 4.4b). The presence of Cu_2O originates from the underlying copper substrate for graphene growth as the employed Al K α radiation leads to a probing depth of 2-5 nm. At near-ambient pressure conditions in the presence of 1.0 mbar of H_2O , another peak arises at 535.3 eV (Figure 4.4c) which is ascribed to water molecules chemisorbed at graphene surfaces. Specifically, the atomic ratio (at.%) of sp^3 C decreases after 30 s while it increases upon 60 to 120 s of hydrogenation, indicating that hydrogenation treatment not only introduces sp^3 C sites but also can remove surface adsorbents like adventitious carbon (defined as a thin layer of hydrocarbon species).

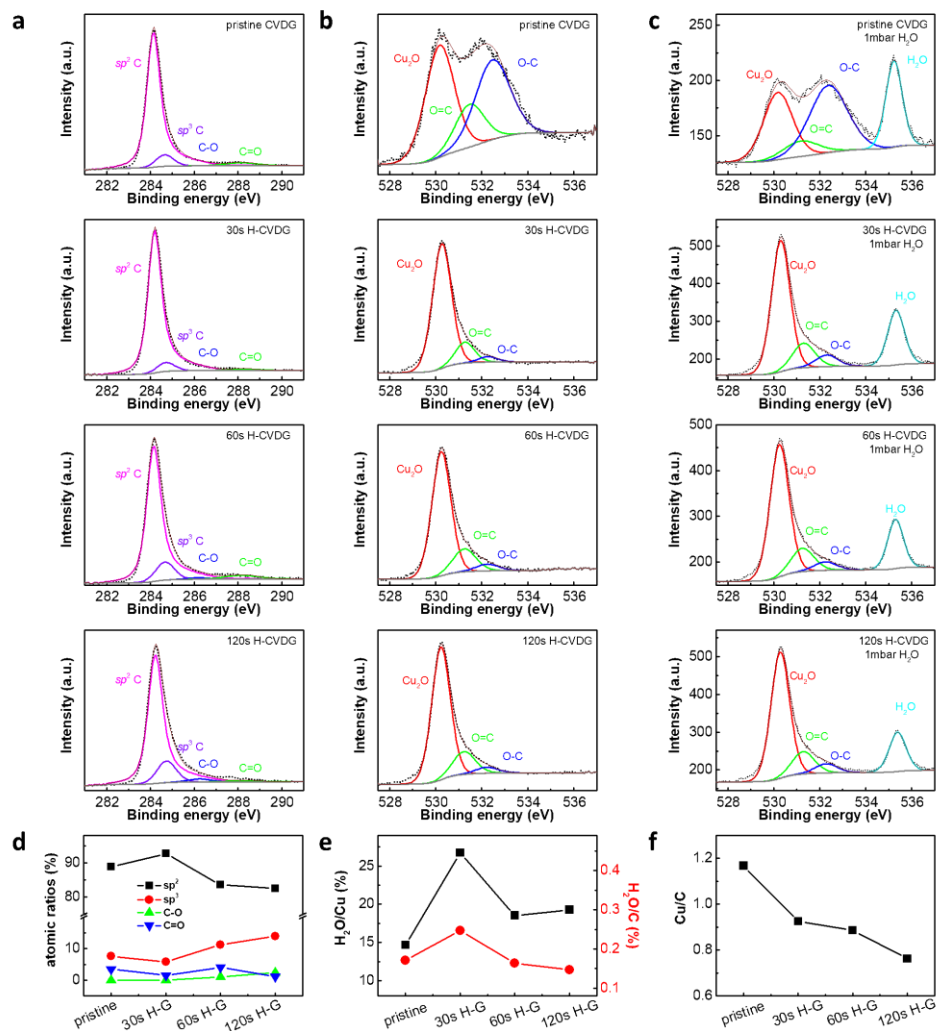


Figure 4.4 Ultra-high vacuum (UHV) and near-ambient pressure (1 mbar H_2O , NAP-) XPS analysis of pristine and hydrogenated CVD graphene (pristine, 30s, 60s, 120s H-CVDG). a) High-resolution carbon (C) 1s spectra in UHV. b) High-resolution oxygen (O) 1s spectra in UHV. c) High-resolution O 1s spectra in the presence of 1 mbar of H_2O . d) Atomic ratios of C 1s in UHV. 'Pristine' represents for pristine graphene without hydrogenation after 30, 60, and 120 s of hydrogenation. e) Corresponding atomic ratios of chemisorbed H_2O versus Cu (black) and C (red) obtained from calculating the peak area. f) Ratios of component area of Cu versus peak area of C.

For comparison, the ratios of the component areas of H_2O versus Cu and peak area of C are calculated (Figure 4.4e). The H_2O/Cu ratios are typically higher in H-graphene (H-G, >15 %) when compared to pristine graphene (14.7 %) with 30 s H-G plateaued (26.7 %), suggesting that H-G presents a higher water affinity. On the

other hand, the H₂O/C ratios are higher after 30 s of hydrogenation (from 17.1% to 24.7 %) but lower upon 60 (16.4%) to 120 s (14.7%) of hydrogenation. This observation is consistent with the at.% changes of sp³ C in Figure 4.4d, confirming the reduction of surface adventitious hydrocarbons especially after 30 s of hydrogenation treatment. As hypothesized, hydrogen radicals can first react with surface adsorbed hydrocarbons before reaching the underlying graphene lattice.^[8] To gain more reliable insights, the area ratios of component peaks for Cu and C (calibrated by the corresponding relative sensitivity factor (R.S.F)) are calculated to rule out the influence of adventitious carbon in Figure 4.4f. The gradual decrease of Cu/C ratios points to the fact that hydrogen plasma removes adventitious carbon on graphene which further illustrates the cleaning effects of hydrogenation treatment. In conclusion, hydrogenation of graphene can effectively improve water adsorption, and the highest affinity is found on the surface after a relatively short period (30 s) of hydrogenation treatment.

4.3 Conclusions

Graphene as a two-dimensional surface is prone to be contaminated by airborne hydrocarbons to minimize its surface energy. As confirmed by HRTEM imaging, hydrogenation of graphene can remove partially the adsorbed hydrocarbons without damaging the lattice integrity and crystallinity. Quantitative analysis of TEM images shows that hydrogenated graphene generally presents and keeps a cleaner surface compared to the untreated, pristine samples. Moreover, a water desorption experiment using TPD-IR and XPS characterization in the presence of 1 mbar H₂O further confirmed that graphene adsorbs more water after it has experienced a hydrogenation treatment. In conclusion, hydrogen radicals clean the surface adsorbed hydrocarbons and meanwhile chemically functionalize the underlying graphene lattice from sp² to sp³, resulting in increased water adsorption of H-graphene and thus an anti-fouling effect towards further hydrocarbon contaminations. We therefore believe that cleaning CVD graphene using surface hydrogenation will represent a new standard in device fabrication of graphene sensors, ameliorating the surface chemistry and thus facilitating surface/interface related applications and biosensors.

4.4 References

- [1] a) Y.-C. Lin, C.-C. Lu, C.-H. Yeh, C. Jin, K. Suenaga, P.-W. Chiu, *Nano Lett.* **2011**, 12, 414; b) W. Xie, L.-T. Weng, K. M. Ng, C. K. Chan, C.-M. Chan, *Carbon* **2015**, 94, 740.

- [2] A. Goossens, V. Calado, A. Barreiro, K. Watanabe, T. Taniguchi, L. Vandersypen, *Appl. Phys. Lett.* **2012**, 100, 073110.
- [3] J. Moser, A. Barreiro, A. Bachtold, *Appl. Phys. Lett.* **2007**, 91, 163513.
- [4] W. J. Choi, Y. J. Chung, S. Park, C. S. Yang, Y. K. Lee, K. S. An, Y. S. Lee, J. O. Lee, *Adv. Mater.* **2014**, 26, 637.
- [5] a) D. Ferrah, O. Renault, C. Petit-Etienne, H. Okuno, C. Berne, V. Bouchiat, G. Cunge, *Surf. Interface Anal.* **2016**, 48, 451; b) Y.-D. Lim, D.-Y. Lee, T.-Z. Shen, C.-H. Ra, J.-Y. Choi, W. J. Yoo, *ACS Nano* **2012**, 6, 4410; c) G. Cunge, D. Ferrah, C. Petit-Etienne, A. Davydova, H. Okuno, D. Kalita, V. Bouchiat, O. Renault, *J. Appl. Phys.* **2015**, 118, 123302.
- [6] a) A. Felten, D. McManus, C. Rice, L. Nittler, J.-J. Pireaux, C. Casiraghi, *Appl. Phys. Lett.* **2014**, 105, 183104; b) A. Harpale, M. Panesi, H. B. Chew, *Phys. Rev. B* **2016**, 93, 035416; c) E. Despiau-Pujo, A. Davydova, G. Cunge, D. B. Graves, *Plasma Chem. Plasma Process.* **2016**, 36, 213.
- [7] H. Arjmandi-Tash, H. Sokooti, J. Lin, A. Kloosterman, L. Lima, G. F. Schneider, *arXiv preprint arXiv:1707.07941* **2017**.
- [8] L. Jiang, W. Fu, Y. Y. Birdja, M. T. Koper, G. F. Schneider, *Nat. Commun.* **2018**, 9, 793.
- [9] G. Algara-Siller, O. Lehtinen, A. Turchanin, U. Kaiser, *Appl. Phys. Lett.* **2014**, 104, 153115.
- [10] a) A. N. Patel, M. G. Collignon, M. A. O'Connell, W. O. Hung, K. McKelvey, J. V. Macpherson, P. R. Unwin, *J. Am. Chem. Soc.* **2012**, 134, 20117; b) Z. Li, Y. Wang, A. Kozbial, G. Shenoy, F. Zhou, R. McGinley, P. Ireland, B. Morganstein, A. Kunkel, S. P. Surwade, *Nat. Mater.* **2013**, 12, 925.
- [11] B. R. Matis, J. S. Burgess, F. A. Bulat, A. L. Friedman, B. H. Houston, J. W. Baldwin, *ACS Nano* **2012**, 6, 17.
- [12] Z. Li, A. Kozbial, N. Nioradze, D. Parobek, G. J. Shenoy, M. Salim, S. Amemiya, L. Li, H. Liu, *ACS Nano* **2015**, 10, 349.
- [13] P. Y. Huang, C. S. Ruiz-Vargas, A. M. van der Zande, W. S. Whitney, M. P. Levendorf, J. W. Kevek, S. Garg, J. S. Alden, C. J. Hustedt, Y. Zhu, *Nature* **2011**, 469, 389.

- [14] C. J. Russo, J. A. Golovchenko, *Proc. Natl. Acad. Sci.* **2012**, 109, 5953.
- [15] L. A. Belyaeva, W. Fu, H. Arjmandi-Tash, G. g. F. Schneider, *ACS Cent. Sci.* **2016**, 2, 904.
- [16] V. Kofman, M. Witlox, J. Bouwman, I. Ten Kate, H. Linnartz, *Rev. Sci. Instrum.* **2018**, 89, 053111.

Chapter 5

Graphene mechanics studied by biaxial compression: The effect of sp^3 and vacancy defects

This work studies the mechanics of graphene floating on the surface of water, subject to biaxial compression in a Langmuir-Blodgett (LB) trough. The platform uniquely allows to characterize graphene samples with centimeter-scale lengths, four orders of magnitude larger than commonly probed microscale graphene samples. The full stress-strain diagram of graphene was plotted to identify elastic and plastic deformation regions. The Young's modulus respects a predicted scaling law and falls two orders of magnitude below that for flat graphene. In contrast, the rigidity of graphene against out-of-plane deformations (flexural rigidity) strongly improves in our large samples. These results demonstrate that graphene – in its very natural form – lacks any intrinsic elastic parameters. Functionalization of the graphene lattice affects the mechanics of graphene; particularly the effects of the sp^3 hybridization and crystalline voids are explored. This work elucidates yet-unexplored science of graphene and establish novel applications for this material in mechanical systems.

Part of this chapter was prepared as an article: Hadi Arjmandi-Tash, Hessem Sokooti, Khosrow Shakouri, Lin Jiang, Alexander Kloosterman, Marius Staring, Lia M.C. Lima, and Grégory F. Schneider, manuscript in preparation.

5.1 Introduction

Picturing graphene as a strictly two-dimensional sheet is unrealistic; though dubbed as two-dimensional, the surface of such materials indeed exhibit transverse out-of-plane undulations (the bending modes) with limited amplitudes in addition to the expected in-plane undulations (stretching modes). Both the in-plane and transverse undulations contribute to the total elastic energy. Harmonic approximation provides a fast solution for this energy considering that the dual modes are decoupled. In this approximation, the average amplitude of the transverse undulations scales with L^2 (L : size of the sample) and approaches infinity for large samples.^[1] This result was interpreted as the tendency for crumpling which questioned the existence of graphene for several decades.^[2]

A more realistic solution, however, was achieved considering that the bending and stretching modes are coupled and mutually affect each other (anharmonic approximation). The transverse displacements are now considerably weaker and scale with $L^{1-\eta/2}$ ($\eta = 0.8$), though still larger than the interatomic distances. Indeed the approximation predicts an intrinsic tendency for small amplitude transverse undulations which eventually and thermodynamically stabilizes the material. The undulations are still size-dependent which activate size-dependent elastic properties. Particularly atomistic Monte Carlo (MC) simulations demonstrates that the out-of-plane undulations in anharmonic approximation renormalize the in-plane stiffness of graphene as $\sim L^{-0.325}$ (L : size of the sample).^[3] The effect, however, cannot be experimentally measured using existing standard platforms (e.g. nano-indentation experiments^[4] and graphene nano-resonators^[5] where graphene is subject to tensile loadings. Indeed the tensile strain suppresses the anharmonicity.^[6] The lack of a suitable experimental approach, on the other hand, has limited the knowledge about the performance of graphene under compression.

In fact compressing free-standing graphene is impractical as graphene collapses. Once supported on a rigid substrate, however, the out-of-plane deformations inherited from the corrugations on the surface of the substrate and graphene/substrate interactions affect the experiment.^[7] More importantly, the mechanics of the substrate is involved in the measurements^[8] and decoupling the contributions of graphene and the substrate is complex. Such experiments may lack accuracy also as a result of the lateral slippage of graphene during the experiments.^[9]

Water offers numerous advantages to conduct graphene compression experiments, hardly available with rigid substrates: i) The surface of water is strictly planar and serves as an appropriate substrate for the two-dimensional graphene. ii) The

adhesion energy between hydrophobic graphene and water is lower than graphene on typical substrates^[10] (45 times lower than graphene on silicon), which guarantees a negligible graphene/substrate interaction. In addition, iii) graphene can smoothly slide on the surface of water (no dry friction) which allows free deformation upon compressive buckling. It is important that iv) ultra-pure water is easily accessible; the uniform and simple chemistry of the water substrate is not a source of irreproducibility, demonstrating that it is now possible to probe still unexplored properties of graphene.

5.2 Results

5.2.1 Compression of graphene floating on water

The study was performed on a LB trough, capable of applying a precisely controlled two dimensional pressure on graphene under test while freely floating at air/water interface.^[11] A piece of $\sim 1 \times 1 \text{ cm}^2$ crack-free graphene,^[12] chemically grown on a copper foil,^[13] was placed on the surface of an ammonium persulfate solution (0.5 M) on the trough and surrounded with Dipalmitoylphosphatidylcholine (DPPC) (see Figure AIV. 1 and Appendix IV. 2). Once the copper foil etches away, graphene was freely floating at the air/liquid interface. Unlike the compression of graphene embedded in polymeric materials where the placement of graphene or curing the supporting polymer deposit a residual strain (which adds complexity to the analysis),^[9a] graphene in our experiments can relax to release any strain (e.g. due to the growth) before initiating the measurements.

Moving two slightly-wetted solid barriers—initially positioned at opposite sides of the trough—forward (closer to each other) lowers the accessible area which eventually applies a two-dimensional surface pressure p (referred to as stress) to graphene (Figure 5.1a). The role of the lipid molecules is to form a stable, two-dimensional and dynamic self-assembled layer at the air/liquid interface in contact with graphene ensuring a strictly lateral compression (no perpendicular component) of graphene. The two-dimensional strain ($\epsilon_{||} = (A_0 - A)/A_0$, A_0 : initial area of graphene, A : area of graphene at the time of the measurement) of the graphene was estimated by processing high resolution images taken by a camera focusing on graphene (see Methods in AIV).

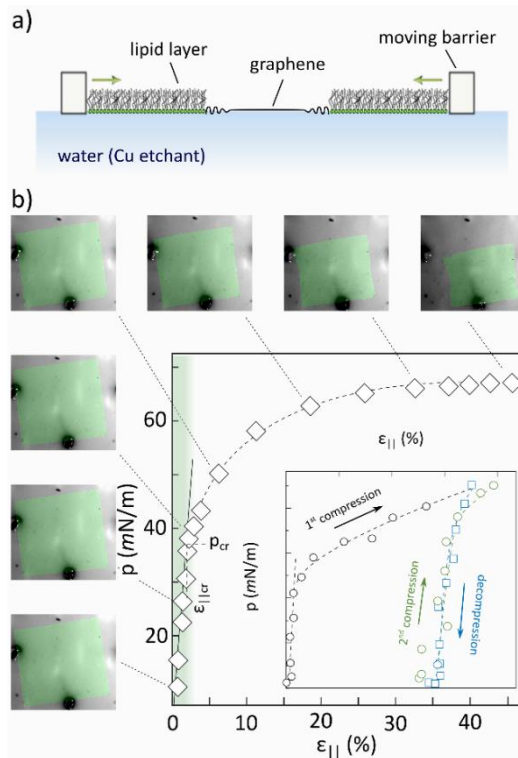


Figure 5.1 Floating graphene subject to 2D compression. a) Schematic representation of the experimental set-up: graphene floating on the surface of a copper etchant (0.5 M ammonium persulfate) is subject to a compressive stress applied by surrounding lipids and moving barriers. b) Stress-strain relation of a floating graphene piece ($\sim 1 \times 1 \text{ cm}^2$): The green shaded area in the main plot corresponds to the elastic deformation region with the solid line as the linear fit. Few snapshots of the graphene (colored in green) at different compression stages are presented at the left and top margins, featuring progressive deformations upon compression. Inset panel corresponds to the subsequent compression (black)/decompression (blue)/compression (green) of a separate graphene sheet. The horizontal displacement between the first and second compression strokes corresponds to the permanent plastic deformation. The barrier displacement rate was limited to 1 mm/min in these experiments.

Figure 5.1b shows the stress-strain curve of a selected graphene sample. Similar to conventional materials, graphene exhibits an elastic deformation (linear stress-strain relation) up to a certain level (critical stress p_{cr}); Then plastic deformation, characterized by the buckling of graphene, starts. Unlike elastic deformation which is reversible, plastic deformation is permanent: removing the external pressure, does not return graphene to its original shape (inset Figure 5.1b). Bulk modulus (k) in biaxial loading measures the resistance of the material against elastic deformation: $p = k\varepsilon_{||}$ and scales with the two dimensional Young's modulus (E_{2D}) as: $k =$

$E_{2D}/2(1 - \nu)$ where $\nu = 0.25$ is the Poisson's ratio of the graphene estimated for large samples.^[3]

5.2.2 The introduction of lattice defects

sp^3 hybridization of carbon orbitals (as a result of reaction with various chemical components) and vacancy defects (generated by shooting-out carbon atoms in momentum transfer processes) are the two major defect types commonly observed in graphene lattice. The mechanics of graphene in the presence of such defects was characterized. Hydrogenation of graphene and argon bombardment of the lattice in a plasma chamber respectively achieved sp^3 hybridization and vacancy defects. Manipulation of the lattice affects the mechanics of graphene. Inclusion of the crystalline defects upon exposing the graphene samples to argon and hydrogen plasmas modify the mechanics of graphene. The defect density n_D can be estimated using the relative intensities of the Raman D and G peaks^[14]:

$$n_D [cm^{-2}] = (7.3 \pm 2.2) \times 10^9 E_L^4 (I_D/I_G) \quad (1)$$

In this relation $E_L = 2.33$ eV is the excitation energy. Figure 5.2 shows the Raman spectra and defect density characterization for samples treated by argon (a-b) and hydrogen plasma (c-d). Note that the intercept of the polynomial fitting of the time dependent defect density gives $n_0 = 9 \times 10^{10} cm^{-2}$ for untreated graphene samples. Energetic Ar^+ ions in plasma bombardment of graphene are capable to effectively knock-out carbon atoms from the lattice and generate vacancy defects of atomic sizes.^[15] In contrast, hydrogen radicals are chemically active and form covalent bonds to carbon atoms, altering their hybridization state from sp^2 to sp^3 .^[16]

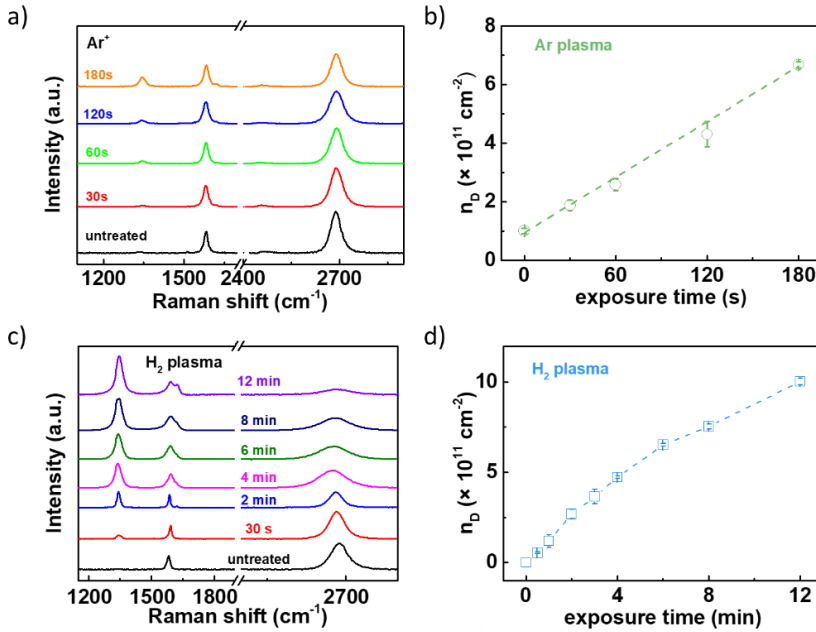


Figure 5.2 Raman characterization and mechanics of functionalized graphene samples. a) Typical Raman spectra recorded on graphene samples exposed to Ar plasma for different durations. b) Density of the vacancy defects (n_D) calculated for different samples in (a). c) Typical Raman spectra recorded on graphene samples exposed to H₂ plasma for different durations. d) Density of the sp^3 hybridization defects calculated for different samples in (c). All the Raman spectra were recorded on graphene/silica wafers, using an excitation source of $\lambda = 532 \text{ nm}$.

5.2.3 Elastic properties of compressed graphene

It is commonly said that pristine graphene, possessing strong bonds between the carbon atoms, is one of the most stiff materials (few hundred times stiffer than steel^[4a]) featuring a Young's modulus of $E_{2D}^{flat} \sim 336 \text{ N/m}$.^[17] Such a statement has to be used with care as its validity is limited to graphene samples that are free from out-of-plane perturbations (flat graphene). Indeed tensile loading of the samples, as the standard procedure to probe the stiffness of graphene so far,^[4-5] inevitably flattens graphene and suppress anharmonicity.^[6, 18] Our approach is the only existing method so far which measures the stiffness of graphene while the natural perturbations remain untouched. The median Young's moduli of our twenty monolayer graphene samples approaches $\bar{E}_{2D} = 2.6 \text{ N m}^{-1}$ ($k = 1.7 \text{ N m}^{-1}$) (Figure 5.3a). Remarkably, this value is two orders of magnitude smaller than E_{2D}^{flat} but can be well-explained in the framework of the scaling effect in the presence of the anharmonicity (Figure 5.3b and Appendix IV. 3): Indeed for large samples, the lower energy costs of out of plane fluctuations ($\propto q^2$, q : the wave vector) compared to in-plane ones ($\propto q$) favors the

long wavelength out-of-plane fluctuations and increases the contribution of the anharmonic energy correction terms in total elastic energy. The size dependency of the energy terms causes a size dependent stiffness which falls in large samples. Interestingly the stiffness of our centimeter-scale samples falls on the extrapolation and respects the same scaling law of the samples of few (tens of) nanometer size (\sim six orders of magnitude smaller in size, \sim twelve orders of magnitude larger in area, more relevant for 2D compression) and validates the accuracy of those modelling.

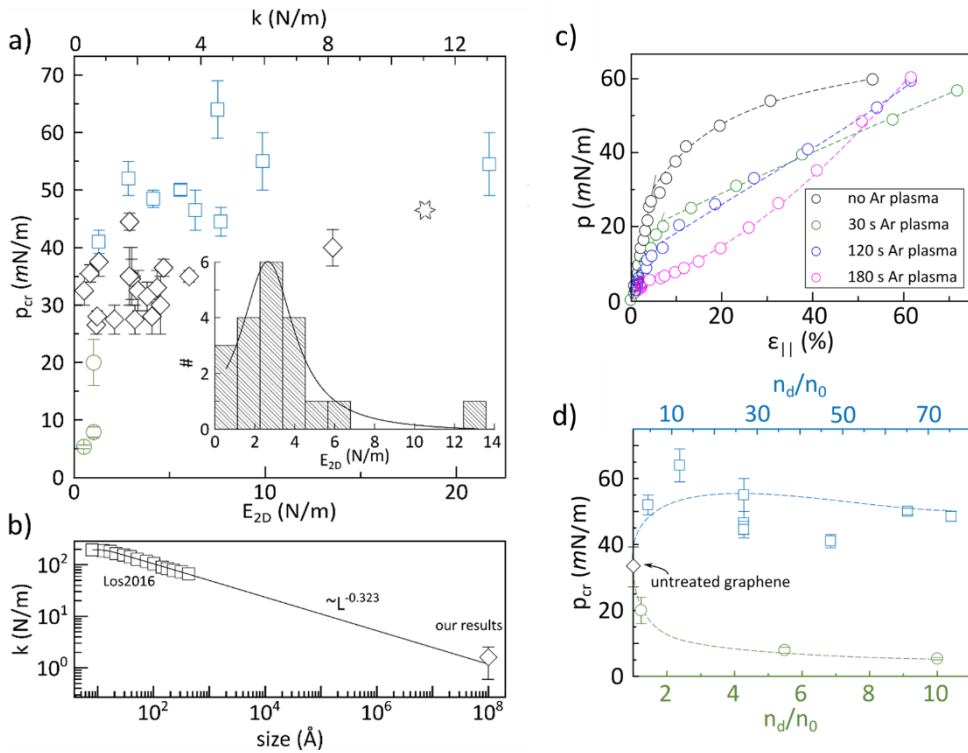


Figure 5.3 Elastic properties of graphene subject to 2D compression. a) Correlation of the yield strength and in-plane stiffness of untreated (monolayer: black diamonds, bilayer: black star), hydrogenated (blue squares), Ar⁺ bombarded (green circles) graphene. The inset displays the distribution of the E_{2D} of untreated monolayer graphene samples, centered at 2.6 N m⁻¹ with the FWHM of 3.2 N m⁻¹ estimated by Lorentzian fitting (solid line). b) Superimposition our experimentally measured bulk moduli (untreated graphene) with the simulation results of nanoscale samples, by Los et al.^[3]: the solid line corresponds to the scaling law reported by the same group (Appendix IV. 3). c) Stress-strain plots of graphene samples subject to Ar ion bombardment of different durations. d) Critical pressure of hydrogenated and Ar ion bombarded graphene samples: the density of the defects (n_D) achieved by the Raman spectroscopy is normalized by the defect density of untreated graphene ($n_0 \sim 9 \times 10^9$ cm⁻²). The p_{cr} of untreated graphene is the median of all the measured samples detailed in Figure 1 of the main text. All the dashed lines are guides to the eyes.

Further characterization of the mechanics of graphene in the presence of such defects was conducted. Figure 5.3c details the stress-strain plots of graphene samples subject to Ar^+ bombardments of up to 180 s. Reduction of the p_{cr} at the cross-over between linear (elastic) and non-linear (plastic) deformations upon increasing the vacancy density is visible directly in the plots. Even after 180 s of plasma treatment, the relative concentration of the vacancies ($\sim 6 \times 10^{10} \text{ cm}^{-2}$) to the concentration of the carbon atoms in graphene lattice ($3.82 \times 10^{15} \text{ cm}^{-2}$) is negligible; hence the treatment is not expected to (and does not) affect the rigidity as it originates from the degree of order and the strength of the bonds between the atoms.^[9a] In contrast, hydrogenation of graphene increases the p_{cr} (Figure 5.3d). Such an effect is attributed to the increased interaction between hydrogenated graphene lattice and water substrate (e.g. hydrogen bonds) which improves the in-plane Young's modulus upon partial screening of long wavelength flexural modes. It seems increasing the dose of the sp^3 defects ultimately (and gradually) tends to weaken the lattice.^[19]

The inclusion of sp^3 defects (achieved by hydrogenation of the graphene lattice) considerably improves p_{cr} . Non-covalent graphene/substrate interaction has been observed to delay buckling by preventing the delamination of graphene from polymeric substrates.^[7a, 9a] In a similar scenario, one could attribute the increase of p_{cr} to the apparition of hydrogen bonds between hydrogenated graphene and water in our system. In Appendix IV. 4 and 5, however, it is theoretically illustrated that water conforms graphene during the buckling and no delamination is involved. In fact, the increment in p_{cr} in hydrogenated graphene is a result of the improved Young's modulus, discussed below.

5.2.4 Correlation of strain and stiffness in graphene

Figure 5.4a shows the $\varepsilon_{|\text{cr}} (\approx \varepsilon_{|\text{cr}}/2)$ of different samples as a function of the stiffness. Untreated and hydrogenated samples respect the classical Eulerian picture of buckling^[7a] and exhibit $\varepsilon_{|\text{cr}} \propto 1/E_{2\text{D}}$ behaviour. This trend is not observable with the Ar^+ bombarded samples. Notably, the hydrogenation of graphene improves the Young's modulus by $\beta = 1.5$ times, matching with the improvement in p_{cr} discussed in Figure 5.3a. In the framework of the anharmonic coupling the stretching and flexural modes in 2D materials and similar to an earlier observation,^[4e] the improvement is attributed to the partial screening and eventual localization of the long wavelength flexural modes by sp^3 defects in hydrogenated graphene (Figure 5.4b). Particularly the improvement factor β is reasonably close to $(n_{\text{D}}/n_0)^{\eta/2}$ ($\eta = 0.36$) predicting 1.3 to 2.3 times improvement in Young's modulus.^[4e] Our molecular dynamics simulations also confirms that the flexural modes are affected by hydrogenated sites,

leading to a 1.35 times improvement in Young's modulus, matching well with the experimental measurement (Figure AIV. 2b and c).

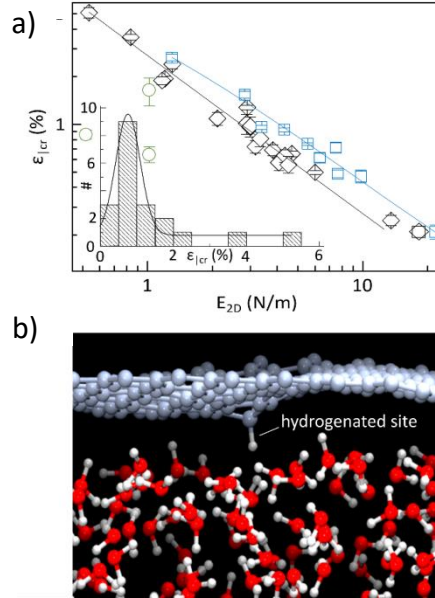


Figure 5.4 Correlation of the strain and stiffness in graphene. a) Correlation of the critical one-dimensional strain $\varepsilon_{|cr}$ ($\approx \varepsilon_{||cr}/2$) and in-plane stiffness of untreated (monolayer: black diamonds, bilayer: black star), hydrogenated (blue squares), Ar^+ bombarded (green circles) graphene; the solid lines correspond to the best fittings with $\varepsilon_{|cr} = \frac{\alpha}{(E_{2D}/\beta)}$ revealing $\alpha = 0.027 \text{ N m}^{-1}$ and $\beta = 1$ for untreated and $\alpha = 0.027 \text{ N m}^{-1}$ and $\beta = 1.4$ for hydrogenated graphene. Inset shows the distribution of the $\varepsilon_{|cr}$ of untreated monolayer graphene, centred at 0.8%. b) Molecular dynamics simulation of hydrogenated graphene on the surface of water: interaction between the hydrogenated site and water molecules locally stabilizes the corresponding carbon atom. The snapshot corresponds to $\varepsilon < \varepsilon_{cr}$ region.

In the classical Eulerian picture of buckling, the coefficient α (see the fitting in Figure 5.4a) depends on the flexural rigidity D of the specimen. In Appendix IV. 6 and by analyzing the buckling patterns, D is estimated to be in the order of 10^{-12} N m (10^6 eV). The value for our centimeter-scale samples is at least three orders of magnitude larger than the previous report for micro-sized graphene samples^[20] which itself is three to four orders of magnitude larger than for flat graphene. The trend agrees with the predicted scaling properties of flexible membranes.^[21] Our observations of scaling both the Young's modulus and flexural rigidity demonstrates that graphene, in its natural form, lacks any intrinsic elastic coefficients.

Inset in Figure 5.4a plots the distribution of the critical strain of untreated graphene samples. Interestingly, the median critical strain ($\bar{\epsilon}_{\text{cr}} = 0.8\%$) in our centimetre-scale samples ($L/t \sim 10^8$) approaches that of narrow (micro-sized) graphene samples sandwiched in between polymeric supports;^[7a] exhibiting such a large strain before buckling is attributed to the strictly 2D surface of water which excludes any substrate-induced out-of-plane deformations as buckling promoters.

5.3 Conclusion

Graphene floating on water remains in its natural form and now unlocked a versatile and easily accessible platform to study the mechanics of graphene, disclosing astonishing size-dependent in-plane and flexural rigidities. Particularly the Young's modulus of centimeter-scale graphene falls two-orders of magnitude below that in micrometer sized sheets, commonly measured earlier; The finding correct the regard to graphene as the strongest material ever measured. Chemical alteration of the graphene lattice remarkably affects the mechanics of the sheet. Particularly the inclusion of vacancy defects leads to a catastrophic failure in-which a negligible surface pressure causes graphene to collapse. Hydrogenation, however, locally stabilizes graphene on water leading to an improved in-plane stiffness. Compressing graphene floating on water, per se, provides new horizons both in science and application of graphene: piezoelectricity, surface chemistry, mechanics, material science, sensors, to name a few.

5.4 References

- [1] A. Fasolino, J. H. Los, M. I. Katsnelson, *Nat. Mater.* **2007**, 6, 858.
- [2] A. K. Geim, K. S. Novoselov, *Nat. Mater.* **2007**, 6, 183.
- [3] J. H. Los, A. Fasolino, M. I. Katsnelson, *Phys. Rev. Lett.* **2016**, 116, 015901.
- [4] a) C. Lee, X. Wei, J. W. Kysar, J. Hone, *Science* **2008**, 321, 385; b) G.-H. Lee, R. C. Cooper, S. J. An, S. Lee, A. van der Zande, N. Petrone, A. G. Hammerberg, C. Lee, B. Crawford, W. Oliver, J. W. Kysar, J. Hone, *Science* **2013**, 340, 1073; c) A. Zandiatashbar, G.-H. Lee, S. J. An, S. Lee, N. Mathew, M. Terrones, T. Hayashi, C. R. Picu, J. Hone, N. Koratkar, *Nat. Commun.* **2014**, 5, 3186; d) G. López-Polín, J. Gómez-Herrero, C. Gómez-Navarro, *Nano Lett.* **2015**, 15, 2050; e) G. López-Polín, C. Gómez-Navarro, V. Parente, F. Guinea, Mikhail I. Katsnelson, F. Pérez-Murano, J. Gómez-Herrero, *Nat. Phys.* **2014**, 11, 26.

- [5] a) C. Chen, S. Rosenblatt, K. I. Bolotin, W. Kalb, P. Kim, I. Kymissis, H. L. Stormer, T. F. Heinz, J. Hone, *Nat. Nanotechnol.* **2009**, 4, 861; b) V. Singh, S. Sengupta, H. S. Solanki, R. Dhall, A. Allain, S. Dhara, P. Pant, M. M. Deshmukh, *Nanotechnology* **2010**, 21, 165204; c) A. M. v. d. Zande, R. A. Barton, J. S. Alden, C. S. Ruiz-Vargas, W. S. Whitney, P. H. Q. Pham, J. Park, J. M. Parpia, H. G. Craighead, P. L. McEuen, *Nano Lett.* **2010**, 10, 4869.
- [6] R. Roldán, A. Fasolino, K. V. Zakharchenko, M. I. Katsnelson, *Phys. Rev. B* **2011**, 83, 174104.
- [7] a) O. Frank, G. Tsoukleri, J. Parthenios, K. Papagelis, I. Riaz, R. Jalil, K. S. Novoselov, C. Galiotis, *ACS Nano* **2010**, 4, 3131; b) Z. H. Aitken, R. Huang, *J. Appl. Phys.* **2010**, 107, 123531.
- [8] H. Conley, N. V. Lavrik, D. Prasai, K. I. Bolotin, *Nano Lett.* **2011**, 11, 4748.
- [9] a) G. Tsoukleri, J. Parthenios, K. Papagelis, R. Jalil, A. C. Ferrari, A. K. Geim, K. S. Novoselov, C. Galiotis, *Small* **2009**, 5, 2397; b) T. Jiang, R. Huang, Y. Zhu, *Adv. Funct. Mater.* **2014**, 24, 396.
- [10] J. Driskill, D. Vanzo, D. Bratko, A. Luzar, *J. Chem. Phys.* **2014**, 141, 18C517.
- [11] P. Cicuta, D. Vella, *Phys. Rev. Lett.* **2009**, 102, 138302.
- [12] H. Arjmandi-Tash, L. Jiang, G. F. Schneider, *Carbon* **2017**, 118, 556.
- [13] H. Arjmandi-Tash, N. Lebedev, P. M. G. van Deursen, J. Aarts, G. F. Schneider, *Carbon* **2017**, 118, 438.
- [14] L. G. Cançado, A. Jorio, E. M. Ferreira, F. Stavale, C. Achete, R. Capaz, M. Moutinho, A. Lombardo, T. Kulmala, A. C. Ferrari, *Nano Lett.* **2011**, 11, 3190.
- [15] A. Eckmann, A. Felten, A. Mishchenko, L. Britnell, R. Krupke, K. S. Novoselov, C. Casiraghi, *Nano Lett.* **2012**, 12, 3925.
- [16] J.-H. Zhong, J. Zhang, X. Jin, J.-Y. Liu, Q. Li, M.-H. Li, W. Cai, D.-Y. Wu, D. Zhan, B. Ren, *J. Am. Chem. Soc.* **2014**, 136, 16609.
- [17] a) L. Pocivavsek, R. Dellsy, A. Kern, S. Johnson, B. Lin, K. Y. C. Lee, E. Cerda, *Science* **2008**, 320, 912; b) Y. Li, D. Datta, Z. Li, *Carbon* **2015**, 90, 234; c) M. M. Shokrieh, R. Rafiee, *Mater. Des.* **2010**, 31, 790; d) R. J. Young, I. A. Kinloch, L. Gong, K. S. Novoselov, *Compos. Sci. Technol.* **2012**, 72, 1459.

- [18] J. H. Los, A. Fasolino, M. I. Katsnelson, *NPJ 2D Mater. Appl.* **2017**, 1, 9.
- [19] G. López-Polín, C. Gómez-Navarro, V. Parente, F. Guinea, M. I. Katsnelson, F. Perez-Murano, J. Gómez-Herrero, *Nat. Phys.* **2015**, 11, 26.
- [20] M. K. Blees, A. W. Barnard, P. A. Rose, S. P. Roberts, K. L. McGill, P. Y. Huang, A. R. Ruyack, J. W. Kevek, B. Kobrin, D. A. Muller, P. L. McEuen, *Nature* **2015**, 524, 204.
- [21] J. H. Los, M. I. Katsnelson, O. V. Yazyev, K. V. Zakharchenko, A. Fasolino, *Phys. Rev. B* **2009**, 80, 121405.

Chapter 6

Hydrogenated and nitrogenated graphene for field effect gas sensing

This work reports the sensing responses of hydrogenated and nitrogenated graphene field effect transistors to various gas species including ethylene, carbon monoxide and ethanol. The two graphene devices are compared in terms of electrical properties and sensing performance corresponding to the surface functionalization. Superior to the responses of pristine graphene, hydrogenated graphene with more positive doping effect shows a higher sensitivity than nitrogenated graphene. The comparable responses to different gas on each device suggest a low selectivity of the functionalized graphene. Importantly, the real-time responses for hydrogenated graphene show a positive correlation with increased concentrations of ethylene. In contrast, the responses of nitrogenated graphene exhibit minimal or even decreased dependency to increased gas concentrations. Higher levels of nitrogen doping further decrease the sensitivity due to the doping transition from p-type to n-type. Therefore, chemical functionalization governs the sensitivity of graphene to a range of gas depending on changing the doping effect and adsorption affinity.

6.1 Introduction

Graphene, a single layer of sp^2 hybridized carbon atoms,^[1] has been considered as an ideal sensing platform due to its large surface-to-volume ratio, being sensitive to surroundings and low electrical noises.^[2] Especially, graphene field effect transistors (GFETs) utilizing the conductivity/resistivity responses can sensitively detect gas species down to single-molecules.^[3] However, the absence of dangling bonds and the chemical inertness of the basal plane limit the detection sensitivity and selectivity of GFETs. As a result, the chemical modifications of the graphene surface have been extensively developed to improve the sensing performance of sensing devices.^[4] For example, hydrogenation (Chapter 2) and nitrogeneration (Chapter 3) have been conducted to not only introduce chemical defects and charge doping into the lattice, but also enhance the chemical and electrochemical reactivity of graphene.^[5] In this chapter, we systematically investigated whether hydrogenation and nitrogeneration by doping and defect generation could improve or modify the sensing performance of GFET devices.

Here, the field effect detection of ethylene, carbon monoxide and ethanol was explored at hydrogenated and nitrogenated graphene, referred as HG and NG. For that, hydrogen and ammonia plasmas were used to chemically functionalize the graphene. With a similar defect density, p-doped HG and NG showed improved responses to the tested gas compared to pristine graphene. The influence of the electron mobility and of charge doping on the sensing performance were investigated in details. A lower electron mobility was not found to limit the highest sensitivity of HG. Nitrogeneration (exposure time longer than 10 s) formed n-doped NG with decreased sensitivity compared to the p-doped NG containing lower levels of nitrogeneration. Surface ageing induced p-doping and enhanced sensitivity. In contrast to NG, the real-time responses of HG exhibited a positive correlation to the increasing concentration of ethylene. The responses to carbon monoxide and ethanol for both HG and NG showed no correlations to the measured concentrations.

6.2 Results

6.2.1 Raman characterization of graphene

Raman spectroscopy was performed to characterize the defect density and nature of chemical vapor deposition (CVD) graphene supported on a silicon wafer upon hydrogenation and nitrogeneration treatments. The Raman spectra of pristine graphene in Figure 6.1a is characterized by two peaks, the G peak (1584 cm^{-1}) and the 2D peak (2681 cm^{-1}). In addition to the sharp and single-Lorentz fitted 2D peak, the intensity ratio $I(2D)/I(G)$ (~ 2) and no visible D peak ($\sim 1350\text{ cm}^{-1}$) indicate the monolayer nature of graphene with a negligible intrinsic defect density. After a

hydrogen plasma treatment of 30 s to 60 s, a D peak and D' peak ($\sim 1620\text{ cm}^{-1}$) appeared due to the activation of H- sp^3 defects.^[6] Similarly, ammonia plasma treatments from 10 s to 60 s also introduced nitrogenated defects and thus D and D' defect peaks (Figure 6.1b).

The intensity ratio $I(D)/I(G)$ is an indicator of the defect density in HG and NG.^[7] Compared to hydrogenation, nitrogenation introduced more defects into the graphene lattice with a $I(D)/I(G)$ ratio for NG larger than for HG (Figure 6.1c). Moreover, the ratios of $I(D)/I(D')$ in Figure 6.1d also suggest different defect nature for hydrogenated (~ 10 , sp^3 type) and nitrogenated (~ 6 , vacancy-like type) graphene.^[8] As 30 s hydrogenation and 10 s of nitrogenation give rise to the similar defect density in graphene, their electrical properties and sensing performance were compared.

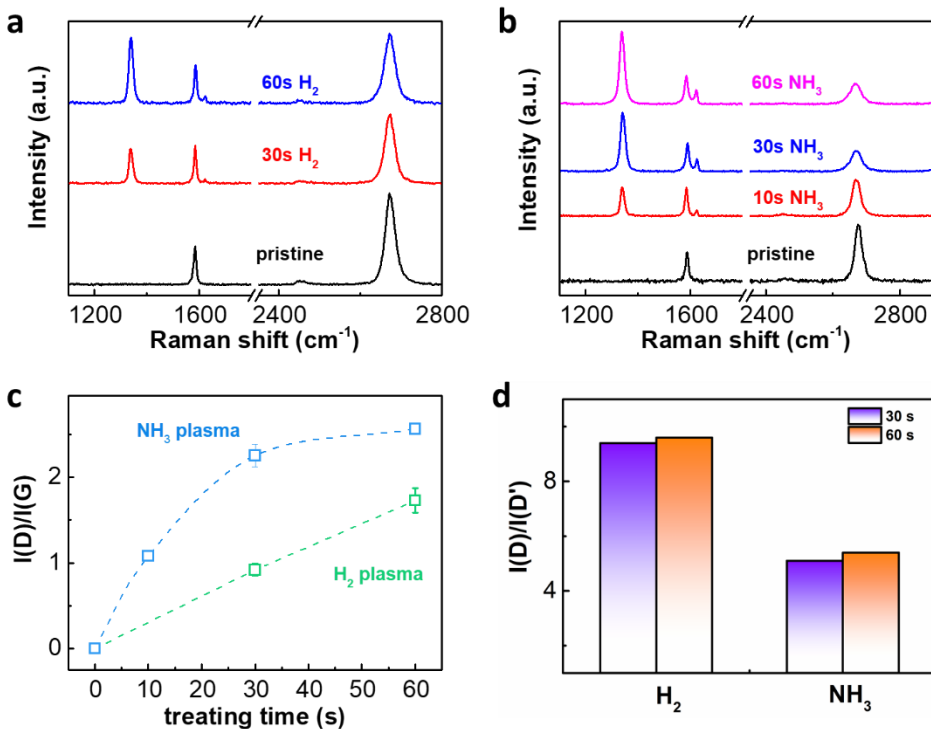


Figure 6.1 Raman characterization of HG and NG. a) Raman spectra of pristine graphene and graphene after 30 s and 60 s of hydrogen plasma treatment. b) Raman spectra of graphene after 0 s (pristine), 10 s, 30 s and 60 s of ammonia plasma. c) Intensity ratio $I(D)/I(G)$ of graphene (a reflection of defect density) versus the treating times for HG and NG. d) $I(D)/I(D')$ ratios of 30 s to 60 s of HG and NG.

6.2.2 The impact of electron mobility on the sensing performance

Graphene field effect transistor (GFET) devices were fabricated using polymer-assisted transfer. In details, chemical vapor deposition (CVD) graphene supported by the as-grown copper foil was spin-coated with a 400 nm thin layer of PMMA (poly(methyl methacrylate)).^[9] After the copper was etched using an aqueous solution of ammonium persulfate (0.5 M), the graphene-PMMA assembly was then rinsed with ultra-pure water to remove any residues from the etchant. Finally a hydrophilic and clean silicon wafer (with a 285 nm-thick silicon dioxide layer on top) was used as a substrate of the graphene/PMMA assembly. Then the dried sample was immersed in acetone to remove PMMA and to expose the graphene surface. Source and drain electrodes (5 nm Cr/50 nm Au) were further deposited on top of graphene to ensure good and stable contacts with minimized contact resistance.

The resistance (R) of graphene was measured at gate voltages (V_g) in a back gated device configuration. The resistance-voltage (R - V_g) curves for 30 s HG and 10 s NG are plotted in Figure 6.2a. Owing to the p-doping effect from the trapped states at the substrate-graphene interface, pristine graphene intrinsically exhibits a positive charge neutrality point (CNP) of around 40 V. In contrast, positive CNP shifts compared to the pristine graphene were obtained for both HG (~ 110 V) and NG (~ 40 V). According to the discussion in Chapter 2 and 3, the p-doping effect for HG is mainly caused by the water adsorption^[10] while for NG p-doping is primarily caused by the presence of pyridinic nitrogen dopants.^[11] Subsequently, the mobility of different graphene samples were compared and plotted in Figure 6.2b. For pristine graphene, the hole carrier mobility is as high as ~ 1000 cm² V⁻¹ s⁻¹, suggesting the high quality of the CVD graphene. In comparison, 10 s NG shows a slightly decreased mobility while 30s HG shows a much decreased mobility of ~ 500 cm² V⁻¹ s⁻¹. As the carrier mobility of graphene is prone to charge scattering,^[12] the reduced mobility of HG was mainly ascribed to the hybridization change and induced short-range scatterings in the lattice.^[10, 13]

The sensing responses of graphene towards ethylene (0.1 ppm), carbon monoxide (0.01 ppm) and ethanol (1 ppm) were recorded in terms of the effective gate shifts, which are directly correlated to the graphene conductance using the transconductance.^[3a] Superior to the responses on a pristine graphene, the 30 s HG shows larger shifts than 10 s NG, presumably because of a higher affinity of HG towards the adsorption of gas. Such a superiority of HG to NG is found to be coincident with the more positive p-doping effect as shown in Figure 6.1a. Separately, each type of GFET devices shows comparable responses between ethylene, carbon monoxide and ethanol within the tested concentrations, indicating a low selectivity to

any of the three gas. Therefore, hydrogenated and nitrogenated defects in graphene can enhance the sensitivity rather than the selectivity to gas detection. Separately, p-doping is favorable to the non-selective gas adsorption at the surface of graphene. More importantly, the mobility of graphene is not ruling the sensing sensitivity of graphene devices.

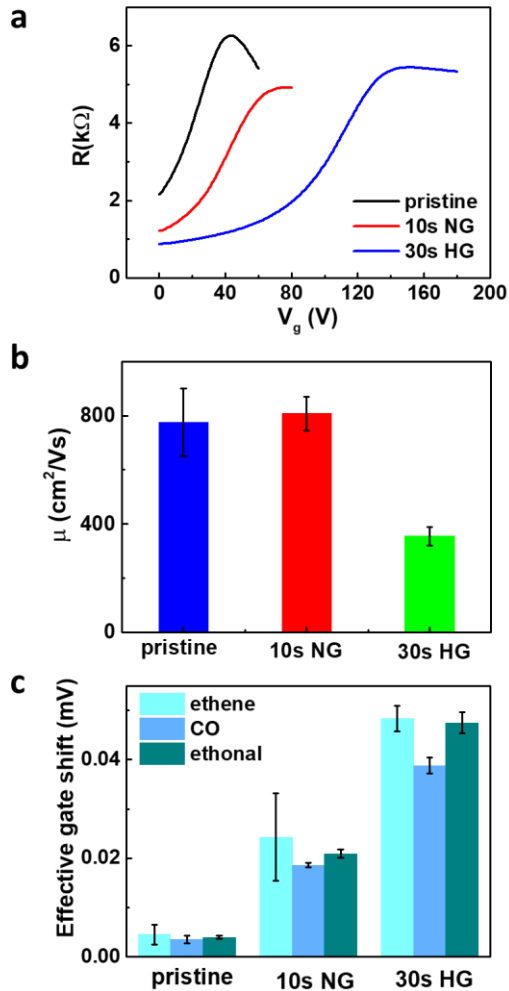


Figure 6.2 Comparison of transport properties and sensing performance for HG and NG. a) Resistance (R)-gate voltage (V_g) curves of pristine graphene, 30 s HG and 10 s NG. b) Comparison of graphene mobilities for pristine graphene, 30 s HG and 10 s NG. c) Effective gate shifts for pristine graphene, 30 s HG and 10 s NG following the exposure of the GFET devices to 0.1 ppm ethylene, 0.01 ppm carbon monoxide and to 1 ppm ethanol.

6.2.3 Real-time sensing responses

To further investigate the sensing performance, the resistance changes for 30 s HG and 10 s NG as a function of gas exposure time were compared (Figure 6.3). In Figure AV. 1, the graphene sheet resistance shows a time dependent drift of the baseline at the applied V_g of 0 V and constant exposure to technical air (free of water). After several seconds in presence of 0.1 ppm ethylene, sharp spikes appear due to the disturbance of the surface equilibrium following the introduction of gas molecules. Upon continuous exposure to ethylene, the resistance shows a staircase-like drop, which is caused by the adsorption of ethylene and the induced charge transfer to graphene.^[14] The newly formed baseline indicates that the gas adsorption reaches an equilibrium. Finally flushing technical air leads to the desorption of ethylene from the graphene surface with the resistance of the device returning to its original equilibrium and baseline.

Figure 6.3a-c shows the resistance responses of the GFETs devices to the increasing concentrations of ethylene (0.1, 0.2, 0.5 ppm), carbon monoxide (0.01, 0.02, 0.05 ppm) and ethanol (1, 2, 5, 10 ppm) in sequence. The detection to each concentration is duplicate. The average responses of HG and NG are summarized in Figure 6.4d. In general, HG shows more sensitive responses than NG to the measured concentrations of all the three gas, which is consistent with the results obtained in Figure 6.2c. For detection of ethylene within the range of measured concentrations, the responses at 30 s HG shows an monotonic increasing dependency. For continuous detection of carbon monoxide, HG starts to show saturated responses when the concentration increases from 0.02 ppm to 0.05 ppm. After the saturation, the responses even decrease upon increasing concentrations of ethanol. In comparison, NG shows saturated responses to ethylene detection at concentrations from 0.1 to 0.2 ppm, followed by a decreasing trend of responses to increased concentrations of carbon monoxide and ethanol detection. The saturation trend after several times of detection can be attributed to that the limited active sites on the graphene surface are occupied by the trapped gas molecules. More detections induce more trapping and thus further reduce the available sites for valid gas adsorption to generate corresponding responses. As a consequence, NG is expected to have less active sites and thus be more prone to give saturated responses than HG.

Furthermore, the adsorption transient behaviors of the GFETs upon the exposure of different concentrations of ethylene gas molecules is summarized in Table 1. The adsorption transient parameter is defined as the resistance change ΔR vs the time required for the signal to reach the new baseline Δt , $\Delta(\Delta R/\Delta t)$. It is shown that upon the increase of ethylene concentrations, the transient parameter increases while

adsorption time decreases for both GFETs. Given the similar adsorption times between two types of GFETs, the higher values of adsorption transient parameters on HG than NG also reflect the more excellent sensing responses of HG in comparison with NG.

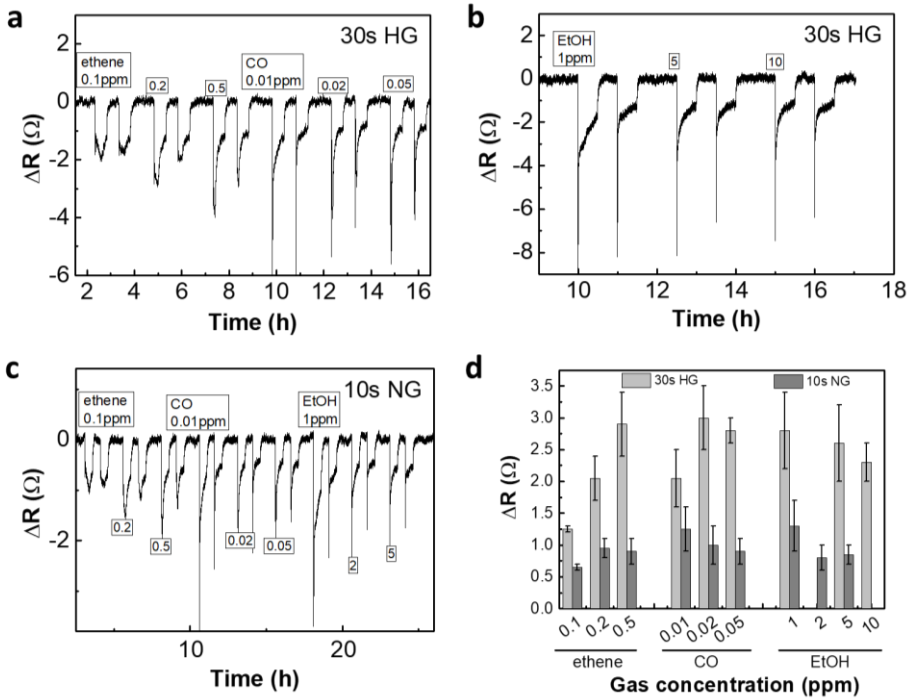


Figure 6.3 Real-time responses for HG and NG. a) Responses of 30 HG to ethylene (0.1, 0.2, 0.5 ppm) and CO (0.01, 0.02, 0.05 ppm). b) Responses of 30 s HG to EtOH (1, 5, 10 ppm). Each gas injection repeated once. c) Responses of 10 s NG to the exposure of ethylene (0.1, 0.2, 0.5 ppm), CO (0.01, 0.02, 0.05 ppm) and EtOH (1, 2, 5 ppm). Each gas injection was duplicated. d) Average resistivity responses for 30 s of HG and 10 s of NG for different gas. All the measurements were done at room temperature.

Table 1 Adsorption transient parameter and adsorption time for different concentrations of ethylene on GFETs

GFETs	Gas concentration (ppm)	$\Delta(\Delta R/\Delta t)$ (ohm/sec)	Adsorption time Δt (sec)
30s HG	0.1	0.035	54
	0.2	0.076	32.4
	0.5	0.193	16.2
10s NG	0.1	0.016	46.8
	0.2	0.026	36
	0.5	0.063	18

6.2.4 The charge doping effect on the sensing performance

To gain insights into the effect of electrical doping on the GFETs sensing performance, graphene with different levels of surface freshness and nitrogeation were further studied. As illustrated in Figure 6.4a, the mobility generally decreases for graphene after ageing ($\sim 600 \text{ cm}^2 \text{ V}^{-1} \text{ s}^{-1}$) compared to the pristine graphene ($\sim 1000 \text{ cm}^2 \text{ V}^{-1} \text{ s}^{-1}$). Such a difference presumably originates from the presence of hydrocarbons adsorbed at the surface of graphene, acting as scatterers for charge carriers.^[15] Correspondingly, aged graphene shows a p-doping behavior with a more positive CNP compared to pristine graphene (Figure 6.4b), which can be ascribed to the electron transfer from graphene to oxygen molecules dissolved in the adsorbed water layer at the surface of aged graphene.^[16] As a result, the p-doping effect induced by ageing is likely to be responsible for the improved response of graphene (aged, without chemical functionalization) to 0.1 ppm ethylene (Figure 6.4c). This is also consistent with the observation that graphene with more p-doping shows a higher sensitivity in Figure 6.2.

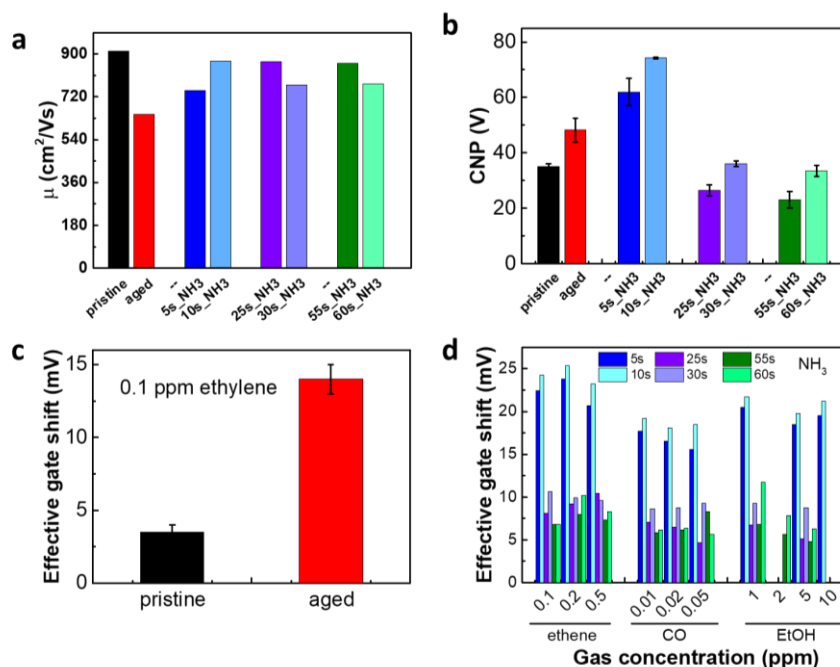


Figure 6.4 The charge doping effect on the GFETs sensing performance. a) The mobility for pristine, aged, nitrogeated graphene (5, 10, 25, 30, 55, and 60 s). b) The charge neutrality points (CNP) of the graphene samples in a). c) The effective gate shifts for pristine and aged graphene to 0.1 ppm ethylene. d) Effective gate shifts for nitrogeated graphene (5, 10, 25, 30, 55, and 60 s) towards the detection of 0.1, 0.2, 0.5 ppm of ethylene, 0.01, 0.02, 0.05 ppm of CO and 1, 2, 5, 10 ppm of EtOH.

Figure 6.4a shows that nitrogenation only slightly decreased the mobility of graphene even when the treating time increased from 5 to 60 s. Compared to the CNP of pristine graphene (35 V), low levels of nitrogenation positively shift the CNP to 62 V (5 s) and 74 V (10 s) and induce a p-doping effect in graphene (Figure 6.4b). In contrast, further nitrogenation (25 to 60 s) negatively shifts the CNP to ~ 30 V, forming n-doped NG as compared to the p-doped NG (5 to 10 s). According to the literature, pyridinic nitrogen causes p-doping while pyrrolic and graphitic nitrogen introduce n-doping effect in graphene.^[11] Therefore, low levels of nitrogenation (5 to 10 s) are expected to mainly form pyridinic nitrogen dopants while pyrrolic and graphitic nitrogen dominate for higher levels of nitrogenation (25 to 60 s).

Figure 6.4d shows the effective gate shifts of different nitrogenated GFETs to the three gas species with increasing concentrations. It is found that more than 10 s of nitrogenation in graphene reduces the responses to all the gas species compared to those after 5 and 10 s. This trend coincides well with the doping transition from p-type to n-type in NG, further confirming that more p-doping in graphene favors the gas adsorption and thus more sensitive responses. Moreover, the responses on all the NG samples exhibit no dependency (or even decreased dependency) on the increasing gas concentrations. Such saturation effects in the sensing performance may be ascribed to the much higher adsorption coefficient than the desorption coefficient of the gas molecules from NG. As a consequence, NG is not a suitable sensing element for gas sensors regardless of the nitrogen doping levels.

6.3 Conclusions

Field effect transistors based on hydrogenated and nitrogenated graphene (HG and NG) have been successfully fabricated for the gas sensing of ethylene, carbon monoxide and ethanol. Compared to the pristine graphene, 30 s HG and 10 s NG both show enhanced sensitivity, however with low selectivity to each of the gas. A higher sensitivity is obtained on the HG with a higher p-doping effect, indicating that positive doping in graphene is related to the improved sensitivity. Besides, only the HG shows positively correlated real-time responses to increased ethylene concentrations. Meanwhile, higher levels of nitrogenation (25 to 60 s) in graphene decreases the responses compared to the low levels of nitrogenation (5 to 10 s). More importantly, p-doping induced by hydrogenation, low levels of nitrogenation and ageing are found to correlate with an increased sensitivity. In conclusion, chemical modification of graphene contributes to change the sensing sensitivity of several gas by introducing p or n doping by modifying the adsorption-desorption process. However, the influence of the surface modification on the selectivity is very limited. To improve the

selectivity via specific recognition between the surface functionalities of graphene and the analytes will have to be developed.

6.5 References

- [1] K. S. Novoselov, A. K. Geim, S. V. Morozov, D. Jiang, Y. Zhang, S. V. Dubonos, I. V. Grigorieva, A. A. Firsov, *science* **2004**, 306, 666.
- [2] a) K. S. Novoselov, A. K. Geim, S. Morozov, D. Jiang, M. Katsnelson, I. Grigorieva, S. Dubonos, Firsov, AA, *Nature* **2005**, 438, 197; b) C. Lee, X. Wei, J. W. Kysar, J. Hone, *science* **2008**, 321, 385.
- [3] a) W. Fu, T. F. van Dijkman, L. M. Lima, F. Jiang, G. g. F. Schneider, E. Bouwman, *Nano Lett.* **2017**, 17, 7980; b) W. Fu, L. Jiang, E. P. van Geest, L. M. Lima, G. F. Schneider, *Adv. Mater.* **2017**, 29, 1603610.
- [4] a) D. C. Elias, R. R. Nair, T. Mohiuddin, S. Morozov, P. Blake, M. Halsall, A. C. Ferrari, D. Boukhvalov, M. Katsnelson, A. Geim, *Science* **2009**, 323, 610; b) H. Feng, R. Cheng, X. Zhao, X. Duan, J. Li, *Nature communications* **2013**, 4, 1539; c) W. Fu, C. Nef, A. Tarasov, M. Wipf, R. Stoop, O. Knopfmacher, M. Weiss, M. Calame, C. Schönenberger, *Nanoscale* **2013**, 5, 12104; d) N. Dontschuk, A. Stacey, A. Tadich, K. J. Rietwyk, A. Schenk, M. T. Edmonds, O. Shimoni, C. I. Pakes, S. Prawer, J. Cervenka, *Nature communications* **2015**, 6, 6563; e) M. B. Lerner, F. Matsunaga, G. H. Han, S. J. Hong, J. Xi, A. Crook, J. M. Perez-Aguilar, Y. W. Park, J. G. Saven, R. Liu, *Nano Lett.* **2014**, 14, 2709.
- [5] J. Duan, S. Chen, M. Jaroniec, S. Z. Qiao, *ACS Catal.* **2015**, 5, 5207.
- [6] a) F. Tuinstra, J. L. Koenig, *J. Chem. Phys.* **1970**, 53, 1126; b) P. Lespade, A. Marchand, M. Couzi, F. Cruege, *Carbon* **1984**, 22, 375.
- [7] L. G. Cançado, A. Jorio, E. H. M. Ferreira, F. Stavale, C. A. Achete, R. B. Capaz, M. V. O. Moutinho, A. Lombardo, T. S. Kulmala, A. C. Ferrari, *Nano Lett.* **2011**, 11, 3190.
- [8] A. Eckmann, A. Felten, A. Mishchenko, L. Britnell, R. Krupke, K. S. Novoselov, C. Casiraghi, *Nano Letters* **2012**, 12, 3925.
- [9] X. Li, Y. Zhu, W. Cai, M. Borysiak, B. Han, D. Chen, R. D. Piner, L. Colombo, R. S. Ruoff, *Nano Lett.* **2009**, 9, 4359.
- [10] L. Jiang, W. Fu, Y. Y. Birdja, M. T. Koper, G. F. Schneider, *Nat. Commun.* **2018**, 9, 793.

- [11] T. Schiros, D. Nordlund, L. Pálová, D. Prezzi, L. Zhao, K. S. Kim, U. Wurstbauer, C. Gutiérrez, D. Delongchamp, C. Jaye, *Nano Lett.* **2012**, 12, 4025.
- [12] S. D. Sarma, S. Adam, E. Hwang, E. Rossi, *Rev. Mod. Phys.* **2011**, 83, 407.
- [13] J. Balakrishnan, G. K. W. Koon, M. Jaiswal, A. C. Neto, B. Özyilmaz, *Nat. Phys.* **2013**, 9, 284.
- [14] J.-H. Chen, C. Jang, S. Adam, M. Fuhrer, E. Williams, M. Ishigami, *Nat. Phys.* **2008**, 4, 377.
- [15] Z. Li, Y. Wang, A. Kozbial, G. Shenoy, F. Zhou, R. McGinley, P. Ireland, B. Morganstein, A. Kunkel, S. P. Surwade, *Nat. Mater.* **2013**, 12, 925.
- [16] Z. Peng, R. Yang, M. A. Kim, L. Li, H. Liu, *RSC Adv.* **2017**, 7, 27048.

Chapter 7

Summary, Conclusions and Outlook

7.1 Summary and conclusions

Advanced sensing techniques require graphene with high quality and well-controlled surface chemistry. The intrinsic high mobility, low electrical noises and uniform graphitic crystallinity are the prerequisites for high-performance graphene electronics. More importantly, chemical functionalization contributes to unlock the sensing potential of the graphene basal plane. This thesis focuses on manipulating the surface chemistry of a graphene monolayer and explores the impacts on the electrical and electrochemical properties for sensing applications. Heteroatoms like hydrogen, nitrogen and oxygen were systematically introduced into the graphene lattice as defect sites to modify the surface chemistry, and consequently the electronic properties. In particular, the interplay between the in-plane electron transport and the electrochemical activity of the graphene basal plane was investigated by modulating the density of H- sp^3 defects (Chapter 2). Moreover, the electronic structure of graphene was found to also determine the electrochemical activity and catalytic properties of the surface. Therefore the electrocatalysis of oxygen reduction reaction on nitrogen doped monolayer graphene was conducted to pinpoint the catalytic active sites (Chapter 3). Meanwhile, the delicate surface of graphene is very sensitive to any surface contaminations, which are found to impair its intrinsic active electrochemistry by covering the crystalline lattice. Hydrogenation treatment was also able to improve and maintain the cleanliness of graphene surface by forming a protective layer of adsorbed water (Chapter 4). Furthermore, the interaction at the supportive interfaces of graphene can also impact its intrinsic properties. The mechanics of a centimeter-scale graphene floating on water was characterized by biaxial compression, and was found to be significantly influenced by lattice defects (Chapter 5). Especially, the introduced H- sp^3 defect sites locally interact with the underlying water molecules to stabilize the corresponding carbon atoms, leading to an enhanced in-plane stiffness. Finally, gas sensors based on hydrogenated and nitrogenated graphene were tested to understand the impacts of chemical functionalization on the sensing performance.

Chapter 2 shows how the electronic nature interplays with the electrochemical activity of a monolayer graphene upon hydrogenation. Through a hydrogen radical plasma, hydrogen atoms were systematically introduced onto the lattice as defects to modulate the chemical and electrical properties of graphene. Raman spectroscopy characterized the density growth and sp^3 nature of the hydrogenated defects. In contrast to the typical decrease of mobility and minimum conductance of graphene induced by hydrogenation, improved conductance and electrochemical activity was obtained after the first second treatment of hydrogen radical plasma. The increase is ascribed to the intrinsically active graphene lattice exposed by removing the

hydrocarbons coverage at the surface. Moreover, the quantum capacitance effect in graphene, originating from the low density of states (DOS) at the Dirac point, was studied to understand the interaction between the electrical and electrochemical properties. By correlating the DOS with the electrochemical activity, the electrochemical kinetics of graphene is concluded to be highly dependent on the DOS upon the addition of hydrogenated defects even in a low density.

In Chapter 3, nitrogen doping in monolayer graphene is investigated for the electrocatalysis of oxygen reduction reaction (ORR). Pyridinic and graphitic nitrogen atoms as the two main doping configurations were confirmed to introduce a n-doping effect in graphene. At high levels of nitrogenation, nitrogen dopants tended to cluster and to form domain-like defect sites, which increased the accompanying surface oxidation. Both sides of the chemical vapor deposition (CVD) graphene, referred to as pure graphene (the side facing the growth substrate) and RRDE graphene (the side facing the air), were adopted for ORR study. For pure graphene containing minimized surface oxidation, decreased ORR currents were observed upon the increase of nitrogen doping levels. In contrast, RRDE graphene accommodating more surface oxidation due to air exposure and ageing showed improved ORR activity with increased nitrogenation. As a consequence, nitrogen dopants are not the essential sites for improved ORR currents. Instead, the content of single-bonded oxygen-containing groups is positively correlated to the enhanced ORR activity in nitrogenated graphene.

As aforementioned, the surface of graphene is sensitive to airborne contaminations, which can significantly alter the surface-related properties including electrochemistry and wettability. Chapter 4 demonstrates an effective and non-invasive cleaning protocol to improve and maintain the cleanliness of the graphene surface. In comparison to pristine graphene and argon treated graphene, hydrogenated graphene presented a quantitatively cleaner surface with less coverage of amorphous patterns arising from airborne hydrocarbons. Moreover, hydrogenated graphene revealed a higher affinity towards water adsorption as compared to pristine graphene, which is closely related to the observed cleaning effect.

Chapter 5 explores the mechanics of a centimeter-scale graphene remaining in its natural form by using water as the supporting substrate. Upon a biaxial compression by a surrounding lipid monolayer in a Langmuir-Blodgett trough, graphene was subjected to deformation (both elastic and plastic) due to the strain in the lattice induced by stress. Characterized by the Young's modulus (\bar{E}_{2D}), the stiffness of graphene is two orders of magnitude smaller than flat graphene, featuring an anharmonic approximation for the total elastic energy. In the anharmonic framework

coupling the stretching and flexural mode in 2D materials, the Young's modulus in hydrogenated graphene was found to be improved by 1.5 times. The improved stiffness is attributed to the localization of the long wavelength flexural modes by H- sp^3 defects in the lattice. In contrast, the inclusion of vacancy defects dramatically lowered the critical stress of graphene, leading to a collapsed graphene upon even a negligible surface pressure.

Chapter 6 shows the field effect gas sensing on hydrogenated and nitrogenated graphene. The introduced chemical functionalization contributed to improve the sensitivity by changing the doping effect and adsorption affinity to gas molecules. Positive doping was found to be positively related to improved electrical responses while negative doping showed decreased responses. Upon dynamic gas detection, the graphene sensors produced saturated and then decreased responses with increased gas concentrations. The consumption of the limited active sites in graphene by the trapped gas molecules can be the explanation. In comparison, hydrogenated graphene exhibited higher sensitivity with less saturation effect than nitrogenated graphene. On the other hand, the limited selectivity for both graphene sensors can be ascribed to the deficiency of specific interaction between the chemical functionalization with the target gas molecules.

7.2 Outlook

A graphene surface is a robust and flexible platform for electrical and electrochemical sensing applications. The work in this thesis provides important insights into the manipulation of the surface chemistry and understanding the corresponding impacts on the intrinsic electrical, electrochemical and mechanical properties of a monolayer of graphene. Chemical defects in the lattice hold the great promise to modulate the electrochemical activity, charge doping and surface adsorption behaviors, to name a few, which are closely involved in the sensing process. Especially, surface contaminations and oxidation of graphene during the handling and ageing process can exert significant impacts on the electrical and electrocatalytic properties. The cleaning approach introduced in the thesis provides not only practical strategy for the electron microscopy study of graphene, but also fundamental insights into the physical chemistry of the graphene surface.

For hydrogenated graphene, it is worthwhile to further investigate its potential as an ideal platform for surface/interface related study. The proposed clean, hydrophilic, mechanically robust and well-preserved graphitic lattice is appealing to (cryo-) electron microscopy study and biointerface involved research. In the viewpoint of GFETs sensing applications, high mobility of graphene after medium hydrogenation is

reasonably preserved while the electrochemical leakage current as a potential leakage signal is minimized. Moreover, the electrochemically active graphene surface after mild hydrogenation functions as an excellent two-dimensional electrode with a low capacitive background current and a large potential window. Furthermore, unpaired electrons or highly reactive free radical trapped at graphene surface can be probed by electron paramagnetic resonance (EPR) or spin-sensitive scanning tunneling microscopy (STM) to reveal mechanisms of certain reactions and gain deep understanding of graphene chemistry.

In particular, the electrocatalytic study on nitrogenated graphene promise monolayer graphene films as a robust and functional surface to monitor *in-situ* reactions using *operando* techniques. For example, surface characterization techniques like Raman and infrared spectroscopy can be employed to monitor systematically how subtle changes of graphene surface chemistry correlate with the mechanism of electrocatalytic reactions, i.e. ORR or hydrogen evolution reactions.

A major problem of polycrystalline CVD graphene is the inevitable oxidation and atmospheric contaminations accompanied with the loss of electrical quality, referred to as “ageing” process. Domain sizes and the amounts of grain boundary in CVD graphene are suspected to be closely related to the ageing effect. According to the recent experimental findings in Leiden, CVD graphene with smaller crystalline domain size is more prone to air oxidization and electrical degradation. For sensitive and stable graphene-based sensing applications, monocrystalline graphene is recommended.

The surface of graphene even after chemical functionalization has limited sensitivity and low selectivity towards the sensing of gas molecules as revealed in Chapter 6. To reach ultra-high sensitivity and selectivity in sensing, specific recognitions like antigen-antibody interactions or biomarkers functionalization should be introduced. Diazonium chemistry can open up a wide range of options for the selective and controlled surface modification of graphene. In spite of the loss of mobility to certain levels, diazonium functionalized graphene can be functioning as sensitive and selective GFET sensing platforms.

Appendix I

Supporting Information for Chapter 2

AI. 1 Materials and methods

GFET device fabrication

To fabricate the GFET devices, the graphene side of the copper growth substrate (CVD graphene, Graphenea S.A.) is glued to a glass slide with a PETMP–TATATO polymer.^[1] PETMP–TATATO (Sigma Aldrich) is a clean and biocompatible polymer usually used for dental restorative application.^[2] After sufficient photo-initiated crosslinking reaction at room temperature (12 h in daylight), the whole stack (glass-glue-graphene-copper) was oxidized with an O₂ plasma (60 W/0.5 mbar/2 min) to remove the trace of graphene that had grown on the backside of the copper substrate (i.e. the side now facing to the air). To fabricate the source and drain electrodes, both ends of the copper substrate (a strip of copper) were protected by a polymer film of cellulose acetate butyrate (CAB, 30 mg mL⁻¹ in ethyl acetate, Sigma Aldrich). An ammonium persulfate solution (0.5 M) was used to etch the non-protected copper foil to reveal the clean CVD graphene supported by the photopolymer and glass substrate without any possible polymer residues. Finally, the fabricated graphene devices were exposed to a hydrogen plasma for different durations to introduce defects with controlled densities.

Thiol-enes polymer

Commercially available pentaerythritol tetra(3-mercaptopropionate) and triallyl-1,3,5-triazine-2,4,6-trione (referred to as PETMP and TATATO, respectively) are used as monomers for the thiol-ene resin formulation. 4:3 volume proportion of PETMP-TATATO were selected for the preparation of the photopolymer.

Plasma condition

A capacitively coupled plasma system with the radio-frequency (RF) of 40 kHz and 200 W power from Diener electronic (Femto) was employed at room temperature. The base pressure of this system is <0.02 mbar. The parameters used for the controlled introduction of defects were 10 W/1.0 mbar for hydrogen plasma and 8 W/0.85 mbar for argon plasma. Specifically, a Faraday cage with grid was employed to shield all the energetic hydrogen ions to form a mild radical plasma to react with graphene.

Characterizations

Raman spectroscopy and mapping were collected from both exfoliated graphene and CVD graphene (using the PMMA transfer method^[3]) on SiO₂/Si substrate. Raman spectra on PETMP-TATATO polymer was performed (see Figure AI. 2a). The Raman

spectrometer used is a WITEC alpha300 R – Confocal Raman Imaging with a laser wavelength of 532 nm. To minimize the potential damage from laser heating effect, the laser power was controlled under 1.1 mW. All of the measurements were performed under ambient conditions at room temperature. XPS data were collected from a K-Alpha X-ray photoelectron spectrometer by Thermo Scientific, and the internal reference was adopted with the binding energy of the C 1s peak at 284 eV. Scanning electron microscopy (SEM) images were carried out from a JEOL SEM 6400 microscope. Transmission electron microscopy (TEM) images were collected from a FEI Titan 80–300 microscope. A JPK NanoWizard Ultra Speed AFM was employed to characterize the topology of graphene before and after hydrogenation on SiO₂/Si substrate. The images were scanned in an intermittent contact mode in air at room temperature.

Electrical measurement

The transport measurements of GFET devices upon different hydrogenation times were performed on a SR830 DSP lock-in amplifier with narrow filters. Electrolyte- or electrochemical-gated GFET measurements were carried out in 0.1 M KCl solution containing 10 mM Tris as the buffer (pH 8, both from Sigma Aldrich). The gate voltage was applied on a AgCl/Ag wire as the reference electrode, at a sweep rate at 100 mV s⁻¹, while the source/drain current was fixed at 0.1 μA.

Quantum capacitance

As illustrated in Figure AI. 4, the total capacitance C_{tot} of an electrolyte-gated GFET, is composed of two components in series, quantum capacitance C_q and the electric double-layer capacitance C_{dl} . The C_{dl} for the KCl solution can be approximated as 10–20 μF cm⁻² for a wide range of ionic concentration >1 mM^[4]. C_q is relatively small (~1 μF cm⁻²) compared to the C_{dl} (in series) and thus dominates the total capacitance $C_q \sim C_{tot}$ ^[5]. By calculating the C_q based on $1/C_{tot} = 1/C_q + 1/C_{dl}$, we get the curves of C_q vs V_{ch} – the potential distributed on graphene channel – derived by $V_{ch} = (V_g C_{dl}) / (C_{dl} + C_q)$ for different hydrogenation times.

Electrochemical measurement

The electrochemical experiments were carried out in a homemade one-compartment three-electrode electrochemical cell at ambient conditions. The working electrode is the CVD grown graphene and the counter electrode a platinum wire. All potentials in this work are reported with respect to a saturated Ag/AgCl reference electrode. A potentiostat/galvanostat (CompactStat, Ivium Technologies) was used for the

electrochemical measurements. The electrolyte, 0.1 M KCl, was prepared from KCl (Sigma Aldrich, $\geq 98\%$) and ultrapure water (Millipore Milli-Q gradient A10 system, 18.2 M Ω .cm). The measured current was normalized to the geometric surface area of the working electrode and not corrected for Ohmic drop as the obtained currents were very low. Prior to the experiments, the cell containing the electrolyte solution was purged with argon to remove the dissolved oxygen.

Table AI. 1 XPS analysis (C 1s and O 1s peaks) of H- vs Ar-graphene deposited on a Si/SiO₂ wafer

	C 1s			O 1s		
	BE (eV)		at (%)	BE (eV)		at (%)
H-graphene (fresh)	284	sp^2 C	81.41			
	285	sp^3 C	6.22	532.3	Si-O	86.67
	286	C-O	6.61	533.8	C-O	6.86
	288	C=O	5.76	531.1	C=O	6.47
H-graphene (aged)	284	sp^2 C	79.60			
	285	sp^3 C	8.05	532.4	Si-O	85.79
	286	C-O	5.97	533.6	C-O	6.70
	288	C=O	6.37	531.2	C=O	7.51
Ar-graphene	284	sp^2 C	69.5			
	285.1	sp^3 C	3.01	532.2	Si-O	86.49
	285.8	C-O	12.09	533.5	C-O	6.95
	287.8	C=O	15.41	531.3	C=O	6.57

*aged: one week after sample preparation.

BE: binding energy

AI. 2 Raman characterization of exfoliated and CVD graphene

To better identify the density and the nature of H- sp^3 defects generated through hydrogenation, in this study we conduct Raman mapping on CVD graphene on Si/SiO₂ (Figure AI. 1a) and on exfoliated graphene (Figure AI. 1b). Moreover, Figure AI. 2a shows the Raman spectra acquired on both exfoliated graphene on Si/SiO₂ (left panel)

and CVD graphene on photopolymer (right panel), prepared with minimized contaminations (i.e. no PMMA residues). The signal-to-noise (SNR) ratio is lower in case of CVDG on polymer compared to graphene on Si/SiO₂ because: i) a low laser power is required to prevent heating of the underlying delicate polymer substrate; ii) the redundant peaks from the polymer (at ~1432 cm⁻¹ and ~1760 cm⁻¹) render the Raman measurements on CVDG more difficult. Figure AI. 2b shows the peak intensities and the $I(D)/I(G)$ ratio for exfoliated and CVD graphene after 2 s, 5 s and 10 s of hydrogenation. The Raman data for both types of graphene are comparable, suggesting similar quality (i.e. H₂-plasma induced defects) for the two types of graphene.

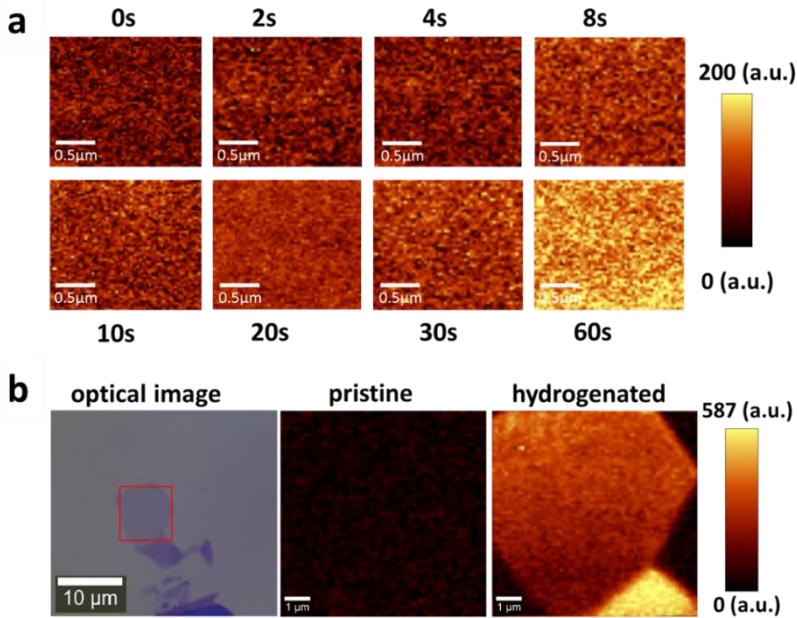


Figure AI. 1 Raman mapping of graphene upon hydrogenation. a) Maps of the D band intensity of CVD graphene with hydrogenation time ranging from 0 to 60 s. b) Maps of the D band intensity for pristine (0 s) and hydrogenated graphene (60 s). Graphene was obtained by exfoliation of natural graphite.

The defect density n_D of H- sp^3 defects in graphene can be estimated based on $I(D)/I(G)$ using Equation 1:^[6]

$$n_D = \frac{(1.8 \pm 0.5) \times 10^{22} (I_D/I_G)}{\lambda_L^4} \quad (1)$$

where λ_L denotes the excitation laser wavelength, which is 532 nm here. Moreover, the average distance between defects sites, L_D (nm), can be calculated based on $n_D(\text{cm}^{-2}) = 10^{14}/(\pi L_D^2)$.

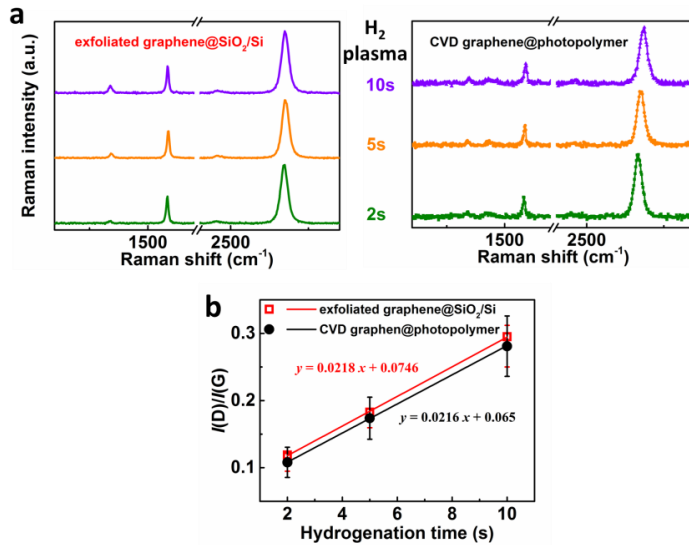


Figure AI. 2 Raman spectra on exfoliated and CVD graphene. a) Raman spectra collected from exfoliated (left panel) and CVD (right panel) graphene after 2 s, 5 s and 10 s of hydrogenation. b) The $I(D)/I(G)$ ratio extracted from exfoliated (red hollow square) and CVD (black solid dot) graphene. The error bars in b) are defined by the standard deviation of experimental values.

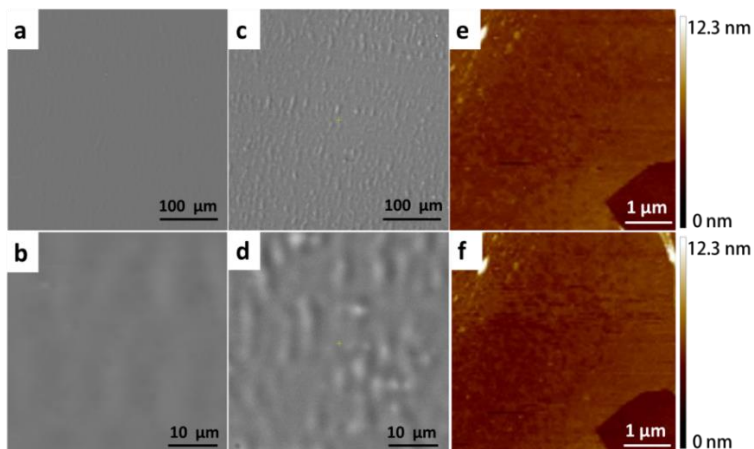


Figure AI. 3 Scanning electron microscopy (SEM) and atomic force microscopy (AFM) of hydrogenated graphene. SEM of hydrogenated graphene on a PETMP-TATATO polymer before (a, b) and after (c, d) hydrogenation. AFM of exfoliated graphene on Si/SiO₂ before (e) and after (f) hydrogenation.

AI. 3 Quantum capacitance calculation

In detail, quantum capacitance (C_q) is measured by adopting a two-electrode configuration (Figure AI. 4). The minimum quantum capacitance, $C_{q,\min}$, is related to the additional carrier density n^* by the following Equation 2

$$C_q = \frac{2e^2 \sqrt{n_G + n^*}}{\hbar v_F \sqrt{\pi}} \quad (2)$$

where $n_G = \left(\frac{eV_{ch}}{\hbar v_F \sqrt{\pi}}\right)^2$ represents the carrier density created by the gate voltage (V_g).^[7] Then we extracted the n^* from $C_{q,\min}$ when $n_G = 0$.

Furthermore, based on self-consistent theory^[8], we determine the impurity density, n_{imp} , based on n^*

$$n_{\text{imp}} = \frac{n^*}{[2r_s^2 C_0^{\text{RPA}}(r_s, a = 4d\sqrt{\pi n^*})]} \quad (3)$$

where $r_s = \frac{2e^2}{\hbar v_F(\epsilon_1 + \epsilon_2)}$, C_0^{RPA} is the correlation function from the random phase approximation (RPA), and d (~ 1 nm) is the average distance between the charged impurity and graphene. ϵ_1 is the dielectric constant of the photopolymer and ϵ_2 the dielectric constant of electrolyte solution, respectively.

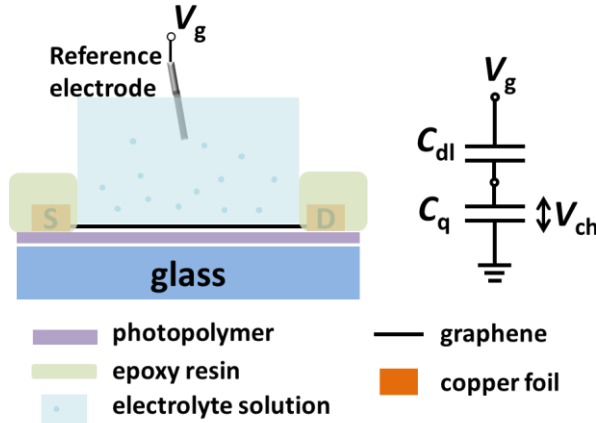


Figure AI. 4 Quantum capacitance measurement setup and circuit illustration.

AI. 4 k^0 calculation

We used the Nicholson's method^[9] to calculate k^0 with Equation 4

$$\psi = k^0 (D_O/D_R)^{\alpha/2} (RT/\pi n F D_O \nu)^{1/2} \quad (4)$$

where ψ is a dimensionless kinetic parameter determined by ΔE_p ,

$$\psi = \frac{(-0.6288 + 0.00241 n \Delta E_p)}{(1 - 0.017 n \Delta E_p)} \quad (5)$$

α is the transfer coefficient, n is the number of electrons transferred, F is the Faraday constant (96500 C mol^{-1}), D_O and D_R is the diffusion coefficient of redox molecules ($\text{cm}^2 \text{ s}^{-1}$), ν is the scan rate (V s^{-1}), R is the gas constant ($\text{VCK}^{-1} \text{ mol}^{-1}$), and T means the temperature in K. Basically, the diffusion coefficients of the reduced and oxidized form for the redox probe are regarded as approximately equal, which gives α about 0.5. As a result, we can apply the Nicholson's method in a simplified form to determine k^0 ,

$$\psi = k^0 \sqrt{RT/\pi n F D \nu} \quad (6)$$

Additionally, the diffusion coefficient, D , can be determined by Randles-Sevcik equation

$$i_p = 0.4463 n F A C \sqrt{\frac{n F D \nu}{RT}} \quad (7)$$

where A is the effective graphene surfaces that were in contact with electrolyte solution.

AI. 5 Reproducibility

We reproduced the hydrogenation on several CVDG samples which all showed at least around 2-times increase in both the CV current density (Figure AI. 5a) and k^0 (Figure AI. 5b) after 1 s of hydrogenation. The differences between k^0 on untreated graphene can be ascribed to the well-known sample-to-sample variations between CVDG originating from the defects formation during the growth or fabrication, or even airborne contaminations from the environment. In addition, the peak-to-peak separation (ΔE_p) for the redox peaks in Figure AI. 5c has a minimum after 1 s of hydrogenation, indicating a more reversible electrochemical process on H-graphene

(1 s) comparing to untreated graphene and other H-graphene with longer times of hydrogenation treatments.

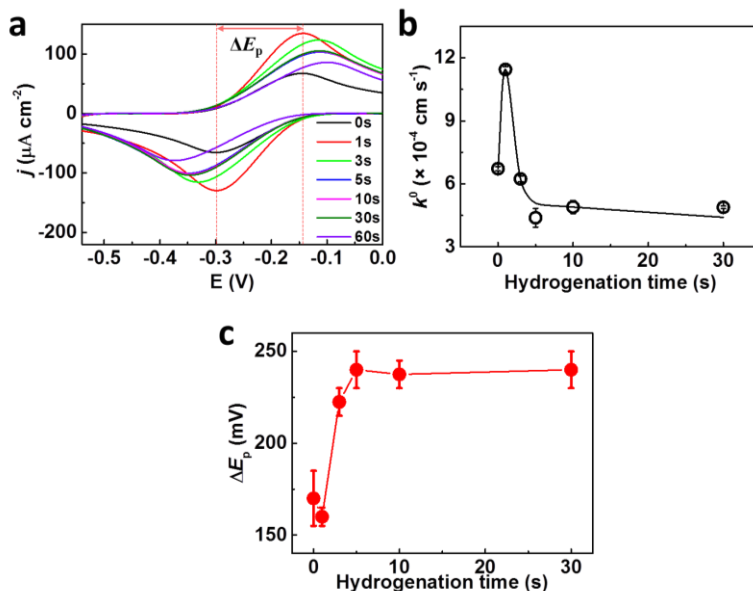


Figure AI. 5 Cyclic voltammograms of hydrogenated graphene. a) Cyclic voltammograms (CVs) collected from the same graphene sample after sequential hydrogenation treatments. The electrolyte solution is 0.1 m KCl containing 10 mM Tris and 1 mM $\text{Ru}(\text{NH}_3)_6\text{Cl}_2/\text{Ru}(\text{NH}_3)_6\text{Cl}_3$, respectively. b) The evolution of electron transfer rate k^0 , along hydrogenation time, extracted from the cvs plotted in a). c) The peak to peak separation (ΔE_p) vs the hydrogenation time. the error bars in (b-c) are defined by the standard deviation of experimental values.

AI. 6 Averaged total capacitance

In Figure AI. 6, we performed capacitive cyclic voltammetry (CV) in 0.1 M KCl solution containing 10 mM Tris on hydrogenated graphene to understand the impact of hydrogenation on the total capacitance. The capacitive current/current density varies with the scan rate (Figure AI. 6a), and can be unified using Equation 8:

$$i \text{ (A)} = C \text{ (F)} \times v \text{ (V s}^{-1}\text{)} \text{ or } j \text{ (A cm}^{-2}\text{)} = C \text{ (F cm}^{-2}\text{)} \times v \text{ (V s}^{-1}\text{)}. \quad (8)$$

We extracted the specific capacitance $C_{\text{ave-tot}}$ of graphene based on the linearity between the current densities and scan rates. For example, the $C_{\text{ave-tot}}$ calculated at the potential of -0.25 V is around $5.37 \mu\text{F cm}^{-2}$ (Figure AI. 6a and b). Consistent with the trend of k^0 versus hydrogenation, the $C_{\text{ave-tot}}$ (extracted from the CVs in Figure

Al. 6c) also increases dramatically after 1 s, and then decreases (2-10 s) and stabilizes at the level of $7.3 \mu\text{F cm}^{-2}$ till 30 s.

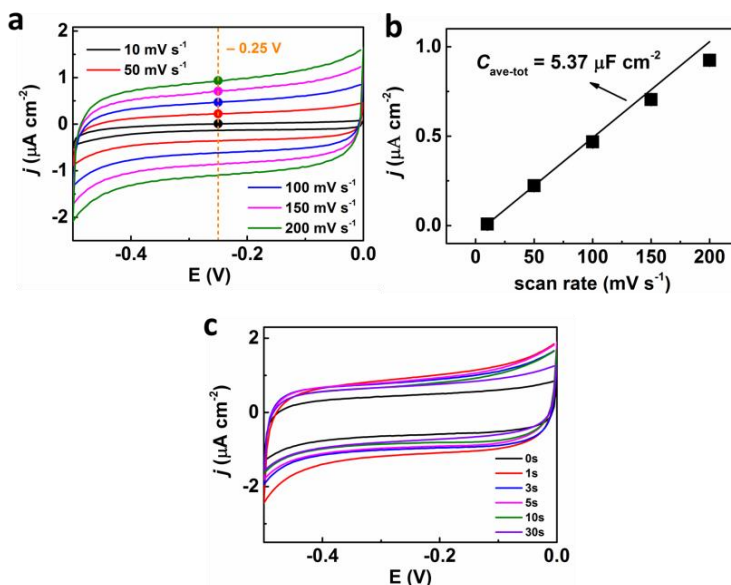


Figure Al. 6 Capacitance measurement for hydrogenated graphene. a) Cyclic voltammograms (CVs) of untreated graphene in 0.1M KCl solution (containing 10 mM Tris) as a function of the scan rate ranging from 10 to 200 mV s^{-1} . b) The plot of the current density (positive-going scan) versus scan rate for an applied potential of -0.25 V . c) Capacitive CVs obtained on graphene before and after 1 to 30 s of hydrogenation. The error bars in (b) are defined by the standard deviation of experimental values.

Al. 7 Raman and electrochemical characterization of Ar treated graphene

To understand to what extent the nature of the defect impacts the electrochemical activity of graphene, we studied vacancy defects on CVD graphene introduced by Ar plasma (Ar-graphene) with comparable defect density levels as for hydrogenated graphene. Figure Al. 7a-b demonstrates the comparable densities (i.e. $I(D)/I(G)$) of Ar-graphene with hydrogenated ones in Figure 1. The electrochemical measurements on Ar-graphene in Figure 3e and f illustrate the barely varied current density and electron transfer rate under the studied defect density. The result echoes well with previous report^[10] where low densities of vacancy defect did not affect the electrochemical activity of the graphene basal plane. However, a dramatically higher density of vacancy defects is expected to improve the electrochemical kinetics at the cost of a lower in-plane electron transport.^[11]

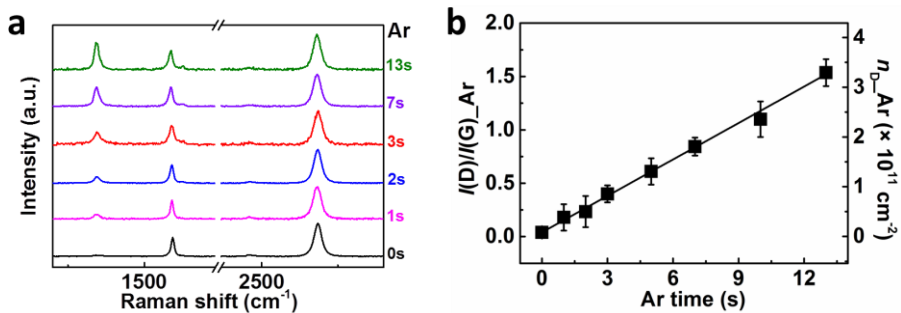


Figure AI. 7 Raman spectroscopy and electrochemistry of Ar-graphene. a) Averaged Raman spectra of CVD graphene transferred on a Si/SiO₂ substrate after the Ar ion plasma (8 w, 0.85 mbar) for 0-13 s. b) The intensity ratio $I(D)/I(G)_{Ar}$ and the derived defect density n_{D_Ar} , plotted vs. the Ar bombarding time. The error bars in (b) are defined by the standard deviation of experimental values.

AI. 8 XPS of H-graphene and Ar-graphene

X-ray photoelectron spectroscopy (XPS) was performed on CVD graphene after hydrogenation and Ar plasma treatment to characterize the chemical stability of plasma treated graphene in ambient condition, and to determine the origin of the H- sp^3 contributions in H-graphene. An asymmetrical fitting function^[12] in combination with Gaussian-Lorentzian functions was used to fit the C 1s spectra. Other symmetric components were fitted with a Gaussian-Lorentzian fitting function. Shirley background was subtracted for the fitting.

On both fresh and aged (one week) samples (Figure AI. 8a and c), the C 1s peak of H-graphene can be deconvoluted into four main peaks: C-C sp^2 (284 eV), C-C sp^3 (285 eV), C-O (286-286.2 eV) and C=O (288 eV).^[13] Confirmed by the atomic ratio analysis (in %) in Table AII. 1, the chemical compositions in H-graphene were stable over time, suggesting a negligible oxidation of H-graphene after aging in ambient conditions. The slight decrease in sp^2/sp^3 ratio for aged samples could originate from the further adsorption of airborne hydrocarbon contaminants. Furthermore, the O 1s spectra in Figure AI. 8b (fresh) and d (aged) also agree well with 1:1 ratio between single and double bonded oxygen groups in H-graphene, except for the dominant Si-O component (from the Si substrate). Consequently, the detected oxygen bands are likely to be attributed to the residues of polymer (PMMA) employed for the graphene transfer process (PMMA was only used to prepare the XPS samples). In fact, 1) highly ordered pyrolytic graphite (HOPG) was not exposed to PMMA and did not show the O 1s band (inset in Figure AI. 8b), and 2) Ar-graphene (Figure AI. 8e and f), which was also exposed to PMMA, showed similar oxygen bands as for H-graphene.

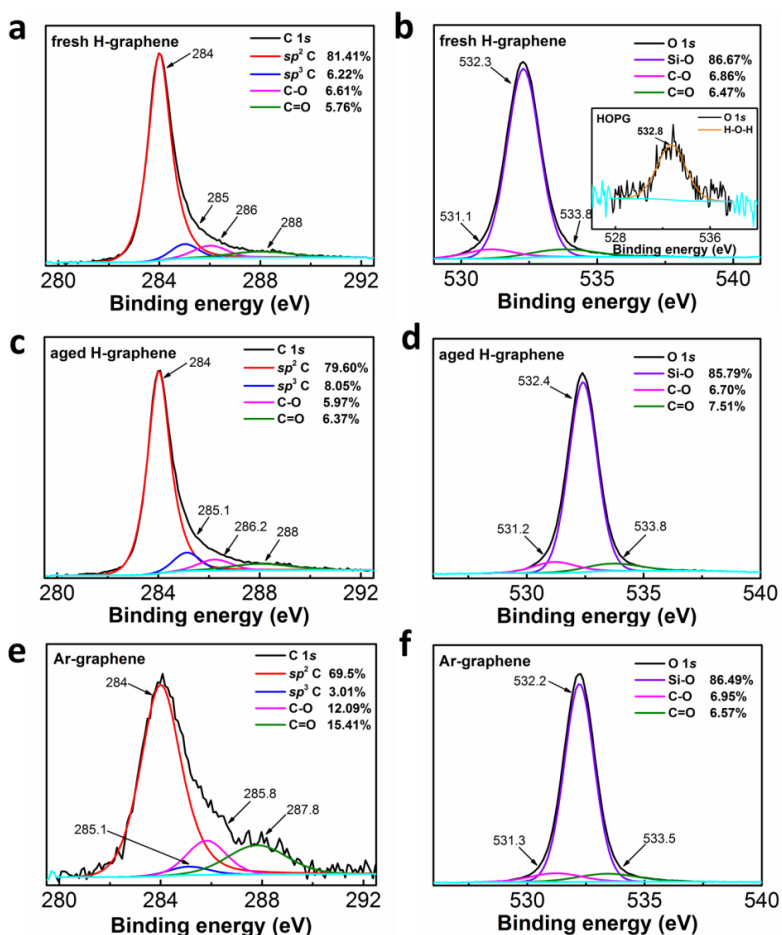


Figure AI. 8 XPS analysis of H-graphene (60 s) and Ar-graphene (13 s) on a Si/SiO₂ substrate. a-b) C 1s (a) and O 1s (b) spectra of H-graphene in fresh state. Inset in b) is the O 1s spectrum for fresh HOPG. c-d) C 1s (c) and O 1s (d) spectra of H-graphene after aging in atmosphere for one week. e-f) C 1s (e) and O 1s (f) spectra of Ar-graphene in fresh state.

Furthermore, we compare the C 1s peak of graphene containing similar defect densities after 60 s hydrogenation (Figure AI. 8a) and after 15 s of Ar plasma treatment (Figure AI. 8e). In addition to the existence of C–O and C=O components, ~3% sp^3 C component was found in Ar-graphene, which is probably attributed to the surface contaminations (i.e. PMMA residues and hydrocarbons adsorption).

AI. 9 References

- [1] W. Fu, C. Nef, A. Tarasov, M. Wipf, R. Stoop, O. Knopfmacher, M. Weiss, M. Calame, C. Schönenberger, *Nanoscale* **2013**, 5, 12104.
- [2] N. B. Cramer, C. L. Couch, K. M. Schreck, J. A. Carioscia, J. E. Boulden, J. W. Stansbury, C. N. Bowman, *Dent. Mater.* **2010**, 26, 21.
- [3] X. Liang, B. A. Sperling, I. Calizo, G. Cheng, C. A. Hacker, Q. Zhang, Y. Obeng, K. Yan, H. Peng, Q. Li, X. Zhu, H. Yuan, A. R. Hight Walker, Z. Liu, L.-m. Peng, C. A. Richter, *ACS Nano* **2011**, 5, 9144.
- [4] S. Baldelli, *Acc. Chem. Res.* **2008**, 41, 421.
- [5] J. Xia, F. Chen, J. Li, N. Tao, *Nature Nanotechnology* **2009**, 4, 505.
- [6] L. G. Cançado, A. Jorio, E. M. Ferreira, F. Stavale, C. Achete, R. Capaz, M. Moutinho, A. Lombardo, T. Kulmala, A. Ferrari, *Nano Lett.* **2011**, 11, 3190.
- [7] A. Das, S. Pisana, B. Chakraborty, S. Piscanec, S. Saha, U. Waghmare, K. Novoselov, H. Krishnamurthy, A. Geim, A. Ferrari, *Nat. Nanotechnol.* **2008**, 3, 210.
- [8] S. Adam, E. Hwang, V. Galitski, S. D. Sarma, *Proc. Natl. Acad. Sci.* **2007**, 104, 18392.
- [9] R. S. Nicholson, *Anal. Chem.* **1965**, 37, 1351.
- [10] a) M. Velický, M. A. Bissett, P. S. Toth, H. V. Patten, S. D. Worrall, A. N. Rodgers, E. W. Hill, I. A. Kinloch, K. S. Novoselov, T. Georgiou, *Phys. Chem. Chem. Phys.* **2015**, 17, 17844; b) J.-H. Zhong, J. Zhang, X. Jin, J.-Y. Liu, Q. Li, M.-H. Li, W. Cai, D.-Y. Wu, D. Zhan, B. Ren, *J. Am. Chem. Soc.* **2014**, 136, 16609.
- [11] L. Vicarelli, S. J. Heerema, C. Dekker, H. W. Zandbergen, *ACS Nano* **2015**, 9, 3428.
- [12] G. Wertheim, *J. Electron Spectrosc. Relat. Phenom.* **1975**, 6, 239.
- [13] A. Ganguly, S. Sharma, P. Papakonstantinou, J. Hamilton, *J. Phys. Chem. C* **2011**, 115, 17009.

Appendix II

Supporting Information for Chapter 3

All. 1 Materials and methods

Materials

Chemical vapor deposition (CVD) graphene is grown on a polycrystalline copper foil (Alfa Aesar, 99.999% purity, 25 mm thickness) in a commercially available hot-wall chamber (planarGROW-2B, planarTECH). Epoxy resin (including the curing agent) was supplied by GENTEC. Poly(methyl methacrylate) (Sigma Aldrich) was used for CVD graphene transfer. Cellulose acetate butyrate (CAB, ~30 mg/mL in ethyl acetate), potassium chloride (KCl, ≥99.0%), potassium ferricyanide ($K_3Fe(CN)_6$, ≥99.0%) and ammonia persulfate ($(NH_4)_2S_2O_8$, ≥98.0%) were supplied by Sigma Aldrich. Sulfuric acid (98% H_2SO_4 , ≥99.999%) and sodium hydroxide monohydrate ($NaOH \cdot H_2O$, TraceSelect ≥99.9995%) were purchased from Honeywell Fluka. Potassium perchlorate ($NaClO_4$, EMSURE®) was ordered from Merck. The electrolyte solution was prepared with ultrapure water (Millipore Milli-Q gradient A10 system, 18.2 MΩ.cm). All gas were supplied by Linde Gas (5.0).

Plasma condition

A capacitively coupled plasma system with a radio-frequency (RF) of 40 kHz and 200 W power from Diener electronic was employed at room temperature. The base pressure of this system is less than 0.02 mbar. To achieve mild plasma conditions, a Faraday cage equipped with grid was employed to shield all the energetic ions, thus forming a mild radical plasma to treat the graphene samples inside the cage. The parameters used for nitrogenation treatments were 16 W power and 0.8 mbar pressure for ammonia plasma. Oxygen plasma was applied with a power of 30W and a pressure of 0.5 mbar.

Structure characterization

Raman spectra and mapping were collected using a WITEC alpha300 R – Confocal Raman Imaging with a laser wavelength of 532 nm. A 100× magnification objective was used to form a laser inspection region of 300 μm in diameter. To minimize the potential damage from laser heating effect, the laser power was controlled under 2 mW. All of the measurements were performed under ambient conditions at room temperature.

The electric transport measurements of graphene field-effect transistor devices were performed on a SR830 DSP lock-in amplifier with narrow filters. Electrolyte- or electrochemical-gated GFET measurements were carried out in 0.1 M KCl solution containing 10 mM Tris as the buffer (pH 8). The gate voltage was applied on a AgCl/Ag

wire as the reference electrode, at a sweep rate of 100 mV s^{-1} , while the source/drain current was fixed at $0.1 \text{ }\mu\text{A}$.

XPS were performed using a K-Alpha X-ray photoelectron spectrometer equipped with a monochromatic X-ray source ($\text{Al K}\alpha = 1486.6 \text{ eV}$) by Thermo Scientific. Energy calibration was performed by refereeing to the C 1s peak of highly ordered pyrolytic graphite (HOPG) at 284.6 eV and CasaXPS software was used to analyze the spectra fitting.

Electrochemical measurements

The electrochemical experiments were carried out in a custom made one-compartment three-electrode electrochemical cell at ambient conditions. The working electrode is the as-prepared graphene and the counter electrode a graphite rod. All potentials in this work are reported with respect to a reversible hydrogen electrode (RHE) reference electrode, a Pt mesh in H_2 saturated electrolyte operating at the same pH and connected to cell via a Luggin capillary. Autolab PGSTAT 12 potentiostats operated by NOVA software were used for the electrochemical measurements. The measured current was normalized to the geometric surface area of the working electrode and not corrected for ohmic drop as the obtained currents were very low. Prior to the ORR experiments, the cell containing the electrolyte solution was purged and saturated with O_2 . For capacitive current measurements, argon was purged at least for 30 min to fully remove dissolved O_2 in the solution. The cyclic voltammetry and polarization curves were measured at a scan rate of 100 mV s^{-1} .

Pure graphene on epoxy support

Epoxy resin (100:45 mass ratio of base to curing agent, EPO-TEK) was slowly poured onto a glass slide substrate (thus air bubble in the mixture was avoided) after homogeneous mixing and degassing in vacuum for 45 min to form a thin layer. The top side of the as-grown CVD graphene on copper foil ($\sim 1.5 \text{ mm} \times 10 \text{ mm}$) was glued attached to the epoxy resin layer (homogeneously mixed with the curing agent) sitting on a glass slide. After the epoxy resin was cured at room temperature for 24 hours, the attached graphene was isolated from the air by the coverage of the air-tight epoxy and the growth copper substrate. Next, graphene that had grown in the backside of the copper (now facing to the air) was removed using an oxygen plasma ($100 \text{ W}/0.5 \text{ mbar}/2 \text{ min}$). After protecting the copper end with a clean and hydrophobic film of cellulose acetate butyrate (CAB), ammonia persulfate solution (0.5 M) was used to etch the non-protected copper and to expose the underlying graphene, referred to as pure graphene. Then the graphene was wired out (using silver epoxy) via the retained

copper foil with a low contact resistance. For the fabrication of graphene field effect transistor devices, similar procedures were adopted except that two ends of the copper foil (a strip of copper) were preserved as source and drain electrodes, respectively.

RRDE preparation

The glassy carbon (GC) disk electrode (0.196 cm²) and platinum ring were supplied by Pine Instruments, and controlled by a Pine MSR rotator in a ChangeDisk configuration. Prior to use, both the disk and ring electrodes were mechanically and separately polished with 1.0, 0.3 and 0.05 micron alumina slurry respectively for 2 min with subsequent rinsing and sonication in water for 10 min. The separate polishing of ring and disk excluded any potential contamination of platinum onto the GC disk electrode. After polishing and cleaning, poly(methyl methacrylate) (PMMA) was spin-coated onto the CVD graphene on copper foil and cured to form a carrier film. After the underlying copper was etched in ammonium persulfate solution, PMMA-graphene layer floating on water (to rinse ammonium salt out) was transferred onto the target substrate, i.e. the GC disk (proposed as monolayer graphene on RRDE) or CVD graphene on copper foil (for bilayer graphene preparation). Finally the transferred graphene was obtained by removing PMMA in acetone. Electrochemical RRDE experiments were carried out in a two-compartment cell with a three-electrode set-up. The counter electrode was separated from the rotating disk electrode via a water permeable glass frit in a different compartment. A capacitor of 10 μ F was connected between the RHE and electrolyte solution through a platinum wire to lower the noise ratio especially for the ring current.

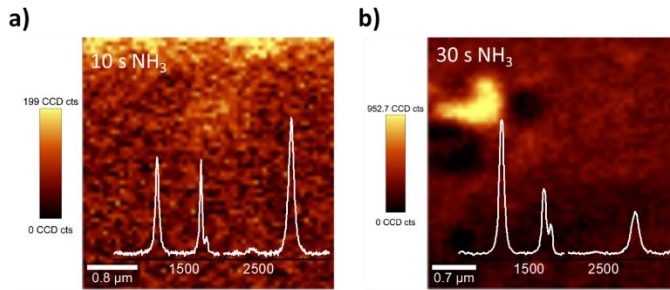


Figure AII. 1 Raman spectroscopy of nitrogenated graphene. Raman mapping of D band intensity of nitrogenated graphene after 10 s (a) and 30 s (b) of nitrogenation treatments, respectively. The insets are the corresponding Raman spectra.

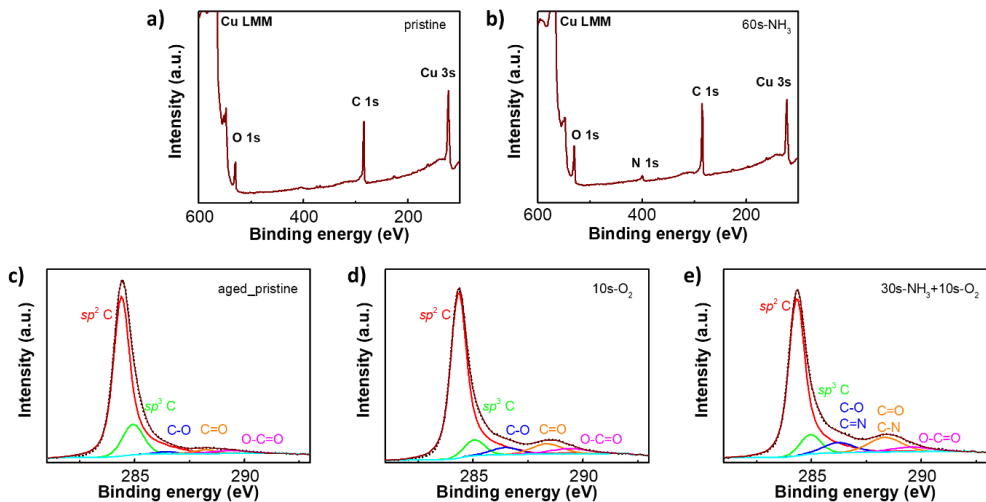


Figure AII. 2 XPS analysis for graphene on copper. a) Survey spectrum for pristine graphene. b) Survey spectrum for graphene treated with 60 s of nitrogenation. c) C1s core spectra for aged (1 month) pristine graphene. d) C1s core spectra for graphene upon 10 s of oxidation. e) C1s core spectra for graphene co-doped with 30 s of nitrogenation and 10 s of oxidation.

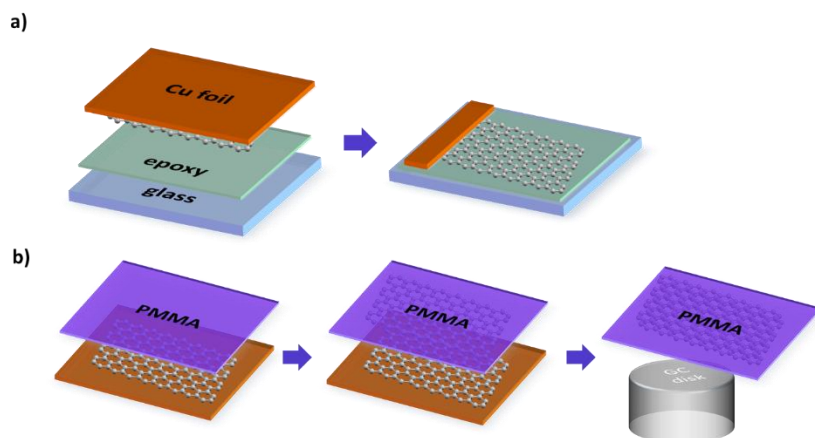


Figure AII. 3 Illustration schemes of graphene surface preparations for ORR measurements. a) Preparation of pure graphene surface supported on epoxy resin. b) Bilayer graphene surface (referred to as RRDE graphene), the opposite face of the pure graphene in (a), is transferred on the glassy carbon (GC) disk.

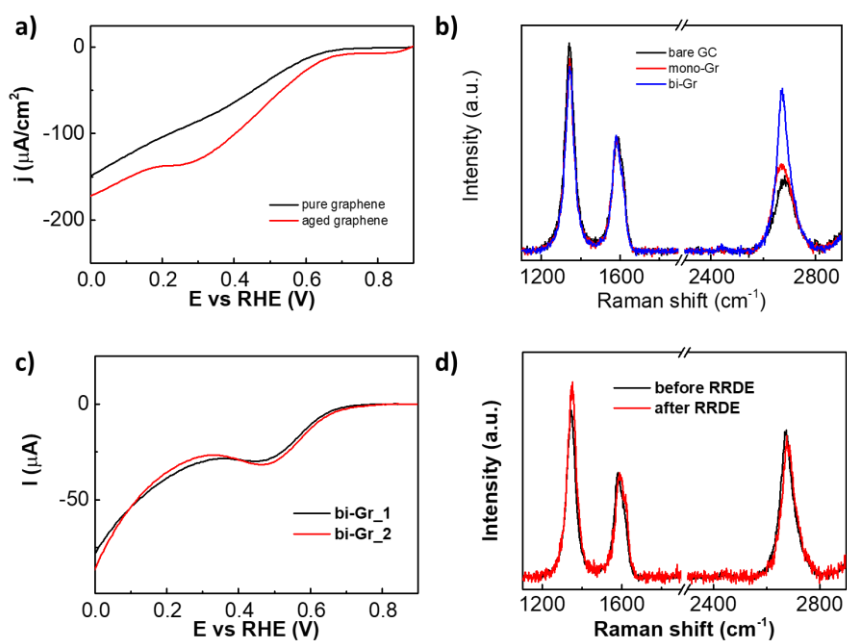


Figure AII. 4 ORR activity and Raman spectroscopy of graphene. a) LSV curves of an aged graphene sample on epoxy substrate with an evident peak at ~ 0.4 V as compared to pure graphene. b) Raman spectra of bare GC, monolayer and bilayer graphene supported by GC. c) LSV polarization curves of two samples of bilayer graphene (denoted as bi-Gr) supported by the same GC disk electrode at 800 rpm in 0.1 M sodium hydroxide solution saturated with O_2 . d) Raman spectra of the bilayer graphene on the GC disk before and after RRDE experiment.

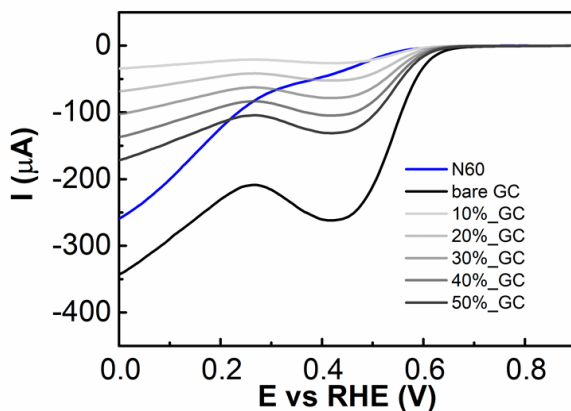


Figure III. 5 Comparison of the ORR activity of N60 graphene on RRDE versus the GC disk. LSV curves for 60 s nitrogenated graphene on the GC disk (N60) and for the GC disk with full (bare GC) or partial exposure (10% to 50%) in terms of the electrode area. The electrolyte solution is 0.1 M sodium hydroxide saturated with O_2 .

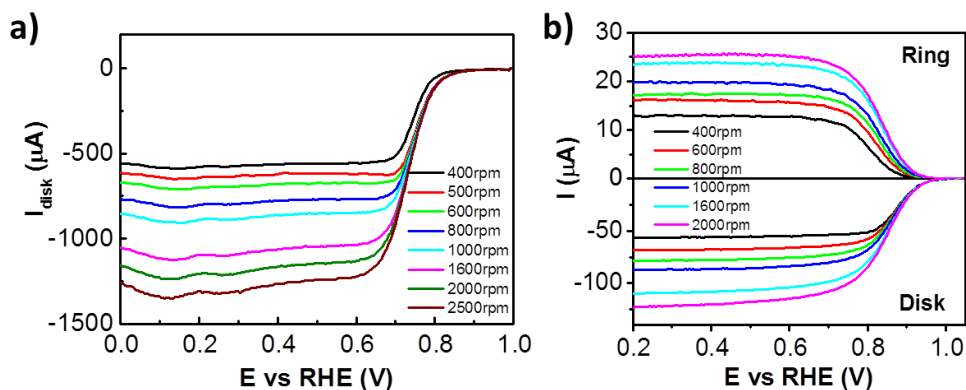


Figure III. 6 Levich constant and collection efficiency. a) ORR polarization curves at different rotation rates on a platinum disk electrode in 0.1 M NaOH solution saturated with O_2 . b) Currents on the GC disk and platinum ring electrodes for 1 mM $K_3Fe(CN)_6$ in 0.1 M $NaClO_4$ purged with argon at different rotation speeds.

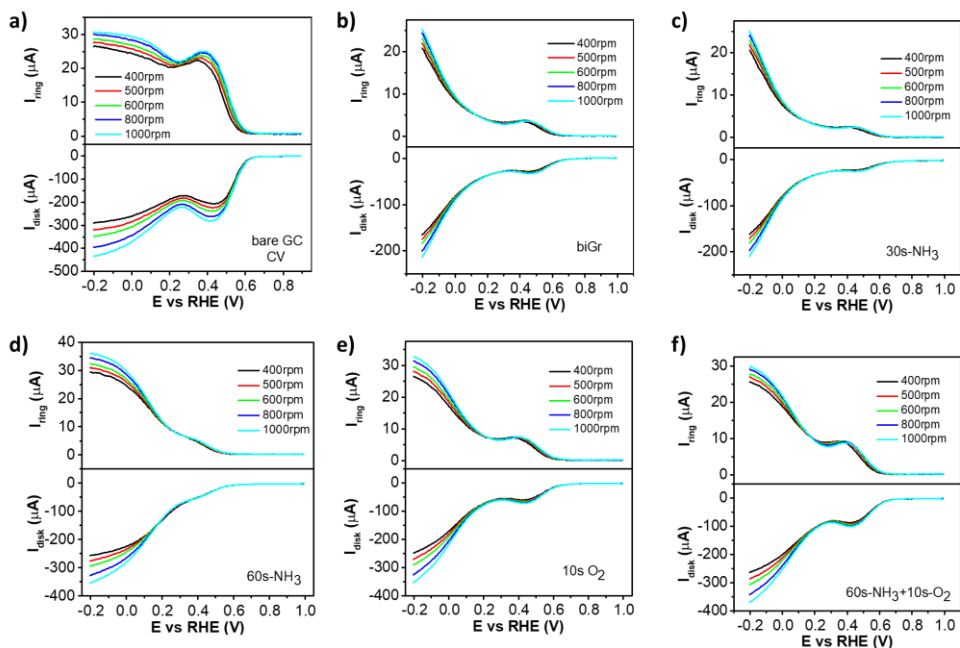


Figure AII. 7 ORR polarization curves of graphene at different rotation rates for Koutecky-Levich plots. a) Bare GC electrode. b) Bilayer graphene on GC electrode. c) 30s nitrogenated graphene. d) 60 s nitrogenated graphene. e) 10s oxygenated graphene. f) 60s nitrogenated and 10 s oxygenated graphene.

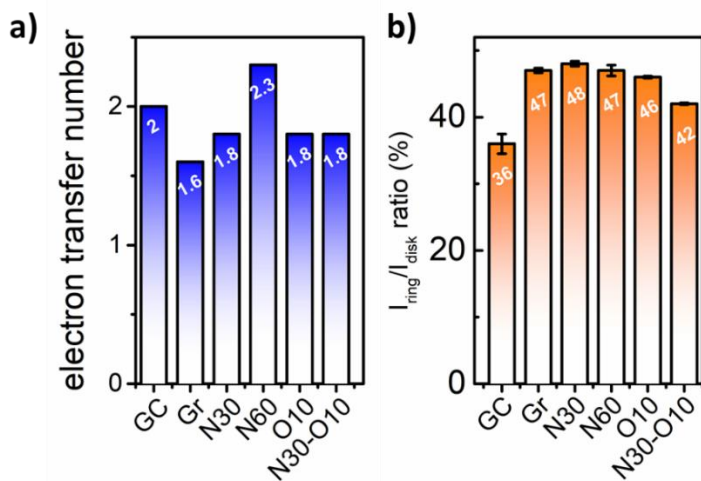


Figure AII. 8 The ORR selectivity of the GC disk and RRDE graphene. a) Electron transfer number based on the K-L plots. b) The ratios of I_{ring} over I_{disk} .

Table AII. 1 Defect density (n_D) and interdefect distance (L_D) analysis based on nitrogenation time

NH ₃ time (s)	0	2	4	6	8
n_D ($\times 10^{10} \text{ cm}^{-2}$)	1 \pm 0.1	3.1 \pm 0.4	10.2 \pm 0.9	17.6 \pm 1.5	21.6 \pm 3.2
L_D (nm)	\sim 56.6	\sim 32.0	\sim 17.7	\sim 13.5	\sim 12.2
NH ₃ time (s)	10	20	30	60	
n_D ($\times 10^{10} \text{ cm}^{-2}$)	23.2 \pm 1.2	3.9 \pm 1.5	4.8 \pm 2.9	5.5 \pm 1.4	
L_D (nm)	\sim 11.7	\sim 9.0	\sim 8.1	\sim 7.6	

AII. 2 Electrical doping effect in N-doped graphene

It is known that the incorporation of N atoms into the two-dimensional in-plane of graphene can vary in different configurations of pyridinic, quaternary and pyrrolic N, that exert distinct effects on the electronic structures and transport properties of graphene.^[1] Normally pyridinic and pyrrolic N p-dopes graphene while quaternary N introduces n-type doping in graphene. Of note, a weak n-doping effect can be found in hydrogenated pyridinic and pyrrolic N wherein the extra charge on N is forced into the delocalized carbon π -network.^[2] Quaternary N sites have been reported to act as a positively charged scattering center, which can enhance the electron-hole asymmetry in transport properties.^[3] Given the observed n-doping behavior as well as the symmetric G (V_g) curves, it is expected that hydrogenated pyridinic and/or pyrrolic N are the dominant configurations in the N-doped graphene of this study.

AII. 3 Working principle of graphene field effect transistor (GFET)

Using AgCl/Ag as the reference electrode, the gate voltage (V_g) is applied through the electrolyte solution (0.1 M KCl with 10 mM Tris, pH \sim 8). When V_g sweeps from negative to positive voltages, the dominant charge carriers in graphene correspondingly change from hole to electron as the Fermi level (E_F) of graphene shifts from the valence band to the conduction band. As a result, the conductance (G) of graphene demonstrate an ambipolar behavior with V_g in Figure 1c (black line). The voltage of the minimum conductance (G_{\min}) is called charge neutrality point (CNP) with equal concentrations of hole and electron carriers. The positive CNP (80 mV) for untreated graphene suggests a positive doping from the underneath epoxy substrate.

AII. 4 Reproducibility and reliability of the bilayer graphene on the GC disk

Raman spectroscopy and repeated ORR tests were performed to confirm the reliability and reproducibility of the bilayer graphene on the GC disk (RRDE graphene). The Raman spectra of monolayer and bilayer graphene on the GC electrode both show increased peak intensity of 2D peak compared to that of the bare GC (Figure AII. 4b). Especially the peak intensity ratio of I(2D)/I(G), an indicator of graphene layer number,^[4] is as high as 1.4 for bilayer graphene while below 1.0 for both monolayer graphene (0.75) and the GC (0.65). Therefore, we can conclude that bilayer graphene behaves more independently than monolayer graphene supported on GC. In addition, the well-overlapped LSV curves at 800 rpm obtained from two different bilayer graphene samples in Figure AII. 4c show a good reproducibility. Raman characterization of bilayer graphene before and after RRDE experiments (Figure AII. 4d) confirms the stability of bilayer graphene. As a result, bilayer graphene is used as a pristine surface on RRDE for further doping treatments and ORR catalysis.

AII. 5 Selectivity of RRDE graphene

1) Koutecky-Levich equation

At different rotation rates, the limiting current for oxygen reduction behaves according to the Koutecky-Levich equation^[5]:

$$\frac{1}{I} = \frac{1}{I_K} + \frac{1}{I_L} \quad (1)$$

where I is the observed current, I_K is the kinetic current that can be observed when the mass transport rate to the electrode is much greater than the reaction rate, I_L is the diffusion limited current that can be obtained when the reaction rates is much larger than the mass transport rate. The diffusion-limited current can be described by the Levich equation:

$$I_L = 0.62nFAD_o^{2/3}C_o\nu^{-1/6}\omega^{1/2} = BnA\omega^{1/2} \quad (2)$$

where n is the electron transfer number, F is the Faraday constant ($C \text{ mol}^{-1}$), A is the electrode area (cm^2), D_o is the diffusion coefficient of O_2 ($\text{cm}^2 \text{ s}^{-1}$), C_o is the concentration of O_2 in the electrolyte, ν is the kinematic viscosity ($\text{cm}^2 \text{ s}^{-1}$) and ω the rotation rate (rad s^{-1}). The equation can be simplified with the Levich constant defined as B . By performing rotating ring disk electrode (RRDE) experiments for ORR with a platinum disk electrode (Figure AII. 6a), B can be calculated using the slope of the

Koutecky-Levich plot (as platinum is known to be a 4-electron dioxygen reduction catalyst):

$$\text{slope} = \frac{1}{BnA} \quad (3)$$

The Koutecky-Levich plots in Figure 4f compares the activities for different RRDE graphene using the intersection at the axis of $1/I_{\text{disk}}$, which corresponds to the kinetics current (I_K). A higher I_K , a direct indicator of a higher catalytic activity, will be reflected by a value of the $1/I_{\text{disk}}$ intersection closer to zero. As expected, the co-doped sample N30-O10 shows the best ORR activity by intersecting with the $1/I_{\text{disk}}$ axis the closest to zero, while the low current values are found at the pristine and N30 samples as their $1/I_{\text{disk}}$ intersections are the furthest from zero.

2) Collection efficiency

The collection efficiency of rotating disk ring electrode (RRDE) was calculated based on the reversible redox reaction of potassium ferricyanide. In 0.1 M sodium perchlorate purged with argon, 1 mM potassium ferricyanide (III) was reduced at the glassy carbon disk to Fe(II) which can be re-oxidized at the platinum ring. Of note, the reversible hydrogen electrode (RHE) as the reference electrode in the Luggin capillary was only in contact with 0.1 M sodium perchlorate. As illustrated in Figure AII. 6b, the redox currents were recorded at both the disk and ring at different rotation rates ranging from 400 to 2000 rpm. Based on the currents, the collection efficiency ratio of the ring was determined as 22.5%.

AII. 6 References:

- [1] Y.-F. Lu, S.-T. Lo, J.-C. Lin, W. Zhang, J.-Y. Lu, F.-H. Liu, C.-M. Tseng, Y.-H. Lee, C.-T. Liang, L.-J. Li, *ACS Nano* **2013**, 7, 6522.
- [2] a) Z. Jin, J. Yao, C. Kittrell, J. M. Tour, *ACS Nano* **2011**, 5, 4112; b) T. Schiros, D. Nordlund, L. Pálová, D. Prezzi, L. Zhao, K. S. Kim, U. Wurstbauer, C. Gutiérrez, D. Delongchamp, C. Jaye, *Nano Lett.* **2012**, 12, 4025.
- [3] J. Li, L. Lin, D. Rui, Q. Li, J. Zhang, N. Kang, Y. Zhang, H. Peng, Z. Liu, H. Xu, *ACS Nano* **2017**, 11, 4641.
- [4] Y. Hao, Y. Wang, L. Wang, Z. Ni, Z. Wang, R. Wang, C. K. Koo, Z. Shen, J. T. Thong, *Small* **2010**, 6, 195.

- [5] A. J. Bard, L. R. Faulkner, J. Leddy, C. G. Zoski, *Electrochemical methods: fundamentals and applications*, wiley New York, **1980**.

Appendix III

Supporting Information for Chapter 4

AIII. 1 Materials and Methods

Plasma condition

A capacitively coupled plasma system with a radio-frequency (RF) of 40 kHz and a base pressure below 0.02 mbar (Diener electronic, Femto) was employed at room temperature. The power/pressure parameters used for controlled surface modifications were 10 W/1.0 mbar for hydrogen plasma and 8 W/0.85 mbar for argon plasma, respectively. Inside the plasma chamber, a perforated Faraday cage was used to shield energetic hydrogen ions to form a mild radical plasma to react with graphene.

(HR)TEM characterization

CVD graphene (Graphenea) was employed to prepare the samples. We deliberately opted for commercial graphene to assure reproducibility. Aberration-corrected high-resolution transmission electron microscopy (AC-HRTEM) imaging was conducted on an FEI Titan 80–300 microscope at an acceleration voltage of 80 kV (Ulm University). Transmission electron microscopy (TEM) images were collected on a Tecnai F20 microscope (Thermo-Fisher Scientific) operating at 200 keV (Leiden University Medical Center, LUMC).

TPD-IR characterization

The temperature programmed deposition-infrared spectroscopy (TPD-IR) was performed in a custom-made high vacuum system, comprising a central high vacuum chamber with a closed-cycle helium refrigerator mounted on top. Water deposition on a BaF₂ window mounted on the tip of a cold finger can be monitored using a Fourier Transform Infrared (FTIR) spectrometer. IR spectra in the range of 700–4000 cm⁻¹ and with a resolution of 1 cm⁻¹ were collected in transmission mode at normal incidence every 90 seconds. CVD graphene films were transferred onto the BaF₂ window via a biphasic method previously developed.^[1]

Near-ambient pressure (NAP)-XPS experiments

NAP-XPS spectra were recorded with a SPECS XPS spectrometer equipped with a monochromatic small-spot (300 μm) X-ray source, an Al anode (Al Kα= 1486.6 eV) and a 180° double-focusing hemispherical analyzer working with a multichannel 1D delay-line detector. XPS measurements at pressures of up to 20 mbar are possible due to a differential pumping system, which separates the electron analyzer (SPECS Phoibos NAP-150) from the reaction area via a nozzle with an aperture of 300 μm.

Filling of the NAP-cell with water vapor was performed by means of piezo-electric leak valve. The water reservoir was kept at room temperature. Further details about the design of the NAP-XPS cell can be found in literature.^[2] UHV measurements were conducted at a chamber pressure of $<10^{-9}$ mbar. XP spectra were processed by CasaXPS software using Shirley background subtraction.

Raman spectroscopy

Raman spectra were collected on a WITEC alpha300 R – Confocal Raman Imaging with a laser wavelength of 532 nm. Laser power was set to <2 mW to minimize potential damages from laser induced heating of the samples. All measurements were performed under ambient conditions at room temperature.

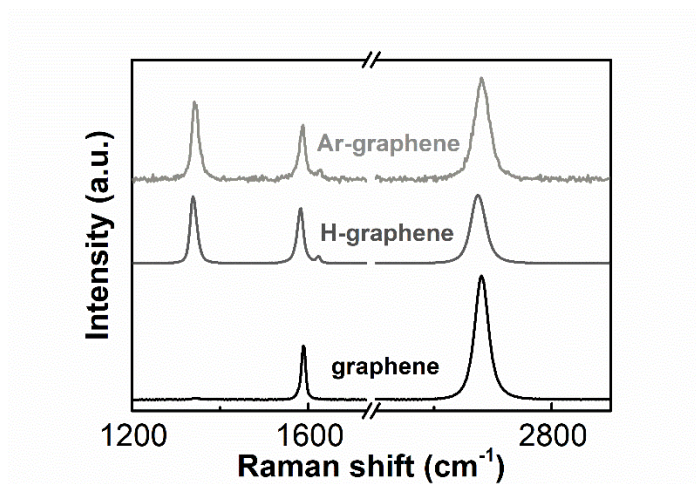


Figure AIII. 1 Raman spectra of graphene, H-graphene and Ar-graphene. Similar densities of hydrogenated and vacancy defects are confirmed by the peak intensity ratio between D (~ 1350 cm⁻¹) and G peaks (~ 1580 cm⁻¹). The spectra recorded using a 2.33 eV (532 nm) laser excitation are calibrated according to the G peak intensity.

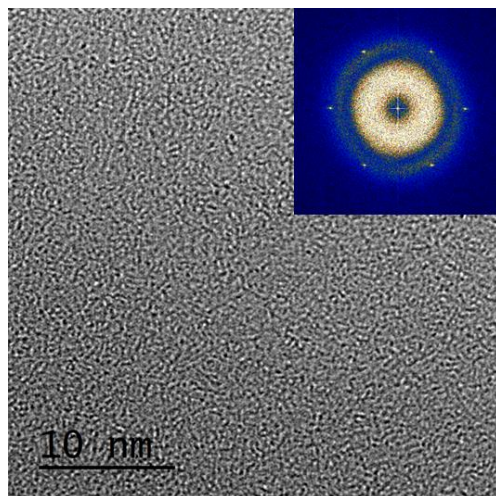


Figure AIII. 2 HRTEM images of pristine graphene. The amorphous patterns caused by the surface-adsorbed hydrocarbons cover all over the graphene lattice within the image views. The inset FET patterns of six reflections 4.7 nm^{-1} in a) suggest the good crystallinity of pristine graphene.

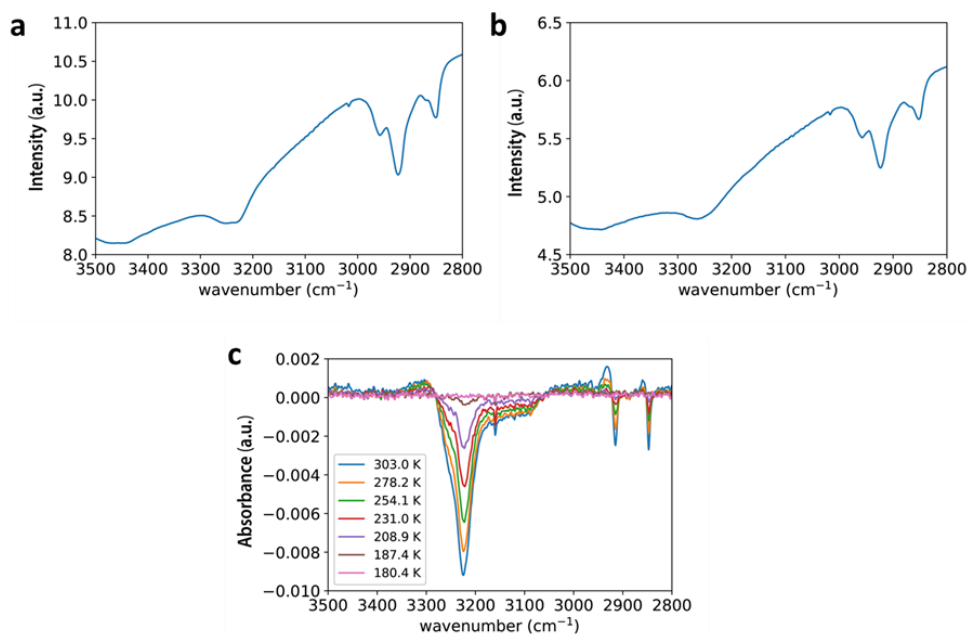
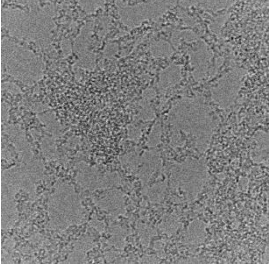

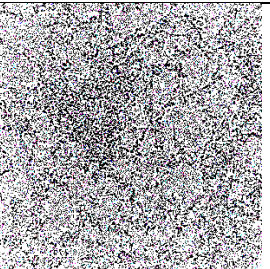
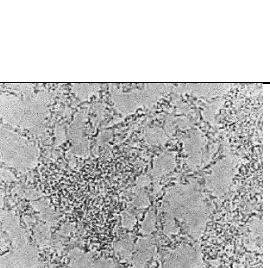
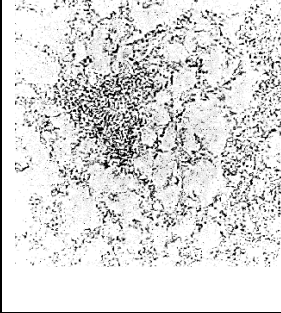
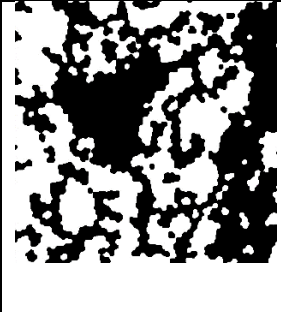


Figure AIII. 3 TPD-IR tests of water adsorption. a) Background spectra for pristine graphene. b) Background spectra for 60 s hydrogenated graphene. c) IR spectra during cooling down from room temperature to 180 K. The peak around 3250 cm^{-1} indicates water desorbed from H-graphene surfaces.

Table AIII. 1 Process flow for analyzing the images

	<p>Step 1: Conversion into a grayscale image The TEM image is converted into a grayscale image using the MATLAB built-in function <code>rgb2gray()</code>.</p>
	<p>Step 2: Adjusting of the contrast The goal of this step is to increase the contrast of the image and improve the visibility of small contaminations. Built-in <code>adapthisteq()</code> function of the MATLAB performs this task by contrast-limited adaptive histogram equalization.</p>
	<p>Step 3: Normalization of the image The goal of this step is to eliminate the effect of any intensity variations from image to image. The intensity of each pixel of the image after this transformation (y) is calculated by: $y = 255 \times \frac{(x-min)}{(max-min)}$ where: x: the gray scale initial intensity of the pixel min: minimum gray scale intensity for the original image. max: maximum gray scale intensity for the original image.</p>
	<p>Step 4: Denoising of the image Several MATLAB built-in functions including <code>imopen()</code>, <code>imclose()</code>, <code>imgaussfilt()</code> are used to remove the noise. Opening and closing operations remove random flipped pixels. The <code>imgaussfilt()</code> smoothens the image by filtering with a 2-D Gaussian function.</p>

	<p>Step 4: Conversion the <i>gray-scale</i> into the <i>binary</i> image</p> <p>With this conversion, all the pixels with the intensity greater than a threshold, calculated by the <code>adaptthresh()</code> function will be replaced by 1 (white color, corresponding to the clean graphene) and the pixels with lower intensities will be replaced by 0 (black, corresponding to contaminations). This operation is performed using the MATLAB built-in function <code>imbinarize()</code>.</p>
	<p>Step 5: Segmentation</p> <p>By using the built-in <code>open()/close()</code> functions (subsequent erosion and dilation operations) the extend of the contaminations is identified. A disk with the radius of 10 pixels is used as the structuring element to define the neighborhood. The cleanness of the image is eventually calculated as the sum of the number of the white pixels (clean graphene area) normalized by the total number of pixels.</p>

AIII. 2 MATLAB script to calculate the cleanness

```

%% Initialization

N = 50; % number of the images to be analyzed.
level= 0.50; % bw conversion treshold value.
size = 10;

report = zeros (N , 3);
shape = 'disk';

for sequence = 1: N
filename = num2str(sequence);
im = imread([filename, '.tif']);

image = rgb2gray(im); %rgb to gray conversion

InIimage = image;

%% improving the image

image = adapthisteq(image); % increasing the image contrast

image = uint8(255*mat2gray(image)); % normalization of the image

```

```

%% Noise removal

image = imclose(image,strel(shape,1));
image = imopen(image,strel(shape,1));

image = imgaussfilt(image, 2);

%% conversion to a binary mage

T = adaptthresh(image,level,'ForegroundPolarity','dark');
image = imbinarize(image, T);

%% segmentation

image = imopen(image, strel(shape,size));
image = imclose(image, strel(shape,size));

%% finalizing
clean = sum(sum(image == 1));
total = numel(image);

report(sequence, 1) = clean;
report(sequence, 2) = total;
report(sequence, 3) = clean*100/total;

figure, imshowpair(IniImage, image, 'montage'), title([filename, ':
cleanless:', num2str(report(sequence, 3)), '%,', ' ', size:', num2str(size), '
level:', num2str(level)]);
saveas(gcf,[filename, '_3rd_analyzed.jpg']);

clear image
clear im
clear IniImage
clear Image
end

figure, bar(report(:, 3));
figure, hist(report(:, 3));
Clenaliness = mode(report(:, 3));
display(Clenaliness);

```

AIII. 3 References

- [1] L. A. Belyaeva, W. Fu, H. Arjmandi-Tash, G. g. F. Schneider, *ACS Cent. Sci.* **2016**, *2*, 904.
- [2] L. Nguyen, F. Tao, *Rev. Sci. Instrum.* **2016**, *87*, 064101.

Appendix IV

Supporting Information for Chapter 5

AIV. 1 Materials and methods

Preparation of graphene samples

Graphene was grown in a CVD oven (nanoCVD system, Moorfield Nanotechnology, England). Briefly, the copper foil (Alfa Aesar, 99.999% purity, 25 μm thickness) was rapidly (in \sim three minutes) heated to 1035°C in the chamber and annealed under the continuous flow of hydrogen (20 standard cubic centimeters per minute, sccm) for 90 minutes. Graphene growth started upon the injection of methane ($\text{CH}_4:\text{H}_2$ ratio of 2:20) for 2 minutes; then the hot stage assembly cooled down under Ar environment. The size of the hot-stage of our CVD chamber allows the growth of the samples as large as 2.5 cm \times 4 cm; graphene on the backside of the copper foil was etched away upon the exposure to oxygen plasma while the front side was protected with a piece of aluminium foil, sealed at the edges with scotch tapes. Use of PMMA was avoided as PMMA left-over might increase the uncertainties in estimating the mechanical properties of graphene. The absence of the D peak in Raman spectroscopy of the front side of the randomly tested samples at this stage, confirmed the quality of the sealing. Graphene on copper sample was sectioned using a sharp blade into pieces of \sim 1 cm \times 1 cm to be used separately at different compression experiments.

Manipulating the lattice of graphene

Argon ion irradiation and hydrogenation of the graphene lattice were performed in a capacitively coupled RF plasma system operating at 40 kHz and 200 W power from Diener electronic. The base pressure of this system is below 0.02 mbar. Thorough flushing (3 to 5 times) of the chamber with the corresponding gas (0.9 mbar for argon and 1.0 mbar for H_2) before plasma process was necessary to ensure a high purity. The samples were placed in a vertical distance of \sim 3 cm away from the electrode and surrounded in a Faraday cage with grid to shield any potential bombardment from energetic ions in the plasma. The intensity of the plasma was controlled by tuning the power and pressure of the corresponding gas. The optimal parameters for controlled defect introduction are 20 W/0.9 mbar for Ar and 10 W/1.0 mbar for H_2 , respectively. For different experiments explained in the text, different irradiation durations ranging from 30 s to 15 min were used.

Photography

The area of graphene during the experiments was recorded by high resolution photos captured by a Canon Eos 100D photo camera (effective pixels: 18 megapixels, maximum resolution: 5184 \times 3456) equipped with a macro lens (Canon EF-S 60mm f/2.8 Macro USM). The camera was positioned perpendicular to the LB trough

(inspected by a spirit level) to minimize the calculation uncertainties. In the optimized condition, deformations as small as few micrometres in each side of the square graphene was detected by this optical set-up.

Image processing

Semi-automatic segmentation of the surface of graphene was performed by means of image registration using *elastix*.^[1] Mathematically, the registration problems are formulated as an optimization problem to find the optimum transform parameters that is best solution to map the fixed image domain to the moving image domain. The image at time = 0 was manually segmented and a template was created from this image. The template was the moving image here and all the subsequent images were counted as a fixed image. By registration, the manual segmentation of the first image can be mapped to other images. An affine transform with the cost function of mutual information was used, which was optimized by adaptive stochastic gradient decent over 1500 iterations.

Raman spectroscopy

Raman spectroscopy was performed at the ambient conditions using WITec alpha300 R confocal Raman microscope. The setup was equipped with a dual-axis XY piezo stage providing a minimum step size of 100 nm for sample positioning. Confocal Raman spectroscopy (532 nm excitation wavelength) was used to characterize the graphene samples transferred onto wafers. The laser power was limited to < 2 mW to prevent any laser induced heating of the samples. High resolution spectra were recorded using a 100x Zeiss EC Epiplan-Neofluar DIC objective (NA = 0.9) using 600 lines/mm and 2500 lines/mm spectrometer grating.

AIV. 2 Experimental setup

A commercial available, computer controlled and programmable Langmuir-Blodgett (LB) trough (Minitrough 2, KSV Instruments controlled by KSV Research Lab v2.01 software) was used to perform the compression experiments. Conventionally, the trough has been used to prepare Langmuir films of different molecules and deposit mono- and multilayers onto rigid substrates. Different components of the set-up are marked in Figure AIV.1. The trough has the dimensions of 320 mm × 75 mm × 10 mm. A micro-electronic feedback system controls the surface pressure which is measured based on the Wilhelmy principle, using a platinum plate connected to a sensitive balance. In a typical experiment, the trough was filled with 0.5 M solution of ammonium persulfate (APS) in water. The surface of the air-water interface was aspirated to minimize any contamination, indicated by the surface pressure < 0.2

mN/m after full compression. A piece of graphene sample on copper foil ($\sim 1 \text{ cm} \times 1 \text{ cm}$) was placed on surface of APS solution, surrounded with 1,2-dipalmitoyl-*sn*-glycero-3-phosphocholine (DPPC) molecules after dropwisely depositing 1 g/L solution of DPPC lipids (Avanti Polar Lipids Inc.) in $\text{CHCl}_3/\text{CH}_3\text{OH}$ (3:1 volumetric ratio) at the air/water interface with a precision needle mounted on a glass syringe. To prevent large movements of the sample during the copper etching and later, a cage composed of a few wires (with the diameter of few hundreds of micrometres) was implanted in and sticking-out of the Teflon block at the bottom of the trough. A high resolution camera is focused perpendicularly on the sample to record its deformation during the experiments.

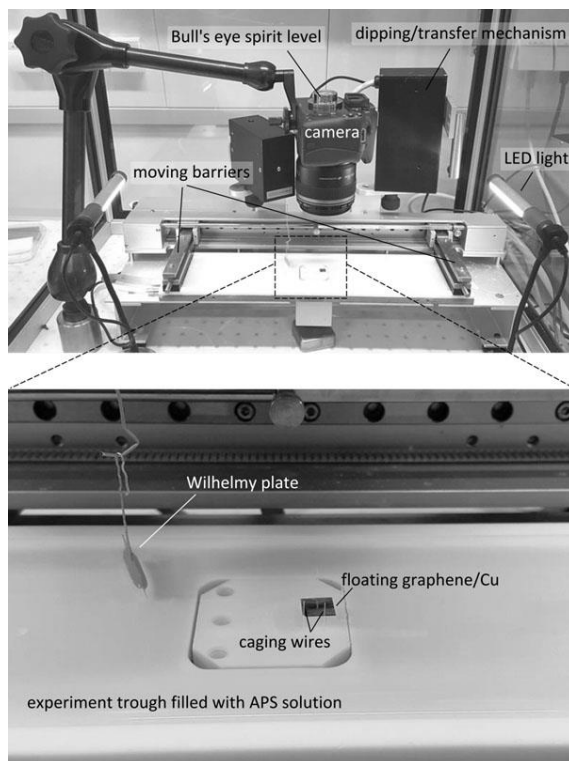


Figure AIV. 1 Experimental setup. The Langmuir–Blodgett trough customized and used for the experiments in this report: different components are marked on the photos.

The copper foil was etched away in ~ 30 minutes yielding graphene floating at the air-water interface. A slight increase of the surface pressure ($\leq 1 \text{ mN/m}$) was observed after the copper etching. Next, two parallel hydrophilic barriers made of Delrin, slightly immersed in the liquid subphase, were moved towards each other. Depending on the specific test, the barrier displacement rates ranged from $\sim 1 \text{ mm/min}$ to 12

mm/min. The Wilhelmy plate, positioned close to the center of the trough, was used to measure the surface pressure. The plate was oriented parallel to the barriers. The LB trough was mounted on an anti-vibration table to limit the effect of external vibrations. The experiments were performed under ambient conditions ($21\text{ }^\circ\text{C} < T < 23\text{ }^\circ\text{C}$) and humidity level.

AIV. 3 Size-dependent in-plane elastic properties of graphene

Monte Carlo simulations demonstrated that the elastic properties of graphene in the presence of anharmonic coupling the in-plane and out-of-plane displacements are highly size dependent.^[2] Particularly the equilibrium bulk modulus of graphene vanishes with the graphene size as $L^{-0.323}$ following the relation:

$$k = \frac{193.6 - 9.1 \times 10^{-2} L^2 + \frac{457.6 \left(\frac{L}{14.14}\right)^4}{L^{0.325}}}{1 + \left(\frac{L}{14.14}\right)^4} \quad (1)$$

Here L is the length (in \AA) and k is the bulk modulus (in N/m) of graphene sample. Bottom inset Figure 1-c superimposes the theoretical and experimental results. Obviously, the size dependency of k can largely explain the considerably low (with respect to earlier reports^[1,3]) in-plane stiffness measured in this work. The median k of our samples, however is slightly above the theory expectation. The suppression of the anharmonicity due to the defects in CVD graphene (as reported previously^[3b]) may account for this discrepancy.

AIV. 4 Graphene buckling: blistering or wrinkling

In the process of buckling, thin films delaminate from the surface of *rigid* substrates and form blisters. Similar scenario may happen on the surface of liquids provided that the film/substrate adhesion is small enough; Otherwise the liquid substrate may deform together with the film to form wrinkles. More precisely, the competition between the work of a hydrostatic pressure of the liquid (following the deformation of the film) and surface energy cost to delaminate the film (assuming that the film remains wet after the delamination) determines which buckling mechanism is in action. Wagner et al studied the compression driven bulking of an elastic film floating on a liquid surface;^[4] They introduced a dimensionless parameter Γ/δ^2 ($\Gamma \equiv \gamma\lambda/D$ and $\delta \equiv \rho_{st}/\rho_l L$, the parameters are explained in Table AIV.1) which sets the critical blister size at the onset of the blistering. Particularly for $\Gamma/\delta^2 \gg 1$ (our case), their model

predicts a blistering size of ~ 10 cm, larger than the sample size implying that blistering is impractical for our samples.

Table AIV. 1: parameters involved in calculating the critical blister size, based on the model proposed by Ref (5)

L [m]	1×10^{-2}	initial length of the sample
t [m]	3×10^{-10}	thickness of graphene
ρ_l [kg/m ³]	1×10^3	density of water
ρ_s [kg/m ³]	2.2×10^3	density of graphene
D [N m]	1×10^{-12}	flexural rigidity of graphene
g [m/t ²]	9.8	gravity acceleration
γ [N/m]	7.3×10^{-2}	surface tension of water
λ [m]	1×10^{-4}	intrinsic wavelength of wrinkles = $(D/ \rho_l g)^{1/4}$

AIV. 5 Molecular dynamics simulations

The dynamical response of a monolayer graphene subject to compression was stimulated by means of large scale atomic/molecular massively parallel simulator (LAMMPS).^[5] Adaptive intermolecular reactive empirical bond order (AIREBO) potential^[6] was chosen to describe interatomic interactions between C-C and C-H pairs. Water molecules have been modelled by the four-point TIP4P potential^[7] with the H-O bond length of 0.9572 Å and the H-O-H bond angle of 104.52°. The interaction between atoms accounts for both Coulomb and Van der Waals contributions. To describe the latter, a 6-12 Lennard-Jones (LJ) potential was employed, $4\epsilon_{ij} \left[\left(\frac{\sigma_{ij}}{r} \right)^{12} - \left(\frac{\sigma_{ij}}{r} \right)^6 \right]$, with parameters $\epsilon_{OO} = 0.1627$ kcal/mol and $\sigma_{OO} = 3.1643$ Å. The long-range electrostatic interactions were calculated using the particle-particle particle-mesh (PPPM) method. Van der Waals interactions between water molecules and hydrogenated graphene films were characterized by LJ parameters $\epsilon_{CO} = 0.0927$ kcal/mol and $\sigma_{CO} = 3.2830$ Å,^[8] and $\epsilon_{OH} = 0.0749$ kcal/mol and $\sigma_{OH} = 2.9071$ Å, where the latter two parameters were obtained from the Lorentz-Berthelot combining rules.

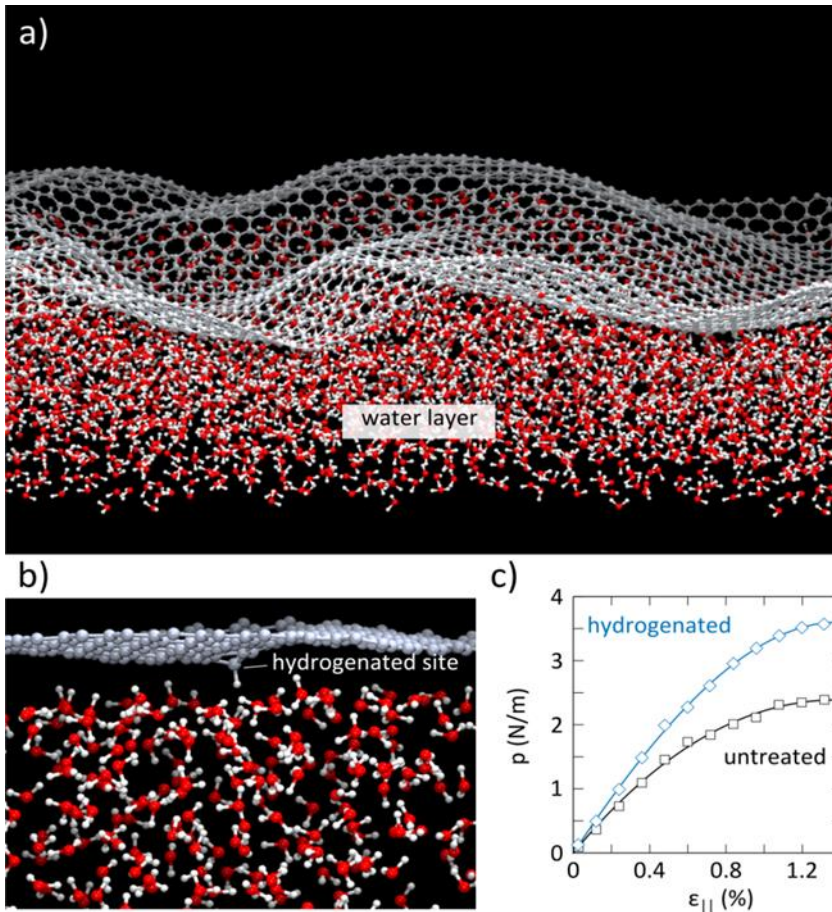


Figure AIV. 2 Molecular dynamics simulation of graphene/water interplay. a) Heavily wrinkled graphene on the surface of water: water molecules follow the undulations of graphene and no delamination is observable. The snapshot corresponds to $\epsilon > \epsilon_{cr}$ region. b) Hydrogenated graphene on the surface of water: interaction between the hydrogenated site and water molecules locally stabilizes the corresponding carbon atom. The snapshot corresponds to $\epsilon < \epsilon_{cr}$ region. c) Evolution of the stress-strain diagram as a result of the hydrogenation: hydrogenation improves the young's modulus by 1.35 times. The concentration of hydrogenated sites (10^{12} cm^{-2}) in the simulations is similar to the experimentally measured values.

The modeled untreated graphene consist of 3936 carbon atoms spanning roughly square area of $10 \times 10 \text{ nm}^2$. Addition of a single hydrogen atom to this model provides a hydrogen density of 10^{12} cm^{-2} , corresponding to the experimentally measured density for hydrogenated graphene. A relatively thick layer of water molecules with height $h_w = 16.7 \text{ \AA}$ encloses the bottom subspace, from which the lowest water molecules have been kept rigid. Periodic boundary conditions were imposed along the two orthogonal directions parallel to the graphene. Initial equilibration run was

performed under isobaric and isothermal conditions (at room temperature and zero pressure) for 10 ps. The compression process starts by applying a homogeneous biaxial strain with constant rate 0.04 %ps⁻¹ within NVT simulations. In all our molecular dynamics simulations, a time step of 1 fs has been used for the velocity-Verlet integrator.

In agreement with the analytical results (see section AIV. 4), the molecular dynamics simulations confirm the absence of blistering in our system (Figure AIV. 2a). Indeed the water molecules follow the undulations of graphene throughout the compression process and no delamination is detectable. Hydrogenation of graphene, on the other hand, locally stabilizes the sheet around the hydrogenated site, implying locally stronger interaction with underlying water molecules (Figure AIV. 2b). The interaction significantly affects the stiffness of graphene (Figure AIV. 2c), resulting in higher bulk modulus than for graphene by a factor of 1.35.

AIV. 6 Flexural rigidity of graphene

Flexural rigidity of graphene governs the onset of buckling. Particularly with Euler's buckling formulation, the critical strain of an square sample reads:

$$\varepsilon_{|cr} = \frac{\pi^2 D}{a^2 E_{2D}} \left(m + \frac{1}{m} \right)^2 \quad (2)$$

Here a is the length (= width), D is the flexural rigidity, E_{2D} is the two-dimensional Young's modulus and m is the number of half waves created upon buckling of the sample. Accordingly the fitting $\varepsilon_{|cr} = \frac{\alpha}{(E_{2D}/\beta)}$ ($\alpha = 0.027$ N/m, $\beta = 1$ for untreated samples) in Figure 1d reveals D :

$$D = \frac{\alpha a^2}{\pi^2 \left(m + \frac{1}{m} \right)^2} \quad (3)$$

The graphene sample strained up to the onset of buckling ($\varepsilon \sim \varepsilon_{cr}$) features numerous horizontal and vertical undulations, separated in $\lambda/2 \sim 50$ μm range providing an estimation for m : $m = a/(\lambda/2) \sim 200$. Accordingly the equation above suggests D in the order of 10^{-12} N m (10^6 eV). This value is six orders of magnitude higher than that for graphene as-grown on Cu(111) recently probed by helium atom scattering (HAS),^[9] which can be mainly ascribed to the higher levels of out-of-plane undulations of strain-free graphene floating on water compared to the heavily strained graphene on copper substrate.^[10] Moreover, the sizes of the graphene samples (1 cm² vs 1 mm²) can also contribute to the difference in bending rigidity as the undulations magnitudes

increase with the size of graphene. In consequence, high levels of undulations lead to the increased thickness of graphene and thus its bending rigidity.

Numerous half waves observed in our sample is due to the interaction of the graphene with liquid substrate which stabilizes the sheet at high energy levels. Notably in the absence of water, graphene samples would form only one large buckle ($m = 1$). In this case equation (2) with our estimated flexural rigidity predicts a critical buckling force of 10^{-10} N order which is the same order of the weight of our graphene piece. In other words vertically standing graphene walls would be highly unstable and may collapse by its own weight.

AIV. 7 Strain distribution in crumpled graphene

In details, the deformed graphene was transferred onto an oxidized silicon wafer after being compressed up to 60 mN m^{-1} . Figure AIV. 3a-d present optical micrograph, atomic force microscopy (AFM) and Raman 2D peak position mappings of a selected window of the transferred graphene sample to characterize the strain distribution following the conformation of the wrinkles in crumpled graphene. As shown in Figure AIV 3, the strain field is inhomogeneous and strain is largely concentrated at heavily crumpled wrinkles where the 2D peak is upshifted. The flat areas, in contrast, exhibit a negligible strain as the 2D peak position averages to $\sim 2675 \text{ cm}^{-1}$, an standard value for unstrained graphene.^[11] A careful examination of the strain distribution highlights the complex role of the morphology of deformations. Surprisingly, the straight wrinkles (some marked by ☆ in Figure AIV. 3b-c) exhibit negligible contrast with the nearby graphene (background) in the Raman mapping. Those wrinkles are wide enough to be probed by Raman as even narrower but curly wrinkles (such as the one marked by □ in Figure AIV. 3c) are captured with the optics. Gauss's Theorema Egregium assertion expresses the correlation between the morphology and the strain surfaces.^[12] The assertion states that straight wrinkles with a single Gaussian curvature identical to flat graphene can exist without any strain. In contrast, for wrinkles with double (multiple) curvatures which are always strained. As unfolding such deformations demands the application of a tensile force, the strain is locked into the heavily crumpled regions (and spreads on neighboring regions) in graphene. The same postulation explains the observed upshift in the 2D peak position along the transition from the marginal (dominant uniaxial compression, featuring straight wrinkles) to the central (biaxial compression with heavily crumpled wrinkles) zones, when the zones are distinguishable (Figure AIV. 3e).

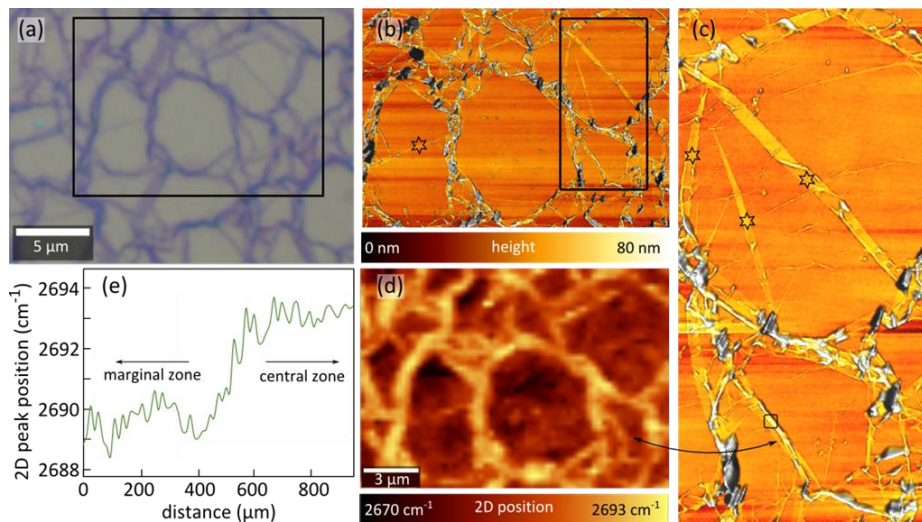


Figure AIV. 3 Strain distribution in crumpled graphene samples. a) Optical micrograph featuring a network of heavily crumpled ridges in graphene. b) AFM mapping of the rectangular window marked in a). c) Zoomed-in AFM mapping of the rectangular window marked in b). d) Two-dimensional map of the position of the Raman 2D peak of graphene, corresponding to the same area in b). e) Line map of the position of the Raman 2D peak of graphene. The low magnification optics (5x) used in this mapping averages the signal over the spot size of $\sim 5.5\mu\text{m}$.

AIV. 8 References

- [1] A. Zandiatashbar, G.-H. Lee, S. J. An, S. Lee, N. Mathew, M. Terrones, T. Hayashi, C. R. Picu, J. Hone, N. Koratkar, *Nat. Commun.* **2014**, 5, 3186.
- [2] J. Los, A. Fasolino, M. Katsnelson, *Phys. Rev. Lett.* **2016**, 116, 015901.
- [3] a) C. Lee, X. Wei, J. W. Kysar, J. Hone, *science* **2008**, 321, 385; b) G. López-Polín, C. Gómez-Navarro, V. Parente, F. Guinea, Mikhail I. Katsnelson, F. Pérez-Murano, J. Gómez-Herrero, *Nat. Phys.* **2014**, 11, 26.
- [4] T. J. W. Wagner, D. Vella, *Phys. Rev. Lett.* **2011**, 107, 044301.
- [5] S. Plimpton, *J. Comput. Phys.* **1995**, 117, 1.
- [6] S. J. Stuart, A. B. Tutein, J. A. Harrison, *J. Chem. Phys.* **2000**, 112, 6472.
- [7] J. L. F. Abascal, C. Vega, *J. Chem. Phys.* **2005**, 123, 234505.
- [8] a) R. R. Nair, H. A. Wu, P. N. Jayaram, I. V. Grigorieva, A. K. Geim, *Science* **2012**, 335, 442; b) P. Hirunsit, P. B. Balbuena, *J. Phys. Chem. C* **2007**, 111, 1709.

- [9] A. Al Taleb, H. K. Yu, G. Anemone, D. Fariás, A. M. Wodtke, *Carbon* **2015**, 95, 731.
- [10] L. A. Belyaeva, L. Jiang, A. Soleimani, J. Methorst, H. J. Risselada, G. F. Schneider, *Liquids relax and unify strain in graphene*, *Nat. Commun.* **2020**, manuscript in press.
- [11] G. Tsoukleri, J. Parthenios, K. Papagelis, R. Jalil, A. C. Ferrari, A. K. Geim, K. S. Novoselov, C. Galiotis, *Small* **2009**, 5, 2397.
- [12] T. A. Witten, *Rev. Mod. Phys.* **2007**, 79, 643.

Appendix V

Supporting Information for Chapter 6

AV.1 Materials and Methods

Plasma condition

A capacitively coupled plasma system with a radio-frequency (RF) of 40 kHz and a base pressure below 0.02 mbar (Diener electronic, Femto) was employed at room temperature. The power/pressure parameters used for controlled surface modifications were 10 W/1.0 mbar for hydrogen plasma and 16 W/0.85 mbar for ammonia plasma, respectively. Inside the plasma chamber, a perforated Faraday cage was used to shield energetic hydrogen ions to form mild radical plasmas to chemically functionalize the graphene.

Raman characterization

Raman spectroscopy and mapping were collected from CVD graphene on SiO₂/Si substrate (transferred via the PMMA assisted method). The Raman spectrometer used is a WITEC alpha300 R – Confocal Raman Imaging with a laser wavelength of 532 nm. To minimize the potential damage from laser heating effect, the laser power was controlled under 1.1 mW. All of the measurements were performed under ambient conditions at room temperature.

Gas detection experiment

A gastight epoxy chip carriers was used to support the GFET devices, which were placed in a Teflon flow cell. A poly-(dimethylsiloxane) (PDMS) ring was employed to tightly seal the cell. Under the control of mass-flow controllers (MFCs), ethylene, carbon monoxide and ethanol gas (1% in synthetic air) were further diluted with synthetic air (79% N₂ and 21% O₂) to reach different concentrations.

Lock-in technique

A lock-in amplifier (HF2LI, Zurich Instruments) was used to measure the signals with very narrow bandpass filters (~1 Hz). A sinusoidal alternating voltage with an amplitude of ~10 mV was applied to the GFETs via the source and drain electrodes. The changes of GFETs resistance versus time were monitored using the ZiControl (Zurich Instruments) program. Prior to each measurement, a noise frequency sweep was performed to determine the testing frequencies with minimum noise power spectrum density and thus to optimize the signal-to-noise ratio.

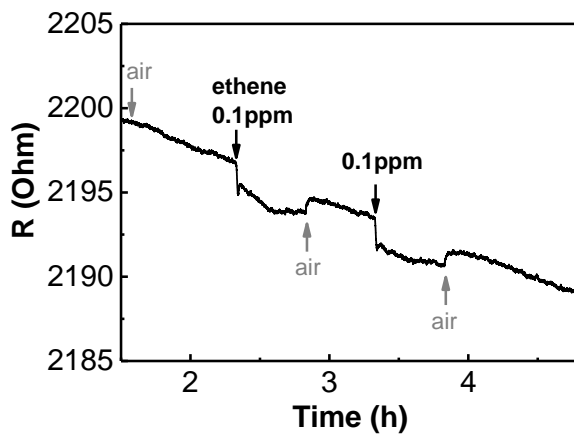


Figure AV. 1 The raw signal from a GFET device upon 0.1 ppm ethylene detection. The sheet resistance exhibits a drifted baseline upon the air exposure. A sharp spike appears due to the initial introduction of 0.1 ppm ethylene, followed by a drop in the signal that stabilizes at a new baseline. Air flush again brings the baseline back to the initial one. A repetitive exposure to ethylene and air gives reproducible results. All the measurements were done at room temperature.

Samenvatting

Geavanceerde toepassingen van grafeen vereisen een hoge kwaliteit, met een oppervlak waarvan de chemische samenstelling goed gedefinieerd is. De intrinsieke hoge elektronenmobiliteit van grafeen, het lage niveau van elektrische ruis en een uniforme kristalstructuur zijn onontbeerlijk voor hoogwaardige elektronische toepassingen. Chemische functionalisering van grafeen maakt het mogelijk om het grafeenvlak te gebruiken als detector. In dit proefschrift onderzoek ik aanpassingen van de oppervlakchemie van enkellaags grafeen, en de impact hiervan op de elektrische en elektrochemische eigenschappen voor toepassingen in detectie. Om de chemische samenstelling (en daarmee de elektronische eigenschappen) van grafeen te beïnvloeden, zijn systematisch heteroatomen zoals waterstof, stikstof en zuurstof in het grafeen geïntroduceerd als onderbrekingen van het kristalrooster. In het bijzonder is gekeken naar het samenspel van elektronentransport in het vlak en elektrochemische activiteit van het grafeenoppervlak, door het manipuleren van de dichtheid van H-sp³ defecten. Daarbij is gebleken dat de elektronische structuur van grafeen bepalend is voor de elektrische en katalytische eigenschappen van het oppervlak. Daarom is de elektrokatalytische reductie van zuurstof uitgevoerd op enkellaags grafeen gedoopt met stikstof om de actieve katalytische centra te vinden. Het delicate grafeenoppervlak is bijzonder gevoelig voor verontreinigingen, welke de intrinsieke actieve elektrochemie verhinderen door het kristalrooster af te dekken. Het is duidelijk geworden dat waterstof-behandeling verontreinigingen verwijdert en het oppervlak schoon houdt, door een beschermende laag van geabsorbeerd water te vormen (Hoofdstuk 4). Voorts blijkt dat de interactie van grafeen met het onderliggende support van invloed is op de intrinsieke eigenschappen van grafeen. Onderzoek naar de biaxiale compressie van centimeter-grote stukken grafeen drijvend op een wateroppervlak heeft uitgewezen dat defecten ook van significante invloed zijn op de mechanische eigenschappen van grafeen (Hoofdstuk 5). De geïntroduceerde H-sp³ defecten gaan interacties aan met de onderliggende watermoleculen om de bijbehorende koolstofatomen te stabiliseren, met een hogere rigiditeit in het vlak als gevolg. Ten slotte zijn gassensoren ontwikkeld gebaseerd op gehydrogeniseerd en genitrogeniseerd grafeen, en getest om de invloed van chemische functionalisering op detectievermogen te onderzoeken.

Hoofdstuk 2 laat zien hoe elektronische eigenschappen en elektrochemische activiteit elkaar beïnvloeden in enkellaags, gehydrogeneerd grafeen. Waterstofatomen werden geïntroduceerd in het kristalrooster door middel van radicaal waterstofplasma, om de chemische en elektronische eigenschappen van grafeen te moduleren. Raman

spectroscopie werd gebruikt om de toenemende dichtheid van sp^3 -defecten te volgen ten gevolge van hydrogenatie. In tegenstelling tot de typische afname van elektronenmobiliteit en minimale geleiding van grafeen normaal voor hydrogenatie, werd er een toegenomen geleiding en elektrochemische activiteit waargenomen na de eerste seconde van blootstelling aan radicaal waterstofplasma. Deze toename wordt toegeschreven aan het verwijderen van koolwaterstoffen die het oppervlak van het grafeenrooster bedekten. Daarnaast is de kwantumcapaciteit in grafeen onderzocht, een effect dat zijn oorsprong vindt in de lage toestandsdichtheid op het Diracpunt, en inzicht geeft in de interacties tussen elektrische en elektrochemische eigenschappen. Door de toestandsdichtheid met de elektrochemische activiteit te correleren, is geconcludeerd dat de elektrochemische kinetiek van grafeen in sterke mate afhankelijk is van de toestandsdichtheid nadat gehydrogeneerde defecten – zelfs in lage dichtheid – zijn geïnduceerd.

In hoofdstuk 3 is gekeken naar stikstof-doping in enkellaags grafeen, in verband met de elektrokatalyse van de zuurstofreductiereactie. De twee belangrijkste dopingsvormen van stikstofatomen, pyridinisch en grafitisch, zorgden voor n-doping van grafeen. Bij hoge gehalten van nitrogenering bleken stikstofdefecten te clusteren in domeinen, waardoor ook de bijbehorende oxidatiegraad van het oppervlak verhoogd werd. De twee kanten van grafeen gesynthetiseerd door de “chemical vapor deposition” technique, zullen in het vervolg benoemd worden als “zuiver” grafeen (dit is de kant die raakt aan het groeisubstraat) en “RRDE” grafeen (de kant die raakt aan de lucht). Beide kanten zijn gebruikt in de zuurstofreductiestudie. Zuiver grafeen, met minimale oppervlakteoxidatie, vertoonde een verlaagde stroomdichtheid tijdens zuurstofreductie bij verhoogde stikstofdoping. RRDE-grafeen is meer geoxideerd door blootstelling aan lucht tijdens de veroudering van het grafeen wat leidde tot een verbeterde activiteit in zuurstofreductie bij verhoogde stikstofdoping. Hieruit werd geconcludeerd dat niet stikstof, maar enkel gebonden zuurstofgroepen bepalend zijn voor verbeterde stroomdichtheid bij zuurstofreductie.

Zoals eerder gesteld is het grafeenoppervlak gevoelig voor verontreinigingen in de lucht, die de oppervlakte-eigenschappen zoals elektrochemie en bevochtiging significant kunnen veranderen. Hoofdstuk 4 demonstreert een effectief en niet-invasief protocol voor het schoonmaken van het grafeenoppervlak. In vergelijking met onbehandeld grafeen en argon-behandeld grafeen is gehydrogeneerd grafeen schoner, met verminderde bedekking door amorfe vervuiling ten gevolge van koolwaterstofdepositie uit de lucht. Tevens blijkt dat gehydrogeneerd grafeen een hogere affiniteit heeft voor geabsorbeerd water in vergelijking met onbehandeld grafeen.

Hoofdstuk 5 beschrijft de mechanismen waardoor centimetergroot grafeen zijn natuurlijke vorm behoudt wanneer het drijft op water. Onder biaxiale druk door een omringende laag van lipiden in een Langmuir-Blodgett trog wordt grafeen gedeformeerd (zowel elastische als plastisch) door de druk die wordt uitgeoefend op het kristalrooster. De stijfheid van grafeen wordt gekarakteriseerd in termen van de Young-modulus (E_{2D}). De stijfheid van grafeen was twee ordegrottes kleiner dan vlak grafeen, door een anharmonische benadering voor de totale elastische energie. De anharmonische benadering koppelt de strek- en flexmodes in tweedimensionale materialen. De gevonden Young-modulus was 1.5 maal groter. Deze verbetering in stijfheid werd toegeschreven aan de lokalisering van de flexmodes bij lange golflengtes door H- sp^3 defecten in het rooster. Anderzijds verlaagde de toevoeging van vacancy-defecten de kritische stress van grafeen, wat zelfs bij een verwaarloosbaar lage oppervlakedruk leidde tot de afbraak van grafeen.

Hoofdstuk 6 beschrijft de detectie van gassen middels het zogeheten *field effect* van gehydrogeneerd en genitrogeneerd grafeen. Het introduceren van chemische functionaliteiten verbetert de gevoeligheid door het moduleren van het dopingeffect en de adsorptieaffiniteit van gasmoleculen. Positieve doping is positief gecorreleerd met de elektrische response, terwijl negatieve doping resulteerde in een verlaagde response. Tijdens dynamische gasdetectie produceerde de grafeensensors een verzadigd en vervolgens verminderde response bij verhoogde gasconcentraties. Dit wordt verklaard door de consumptie van het beperkte aantal actieve plekken in grafeen als gevolg van het vasthouden van gasmoleculen. Ter vergelijking, gehydrogeneerd grafeen laat een veel betere gevoeligheid zien met minder verzadigingseffect dan genitrogeneerd grafeen. De beperkte gevoeligheid van beide grafeensensoren kan, worden toegeschreven aan het beperkte aantal specifieke interacties van de chemische functionaliteiten met de doelgasmoleculen.

Een grafeenoppervlak is een robuust en flexibel platform voor elektrische en elektrochemische sensor-applicaties. Het werk in dit proefschrift biedt belangrijke inzichten aangaande het manipuleren van de oppervlaktechemie en de mechanische eigenschappen van monolaag grafeen. Introductie van chemische defecten in het grafeennetwerk biedt grote mogelijkheden om, onder andere, de elektrochemische activiteit, ladingsdoping en adsorptiegedrag aan het oppervlak te moduleren, welke nauw verwant zijn aan het sensoreigenschappen. Oppervlakte verontreinigingen en oxidatie van grafeen tijdens het werken, en het verouderen van monsters kunnen een significante invloed hebben op de elektrische en elektrochemische eigenschappen ervan. De schoonmaakprocedure welke in dit proefschrift beschreven is biedt niet alleen een praktische strategie voor elektronmicroscopietoepassingen van grafeen,

maar biedt tevens fundamentele inzichten in de fysische chemie van het grafeenoppervlak.

Voor gehydrogeneerd grafeen is het de moeite waard om nog verder de mogelijkheden te onderzoeken voor het gebruik ervan als een platform voor oppervlak/grensvlak gerelateerde studies. Schoon, hydrofiel, mechanisch robuust grafeen is aantrekkelijk voor de (cryo-)elektronmicroscopie en de studie van (bio)-grensvlakken. Voor GFET-toepassingen is de hoge mobiliteit van grafeen na matige hydrogenering redelijk behouden, terwijl de elektrochemische lekstroom drastisch verminderd is. Bovendien maakt de elektrochemische activiteit na milde hydrogenering een ideale tweedimensionale elektrode met een lage capacitatieve achtergrondstroom en een breed potentiaalbereik. De studie van de elektrokatalytische eigenschappen van genitrogeerd grafeen laat zien dat een monolaag van grafeen een robuust en functioneel oppervlak biedt voor het lokaal bestuderen van reacties met behulp van *operando* technieken. Daarnaast kunnen oppervlaktekarakteristiektechnieken zoals Raman en infrarood spectroscopie gebruikt worden om systematisch de subtiele veranderingen van de chemie van het grafeenoppervlak te volgen en te correleren aan mechanismen van elektrokatalytische reacties zoals, bijvoorbeeld, de ORR en waterstof evolutie reactie.

Een groot probleem met polykristallijn CVD geproduceerd grafeen is de onvermijdbare oxidatie en atmosferische verontreiniging ervan, welke gepaard gaat met verlies van de elektrische eigenschappen, wat bekend staat als “veroudering” van het grafeen. Domeingrootte en het aantal *grain boundaries* in CVD grafeen zijn waarschijnlijk de veroorzakers van dit verouderingsproces. Volgens recente experimentele bevindingen in Leiden is CVD grafeen met kleinere kristallijne domeinen gevoeliger voor oxidatie aan de lucht en elektrische degradatie. Voor afdoende gevoelige en stabiele grafeen-gebaseerde sensor applicaties is monokristallijn grafeen dus noodzakelijk.

Het oppervlak van grafeen heeft ook na chemische functionalisatie een beperkte gevoeligheid en lage selectiviteit voor de detectie van gasmoleculen, zoals beschreven in Hoofdstuk 6. Om een ultra-hoge gevoeligheid en selectiviteit te bereiken, moeten selectieve interacties gebruikt worden zoals, bijvoorbeeld, antigeen-antilichaam interacties of functionalisatie met specifieke biomarkers. Diazonium chemie verbreedt het aantal mogelijkheden voor het selectief en gecontroleerd modificeren van het grafeenoppervlak. Ondanks het verlies van mobiliteit tot bepaalde niveaus kan diazonium-gefunctionaliseerd grafeen fungeren als een gevoelig en selectief GFET gebaseerde sensor applicatie.

Curriculum Vitae

Lin Jiang was born in Rizhao, Shandong province, China, on September 16th in 1988. In 2007, she graduated from Rizhao Experimental High School and enrolled as a bachelor student in marine science at Qingdao University of Science and Technology. In 2011, Lin graduated with her thesis entitled “Recycling and utilization of purified terephthalic acid” under the supervision of Prof. Dr. Kongcheng Hu. Lin continued her master study at Shanghai University under the supervision of Prof. Dr. Yaping Ding. Her research program focused on the fabrication of electrochemical biosensors based on novel graphene nanocomposites. As a master student, Lin received the “National Scholarship” and “Elite Student” Award from Shanghai University.

In 2014, Lin was granted a Chinese Scholarship Council scholarship (L.J., 201406890016) to start her PhD studies in the research group of Dr. Grégory F. Schneider in the department of Supramolecular & Biomaterials Chemistry (SBC) at Leiden University. During her PhD study, Lin collaborated with Dr. Yuvraj Birdja and Prof. Dr. Marc T. M. Koper on the electrochemical activity of hydrogenated graphene. With Bas van Dijk, M.Sc. and Dr. Dennis G. H. Hetterscheid, Lin further expanded her knowledge on the electrocatalysis of oxygen reduction reaction (ORR) using nitrogenated graphene. She also collaborated with Dr. Jiao and Prof. Dr. Harold Linnartz, Laboratory Astrophysics of Leiden University, as well as with Dr. Longfei Wu and Dr. Jan P. Hofmann, Eindhoven University of Technology, on the surface chemistry of graphene. In 2019, Lin was selected as a young editorial board of Chinese Chemical Letter (CCL, IF = 3.839). Lin was the co-founder of the Leiden Science China community, a student association in Leiden University aiming at strengthening connections between international students.

The results reported in this thesis were presented at several national and international conferences as listed below:

- NWA startimpuls workshop, Den Haag, the Netherlands, **invited talk** (13 September 2019).
- KNCV Electrochemistry Symposium, Groningen, the Netherlands, **invited talk** (23 November 2018).
- Graphene Week 2017, Athens, Greece, **contributing talk** (25-29 September 2017).
- Young Scholars Forum of Sun Yat-Sen University 2017, Guangzhou, P.R. China, **invited talk** (16-18 June 2017).

- 1st European Conference on Chemistry of Two-Dimensional Materials (Chem2DMat), Strasbourg, France, **contributing talk** (22-26 August 2017).
- CHAINS Conference 2017, Veldhoven, the Netherlands, **Best Poster Award** (5-7 December 2017).
- CHAINS Conference 2016, Veldhoven, the Netherlands, **poster** (6-8 December 2016).
- CHAINS Conference 2015, Veldhoven, the Netherlands, **poster** (30 November-2 December 2015).

List of Publications

1. Quantum and electrochemical interplays in hydrogenated graphene.

Lin Jiang, Wangyang Fu, Yuvraj Y. Birdja, Marc T. M. Koper, Grégory F. Schneider, *Nature Communications*, 2018, 9(1), 793.

2. Contact angle measurement of free-standing square-millimeter single-layer graphene.

Anna V. Prydatko, Liubov A. Belyaeva, **Lin Jiang**, Lia M. C. Lima, Grégory F. Schneider, *Nature Communications*, 2018, 9 (1), 4185.

3. Liquids relax and unify strain in graphene.

Liubov A. Belyaeva, **Lin Jiang**, Jelger H. Risselada, Jeroen Methorst, Grégory F. Schneider, *Nature Communications*, in press (2020).

4. Effects of substrate and polymer encapsulation on CO₂ electroreduction by immobilized indium (III) protoporphyrin.

Yuvraj Y. Birdja, Rafael E. Vos, Tim A. Wezendonk, **Lin Jiang**, Freek Kapteijn, Marc T. M. Koper, *ACS Catalysis*, 2018, 8(5), 4420-4428.

5. Redox interconversion between Co^{III} thiolate and Co^{II} disulfide compounds.

Feng Jiang, Maxime A. Siegler, Xiaobo Sun, **Lin Jiang**, Celia Fonseca Guerra, Elisabeth Bouwman, *Inorganic Chemistry*, 2018, 57(15), 8796-8805.

6. Sensing at the surface of graphene field-effect transistors.

Wangyang Fu, **Lin Jiang**, Erik P. van Geest, Lia M. C. Lima, and Grégory F. Schneider, *Advanced Materials*, 2017, 29(6), 1603610.

7. Rupture index: A quantitative measure of sub-micrometer cracks in graphene.

Hadi Arjmandi-Tash, **Lin Jiang**, Grégory F. Schneider. *Carbon*, 2017, 118, 556-560.

8. Graphene-stabilized lipid monolayer heterostructures: a novel biomembrane superstructure.

Lia M. C. Lima, Wangyang Fu, **Lin Jiang**, Alexander Kros, Grégory F. Schneider, *Nanoscale*, 2016, 8(44), 18646-18653.

9. Determination of isoniazid content via cysteic acid/graphene modified glassy carbon electrode.

Xiaojing Si, **Lin Jiang**, Xinyue Wang, Yaping Ding, Liqiang Luo, *Analytical Methods*, 2015, 7(2), 793-798.

10. Electrodeposited nitrogen-doped graphene/carbon nanotubes nanocomposite as enhancer for simultaneous and sensitive voltammetric determination of caffeine and vanillin.

Lin Jiang, Yaping Ding, Feng Jiang, Li Li, Fan Mo, *Analytica Chimica Acta*, 2014, 833, 22–28.

11. Facile and novel electrochemical preparation of a graphene-transition metal oxide nanocomposite for ultrasensitive electrochemical sensing of acetaminophen and phenacetin.

Lin Jiang, Shuqing Gu, Yaping Ding, Feng Jiang, Zhen Zhang, *Nanoscale*, 2014, 6(1), 207–214.

12. Mild and novel electrochemical preparation of β -cyclodextrin/graphene nanocomposite film for super-sensitive sensing of quercetin.

Zhen Zhang, Shuqing Gu, Yaping Ding, Mingju Shen, **Lin Jiang**, *Biosensors and Bioelectronics*, 2014, 57, 239–244.

13. A novel nonenzymatic fructose sensor based on electrospun LaMnO_3 fibers.

Duo Xu, Liqiang Luo, Yaping Ding, **Lin Jiang**, Yuting Zhang, Xiaoqian Ouyang, Bingdi Liu, *Journal of Electroanalytical Chemistry*, 2014, 727, 21–26.

14. Amperometric sensor based on tricobalt tetroxide nanoparticles–graphene nanocomposite film modified glassy carbon electrode for determination of tyrosine.

Lin Jiang, Shuqing Gu, Yaping Ding, Daixin Ye, Zhen Zhang, Fenfen Zhang, *Colloids and Surfaces B: Biointerfaces*, 2013, 107, 146–151.

15. Oxygen reduction reaction on nitrogen-doped graphene activated by co-doped oxygen functional groups.

Lin Jiang, Bas van Dijk, Longfei Wu, Jan P. Hofmann, Viorica Tudor, Marc T. M. Koper, Dennis G. H. Hetterscheid, Grégory F. Schneider, submitted.

16. Hydrogenation cleans up airborne contamination from graphene.

Lin Jiang, Pauline M.G. van Deursen, Hadi Arjmandi-Tash, Liubov A. Belyaeva, Haoyuan Qi, Jiao He, Vincent Kofman, Longfei Wu, Valerii Muravev, Ute Kaiser, Harold Linnartz, Emiel J.M. Hensen, Jan P. Hofmann, Grégory F. Schneider, submitted.

17. Biaxial compression of centimetre-scale graphene.

Hadi Arjmandi-Tash, Hessam Sokooti, Khosrow Shakouri, **Lin Jiang**, Alexander Kloosterman, Marius Staring, Lia M.C. Lima, Grégory F. Schneider, submitted.

18. Hydrogenated and nitrogenated graphene for field effect gas sensing.

Lin Jiang, Wangyang Fu, Elisabeth Bouwman, Grégory F. Schneider, in preparation.

Acknowledgements

I would like to thank all my collaborators who contributed to this thesis. Dr. Yuvraj Y. Birdja, Prof. dr. Marc T. M. Koper, thank you for your experimental support and the fruitful collaboration in studying the fundamental electrochemical activity of graphene. I also want to acknowledge Bas van Dijk, Dr. Dennis G. H. Hetterscheid and Prof. dr. Marc T. M. Koper for all the discussions about the electrocatalytic properties of a monolayer graphene. To Dr. Jiao He, Vincent Kofman, Prof. dr. Harold Linnartz, Dr. Haoyuan Qi, Prof. dr. Ute Kaiser, Dr. Longfei Wu, Dr. Jan P. Hofmann, Valerii Muravev, Prof. dr. Emijel J. M. Hensen for the experimental support and discussions.

Another special thank you goes to Prof. Yaping Ding, Prof. Liqiang Luo and Prof. Weiguo Cao from Shanghai University, who give a lot of help and advice for my research career. Especially, I would like to thank Prof. Ding for her support and guidance for my master study, which inspired me to go after further PhD study.

My sincere thanks also go to my colleagues and officemates. Yanina, Hadi, Amedeo, Lia, Liuba and Wangyang, thank you all for the nice, friendly and wonderful atmosphere in the lab in the starting stage of the group. Yanina, thank you for your warm, patient and kind introduction and help in the first year of my PhD. Hadi and Wangyang, thank you for the participation and guidance in my PhD projects. To Amedeo and Lia, thank you for being always so cheerful and caring for everything. I would like to thank Liuba for being a bright, brave and intelligent office mate, who inspired me a lot in life and in science. To Pauline, Erik, Alex, Xue, Xiaoyan, Weizhe, Max, Batuhan and Valeria, thank you for keeping the spirit. To Pauline and Alex, thank you for the help in translating the thesis summary. Many thanks to the other SBC-ers, Lily, Nicola, Jing, Yue, Tingxian, Ciqing, Ye, Mengjie, Ying, Wei, Aimee, Fred, Victoria, Willem, Jan, Rene, Nestor, Francesca, Panagiota, Gabriela, Bartjan, Niek, Elena, Jeroen, Geert, Dimitris, Teun, Elena, Roy, Jolinde, Roxanne, Michelle, Wim and Viorica, and all others.

I want to thank my friends. Nicole and Tom, thank you for making my life in Leiden more Dutch and more fun. Also, I want to thank Yun, Yasmine, Gang, Qing, Qiang, Xuequan, Ye, Chengyu, Yurong, Donggang, Maolin, Wanbin, Yi and Xu for the wonderful LSC community activities we made together. Thank you, Marlon and your fellows, for all the help during my stay in the Netherlands. I would also like to thank Siyuan, Yangan, Hui, Xin, Xiaoting, Jing, Kun, Yifan, Zhichao, Jichao, Gangqi, Zhiwei, Meng, Wenjing, Xiansha, Shengxiang, Chunmiao, Chen, Qingju, Silvia, Koen, Michiel, Martijn for sharing your knowledge, experience and positive energy you gave me.

Many thanks to all my nice neighbors – Zhuang, Jiaxin, Xiaobing, Jing, Peng, Jian, Zhen, Junfei, Yiran, Jialong – for all the fun and sweet neighborhood memories.

Finally, I want to thank my parents for their unconditionally love and support throughout my life. Thank you, my parents-in-law, for the understanding, respect and backing. Thank you, Nana, for your accompany and for being my sister. Last but not the least, I want to express my gratitude and love to my soulmate, Feng, who knows me better than anyone else, who inspires me to be a better person, who accepts and believe in me even when no one else would. And thank you my dear lovely son, Mingze, for making me the happiest mother in the world.

